

# On the vegetation front dynamics generated by strong versus weak nonlocal interactions

---

A thesis submitted in partial fulfilment of the requirements  
for the degree of Doctor in Science

**Cristian Fernandez Oto**

---

Academic year 2016-2017

Supervisor: Prof. Mustapha Tlidi

## **Résumé: Auto-organisation de la végétation dans des écosystèmes arides**

Dans cette thèse, nous étudions différentes structures de végétation issues de l'auto-organisation spatiale. Ce phénomène est visible dans des zones (semi-)arides où le potentiel d'évapotranspiration dépasse sensiblement la moyenne des précipitations annuelles. Ce déficit hydrique freine le développement des plantes individuelles et, au niveau communautaire, stimule des comportements de agrégation même si la topographie est isotrope. Dans ce contexte, nous adoptons une approche basée sur l'équation F-KPP non-locale permettant de formuler ces hypothèses en termes de propriétés des plantes individuelles.

Une partie importante de cette thèse concerne l'étude d'un exemple de structure de végétation localisée bien connu dans la littérature, les cercles de fées. Les cercles de fées ont été découverts dans le désert de Namibie. Cependant, ces dernières années, ils ont aussi été observés en Australie. Plusieurs hypothèses ont été proposées dans la littérature. Nous proposons la compétition non-locale forte entre plantes individuelles (en utilisant un noyau de type Lorentzien) comme ingrédient principal pour expliquer la formation des cercles de fées. Le couplage non-local fort influence l'interaction entre fronts dans le régime bistable (loin de toute forme d'instabilité briseuse de symétrie). Dans le cas d'un couplage non-local faible, par exemple dans un noyau Gaussien, l'interaction entre fronts est toujours attractive. Par conséquent, les structures localisées qui résultent de l'interaction des fronts sont instables. Le couplage non-local fort peut induire la stabilisation de structures localisées que nous interprétons comme étant des cercles de fées. Notre mécanisme permet d'expliquer les principales caractéristiques des cercles de fées, comme la relation entre leur diamètre et la disponibilité des ressources. De plus, nous avons appliqué ces résultats à d'autres modèles de végétation. Nos résultats concordent avec les observations sur le terrain.

Nous avons analysé la formation de "spots" de végétation dans la région Andine en Bolivie. Nous avons étudié comment un modèle standard d'interaction-

redistribution génère des “spots”, de longueur d’onde d’approximativement 1.36m, via une instabilité qui brise la symétrie. En considérant des paramètres réalistes, nos résultats concordent avec les observations sur le terrain.

Enfin, nous avons étudié la formation de structure en forme de spirale dans un système qui couple la végétation et les herbivores dans un modèle proie-prédateur. Nous avons trouvé que le mécanisme qui induit la formation de spirales est l’excitabilité. Nos observations sur le terrain et nos résultats numériques du modèle montrent que les spirales de végétation ont une profondeur de quelques centimètres et une longueur de quelques mètres. En ce qui concerne l’échelle de temps, nos estimations donnent une période de rotation de l’ordre de 10 ans.

# Acknowledgments

First I want to acknowledge my supervisor Mustapha Tlidi. He has been very helpful during more than four years. I want to thank him for all the scientific conversations, help to solve several problems, wonderful advice on countless occasion, and support to finish my PhD.

I want to acknowledge the Jury of this thesis for their careful reading and constructive criticism (P. Gaspard, P. Kockaert, R. Lefever, K. Panajotov, A. Vladimirov, and my supervisor M. Tlidi). I am also thankful to all my collaborators in different works during my PhD (M. Clerc, D. Escaff, G. J. de Valcárcel, K. Panajotov, K. Staliunas, P. Couteron , F. Anthelme, A. Reina, G. Valentini, M. Dorigo, V. Trianni, P. Kockaert, J. Cisternas, S. Weisser, and of course M. Tlidi). In addition, I want to thank S. Coulibaly, R. Rojas, R. Troncoso, A. Cisternas, C. Erices, E. Meron, Y. Zelnik, H. Yizhaq, and O. Tzuk for all the fruitful discussions over these years.

Family and friends are very important in my life and I want to thank all of them. I want to acknowledge my mother (Angelica Oto), my father (Manuel Fernandez) and my sister (Soledad Fernandez). I especially acknowledge the friends that proof-read my thesis (Robson, Shyam, Mauro, Eleonora and Sofi). It is impossible to mention all the friends who shared time with me during this period in Brussels, however I want to say thank you to everyone (Cati, Nacho, Rakib, Gus and Ann, Edu, several Andreas, several Lorenzos, Nirmal, Arash, Lapo, Pato, Hernan, Simona, Davide, Isabelle, Tefa,

Marcela, Guiliano, Celine, Laura, Gaston, Marco and Giovanna, Stephane, Etienne, Pedro, Nico, Issar, Gabin, Isabel, Marcelo, Rossella, Rosanna, Anna catalana, Mauro italiano, Agnese, Erica, Vero, Dani, Sara, Helene, Camilla, Davide, Barab and Giulia, Jeremie, Alessandra, Fede, Felito, Anna, Helena, Sonsoles, Rafa, Antonio, Artiza, Lidia, Christoph, Lucia, Diego, Evaristo, Charo, Angela, Ana gallega, Rebe, Franz, Nico, Nora, Cristina, Elise, Anne-Sophie, Kevin, Alice, Vladi, Michela, Katja, Hanni, Nacho, Yolanda, Miguel, Ainhoa, Sarita, Leire, Kristin, Monica, Mela, Felipe, Ana Maria y Alex, Maria Isabel, Juliana, Jorge y Jessica, Sebas, Juanita, Camila, Joao, Adolfo, Claudito and Sabina, Ire, Carlos, Ralf and Helena, Rodrigo, Pablo, Leslie, DJ, Rachel, Leah, Alejandro and Andrea, Peter, Sino, Stela, Tania, Cata, Franceline, Raliaga, Sandro, Amanda, Kasia, Conti, Angelica, Greta, Bianca, Henry, the “portugueses”, Liberty, Eric, Laurent, Anat, Ele, Abraham, Anne, Marija, Maria, Max and Lusine). Sorry if I forgot to mention someone.

Finally, I want to acknowledge the financial support of “Becas Chile” and Fondecyt of the government of Chile, the “Fonds Van Buuren”, and “bourses de voyages de la Fédération Wallonie-Bruxelles”.

# Contents

|          |                                                                 |           |
|----------|-----------------------------------------------------------------|-----------|
| <b>1</b> | <b>Introduction</b>                                             | <b>9</b>  |
| 1.1      | Vegetation patterns . . . . .                                   | 9         |
| 1.2      | Fairy circles . . . . .                                         | 15        |
| 1.2.1    | Description . . . . .                                           | 15        |
| 1.2.2    | Hypotheses of their formation and maintenance . . . . .         | 17        |
| <b>2</b> | <b>Effects of strong nonlocal coupling in a bistable model</b>  | <b>24</b> |
| 2.1      | Strong versus weak nonlocal coupling . . . . .                  | 26        |
| 2.2      | A simple bistable model with strong nonlocal coupling . . . . . | 27        |
| 2.3      | Symmetry breaking instability . . . . .                         | 29        |
| 2.4      | Single fronts . . . . .                                         | 31        |
| 2.5      | Fairy circles . . . . .                                         | 37        |
| 2.6      | Flat spots . . . . .                                            | 41        |

|          |                                                                                                          |           |
|----------|----------------------------------------------------------------------------------------------------------|-----------|
| 2.7      | Conditions for the appearance of fairy circles and flat spots                                            | 45        |
| 2.8      | Interaction of fairy circles . . . . .                                                                   | 46        |
| <b>3</b> | <b>Fairy circles in vegetation models for arid regions</b>                                               | <b>56</b> |
| 3.1      | The strong nonlocal logistic-type model . . . . .                                                        | 57        |
| 3.2      | Fairy circles in the nonlocal logistic-type model . . . . .                                              | 60        |
| 3.3      | Analytical description in the nonlocal logistic-type model . . . . .                                     | 64        |
| 3.4      | Numerical simulations of fairy circles in the strong nonlocal reaction-diffusion type of model . . . . . | 66        |
| <b>4</b> | <b>Spots in a semiarid region in the highlands</b>                                                       | <b>70</b> |
| 4.1      | The logistic-type model . . . . .                                                                        | 72        |
| 4.2      | Spatial instability of the homogeneous state . . . . .                                                   | 74        |
| 4.3      | Measurement of the parameters . . . . .                                                                  | 76        |
| 4.4      | Localized spots of vegetation . . . . .                                                                  | 83        |
| <b>5</b> | <b>Spiral vegetation patterns</b>                                                                        | <b>87</b> |
| 5.1      | Field observations . . . . .                                                                             | 88        |
| 5.2      | Mechanism for excitability . . . . .                                                                     | 92        |
| 5.3      | Mathematical model . . . . .                                                                             | 93        |
| 5.4      | Excitability of the system . . . . .                                                                     | 95        |
| 5.5      | Numerical simulations . . . . .                                                                          | 98        |

|          |                                   |            |
|----------|-----------------------------------|------------|
| <b>6</b> | <b>Conclusions and discussion</b> | <b>101</b> |
|          | <b>Bibliography</b>               | <b>104</b> |
| <b>7</b> | <b>Appendix</b>                   | <b>123</b> |

# Chapter 1

## Introduction

### 1.1 Vegetation patterns

The first observation of vegetation patterns, on a scale of 100 meters, was published by Macfadyen in 1950 [1,2]. This observation was made in Somalia and consists of “arcs of vegetation” (also called tiger-bush) separated by more than 100 meters. The arcs of vegetation are composed by trees, bushes and grasses, which create a vegetation width of around 30 meters. The average wavelength of this spatial structure is around 158 meters. Given the long distance between two arcs of vegetation, the observation from the ground of this spatial pattern is almost impossible, and aerial photographs were needed to discover this periodic structure. Note that the vegetation patterns [3] are not limited to Somalia. They can also be observed in several continents [4–6]. The soil where these patterns emerge, and their composition (grasses, bushes, or trees), is not a relevant factor [1,4,5,7–9]. Hence, the interpretation of these observations should be general. Indeed Macfadyen said [1] “The study of the first two patterns, of which I have been able to find no previous recognition, is not conveniently to be pigeon-holed

under any one accepted branch of knowledge, and the phenomena are thus awkward to classify. They are manifestly within the province of botany and ecology; the essential background concerns geomorphology and meteorology; the causes, as I believe, must be investigated by physics and mathematics; and the whole matter must be studied on air photographs, since on the ground it proved difficult to recognize the patterns at all.”

The formation of spatial periodic vegetated patterns is related to the scarcity of resources such as nutrients or water. The absence of sufficient rainfall is the key factor in explaining several patterns of vegetation. The poverty of this basic resource in different regions is one of the most important issues of our times. The continuous droughts and the climate change are increasing the arid and semiarid regions around the world. Note that a region is considered arid or semiarid when evapotranspiration is high compared to precipitations. Such regions cover around 31% of land area of the world. Hence, arid or semiarid regions, and their ecosystems, are relevant to several countries and people. As a consequence, the patterns of vegetation that emerge on these regions increase in their relevance everyday. A summary from 2010 of the spatial patterns of vegetation, with a wavelength over 60 meters, is shown in Figure 1.1 [10]. Moreover, spatial patterns of vegetation with wavelength above 60 meters are spread around several countries with arid or semiarid environments.

Several decades after the first observations of tiger-bush by Macfadyen [1], self-organization arises as the most accepted explanation for the mentioned spatial patterns and several others. In 1997, Lefever and Lejeune proposed for the first time a mathematical model that gives a realistic explanation of this intriguing phenomenon [11]. Their model describes at the level of individual plants the birth/death process, and the nonlocal interactions (competition or facilitation) which exist within plant communities. This work is able to explain the formation of vegetation patterns even on flatland, as a consequence of a symmetry breaking instability.

The formation of stripes of grasses or trees which go up on a hill was explained by a reaction-diffusion type of model in 1999 [12]. This model

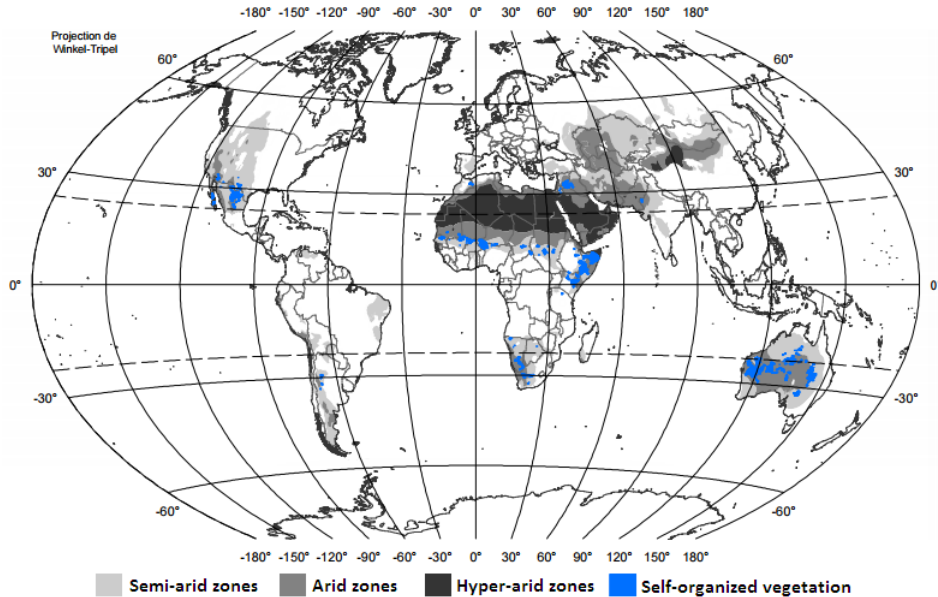
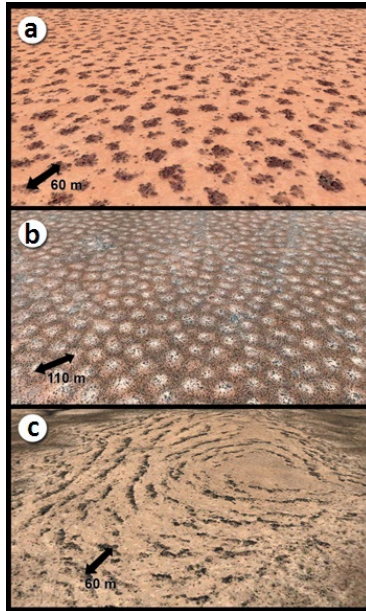


Figure 1.1: Geographic distribution of the hyper-arid, arid and semiarid regions (source [10]). The blue areas represent regions that exhibit vegetation patterns with wavelength over 60 meters.

considers two dynamical variables: the biomass density per unit area, and the water which moves downhill. The stripes of trees reported in that work move uphill around 0.5 meters per year, and their wavelength is around 45 meters. The stripes of grass move uphill around 1.7 meters per year, and their wavelength is around 18 meters. Later on, several works have confirmed the previous predictions and have included periodic patterns of spots and gaps [13–21]. Figure 1.2 shows spots, gaps and tiger-bush in a), b) and c) respectively.

The patterns showed in Figure 1.2 have a wavelength that increases with the aridity, i.e. the distance among areas of vegetation (separated by bare soil) increases with the reduction of water (rainfall) [23, 24]. A general



*Figure 1.2: Vegetation patterns (source [22]). Figure a, b, and c shows spots, gaps and tiger-bush respectively. Their formation is associated with a low level of rainfall in arid regions.*

behavior, over the difference in wavelength according to the availability of water, is the order in which the different patterns emerge [23]. Indeed, the vegetation is homogeneous with sufficient water resources. By decreasing the rainfall, the typical patterns that first emerge are gaps devoid of any vegetation. Considering a lower level of rainfall, we can observe stripes. Taking into account an even lower level of water, that sometimes allows the bare state to become stable, we can find spots of vegetation in a matrix without vegetation. This sequence of patterns is observed in several regions and it has been shown by several authors theoretically and numerically [13, 15, 23–28] as a natural consequence of self-organization that imposes the system to have less and less area covered by vegetation when the water

resources decrease.

More than 60 years later, we can conclude that the statement of Macfadyen “the causes (of vegetation patterns), as I believe, must be investigated by physics and mathematics” [1] was correct. Nonetheless, the way to model the vegetation in arid regions does not have a consensus. In the literature, there are three well-established types of modeling that describe vegetation patterns. They are the nonlocal F-KPP (Fisher-Kolmogorov, Petrovsky and Piskunov [29,30]) equation which is also called the logistic-type of model [31] or the generic interaction-redistribution model [11,27,32,33], the reaction-diffusion kind of model [12,15,34–50], and the stochastic approach [51–53]. Lefever and Turner classify them as [24]:

“(i) The non-local F–KPP approach: it focuses on the relationship between the structure of individual plants and the facilitation–competition interactions existing within plant communities. The biomass density is defined at the individual plant level; the modeling calls for no other state variable [11,27].”

“(ii) The reaction–diffusion approach: it emphasizes the influence on vegetation patches of water transport by below ground diffusion and/or above ground run-off. The biomass density is defined at the patch level. Together with the water concentration below ground and/or in some surface ground layer, it constitutes the set of state variables [12,15,19,49,54,55].”

“(iii) The stochastic approach: it focuses on the “constructive” role of environmental randomness as a source of noise induced symmetry breaking transitions triggering pattern formation. These transitions occur when the variance of environmental noise increases while its average value remains constant [52,57].”

Besides periodic vegetation patterns, there are aperiodic and localized structures. For instance, another kind of structure that appears in some arid regions is localized spot of vegetation. The formation of these structures is related to the symmetry breaking instability [38,56,58,59] (this is also the



*Figure 1.3: Localized spots. Ground pictures from French Guiana (source [56]). One single spot is illustrated in a). Figure b) shows two spots.*

mechanism to explain the aforementioned periodic patterns). The localized spots come from the bistability between the bare state and the periodic spots patterns, in a region of parameters where the spots and the bare state do not invade the other. Figure 1.3 illustrates spots of vegetation in a savanna region [56]. Rings of vegetation, as the ones illustrated in Figure 1.4, are other well-known structures that are not periodic patterns. These rings are formed spots that grew in their diameter [60–62]. When the diameter of a spot grows enough, suddenly the spot start to generates a hole in its center. This hole and the ring itself grow, leaving behind a small tail of dead grass as illustrated in Figure 1.4. Note that there are different types of rings around the world and not all of them come from the same mechanism: here we have presented the rings of vegetation observed in arid regions.



*Figure 1.4: Fairy Rings. Both photos show fairy ring in the north of Chile, near San Pedro de Atacama.*

## 1.2 Fairy circles

### 1.2.1 Description

Fairy circles are other fascinating and well-documented examples of structures of vegetation. They are bare circles surrounded by a matrix of vegetation (See Figure 1.5). In general, fairy circles exhibit a high level of biomass on the frontier between the bare soil of the circle and the vegetation of the matrix, which is called the fringe of the fairy circle. This mysterious phenomenon has been studied for several decades [63–70] and its origin is still a subject of debate. They have been observed in Namibia, Angola and South Africa [65]. Recently, fairy circles have also been observed in Australia [71] as shown in Figure 1.5b.

Fairy circles are found in arid or semiarid regions in Namibia, where the precipitations are in the range of 50-150mm/yr. It has been reported that these structures have a diameter that ranges from around 2 meters to more than 20 [65,67,68]. These diameters are much larger than the size of the grasses forming the matrix. Regarding the time scale of fairy circles, several authors suggest that the fairy circles found in Namibia have an average life between 50yrs [72] and more than 100yrs [65,68]. Direct observation of the

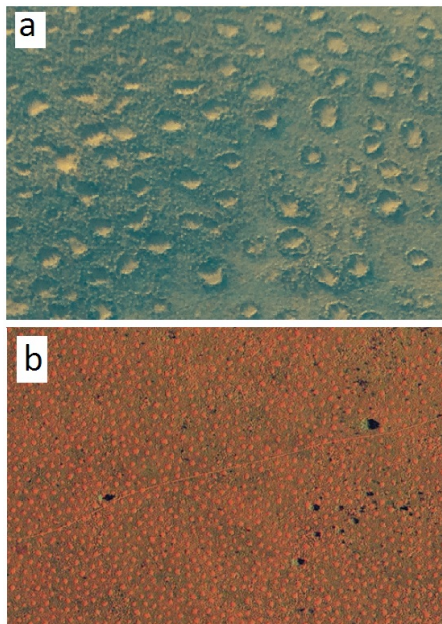


*Figure 1.5: Figure a: Several fairy circles in the NamibRand Nature Reserve. The photo was taken on February 27th, 2015. Figure b (source [71]): Fairy circles in Australia.*

formation of fairy circles or their deaths have not been documented. On the other hand, satellite observations have shown that the time of birth and death of these structures span a few years [72], even two orders of magnitude less than their typical life time.

Another important feature of fairy circles is their robustness with respect to the kind of soil where they exist. In fact, it is possible to observe these localized structures on different kinds of soil, such as sandy (Figure 1.6) or rocky soil (Figure 1.7). It has also been proved that the sandy soil in Namibia and the soil in Australia, where we can observe fairy circles, have different features. Indeed, in contrast with the soil where fairy circles



*Figure 1.6: Fairy circle in NamibRand Nature Reserve in sandy soil. The photo was taken on February 26th, 2015.*

are present in Namibia, the soil of fairy circles in Australia has a relevant infiltration contrast [71].

### **1.2.2 Hypotheses of their formation and maintenance**

Probably due to their long time dynamics, and also the space necessary for their formation, fairy circles are not easy to find or reproduce in the laboratory. These difficulties have allowed the existence of several hypotheses to explain fairy circles. These can be classified into two types: the hypotheses that suggest self-organization theory as the main ingredient to explain fairy circles [65–67, 69–71, 73–77]; and the hypotheses that take into account other external elements such as termites [64, 68, 78–83], ants [80, 84], allelopathic chemicals [63, 85], microbial communities [86], or abiotic gas [87, 88] to explain this phenomenon.



*Figure 1.7: Fairy circles near NamibRand Nature Reserve in rocky soil. The photos were taken on March 2nd, 2015. The first photo shows fairy circles with huge rocks inside them. The second photo shows a fairy circle in a completely rocky soil.*

The most important hypotheses that consider external factors are:

- **Allelopathy:** The first documented hypothesis considers *Euphorbia* species of plants as the relevant ingredient to explain the formation of fairy circles [63]. The remains of these plants were assumed to generate some biochemicals which interfere negatively in the germination and growth of other plants. Given a correlation, in some areas, between the number and the size of these plants, and the number and the size of fairy circles, Theron concluded that fairy circles are consequence of some allelopathic chemical from the remains of *Euphorbia* species of plants [63]. Later studies have not found allelopathic chemicals in fairy circles [65, 67, 78]. Indeed, this hypothesis was neglected since the seventies until a publication in 2015 [85] that found some correlation between fairy circles and a *Euphorbia* species in a specific area. However, there is still no evidence of any allelopathic biochemical in the circles area. In any case, the effect of an allelopathic biochemical should disappear after some years and the long life of fairy circles [65, 75] is not in agreement with this possibility.
- **Radiation:** This hypothesis is based on the effect of radiation on vegetation. Indeed, it has been proved that vegetation dies or cannot grow in areas with certain levels of radiation [89]. Nonetheless, there are no positive measurements of radiation in any fairy circle to confirm this hypothesis. Soil sample analysis have shown that this hypothesis cannot be supported [65].
- **Hydrocarbons:** This hypothesis suggests gas as the key factor to explain fairy circles, and is based on some measurements developed in [87, 88]. These results suggest a small difference in the quantity of hydrocarbons between the soil inside the circle and the soil in the matrix of vegetation. Nonetheless, this hypothesis has been refuted by some authors [74, 75]. Note that a small difference of some gases could generate the necessary condition to avoid the growth of plants. However, a small difference in the characteristics of the soil (such as

different levels of hydrocarbons) could also be the natural process for the decades of differences on the vegetation area versus the bare area.

- Microbial communities: Another theory, supported by a recent paper [86] and mentioned by some people living near the NamibRand reserve, proposes microbial communities as a relevant factor to the formation and/or maintenance of fairy circles. The mentioned paper is based on a significant difference of microorganisms in the bare soil versus the matrix in five fairy circles. However, as in the hypothesis related to hydrocarbons, it is not clear whether the presence of bacteria and fungi generates the fairy circles or the fairy circles increase the presence of these microorganisms.
- Termites: The most popular hypothesis that considers an external agent to generate fairy circles is the one referred to termites. This hypothesis has been proposed by different authors at least since 1994 [64] until recent years [68, 78–80, 82]. This option suggests that a nest of termites is in the center of the circle, and the termites feed themselves with the grasses on the border of the circle. Some authors even propose that termites design these circles in order to have a reservoir of water [68]. However, several works have found inconsistencies in this hypothesis and their authors reject termites as the main element in the formation and the conservation of fairy circles. They have considered different weaknesses of this hypothesis such as termites do not eat in circles as perfect as fairy circles, termite nests are in several positions and not only in the bare circles, the specific kind of termites found in Namibia are not present in Australia, or that large regions of fairy circles in Namibia exhibit a coherence among them that the nests of termites do not present [65, 70, 71, 74]. Another relevant issue is that areas as the ones presented in Fig 1.7 are rocky soil, and this kind of soil is not a good environment for termites. Note that, not all the authors who support this hypothesis suggest the same species of termite as the cause of fairy circles. Indeed, over the different species of termites proposed in Namibia, a new type of termite is proposed to

explain the circles in Australia [90].

- Ants: Some authors consider harvester ants as one of the primary causes of fairy circles [80, 84]. This hypothesis has been mentioned vaguely, generally in relation with termites. However, there are several works that evaluate this factor and conclude that there are no evidence to support that ants are a factor which determines the formation or maintenance of fairy circles [70, 74].

In 2004, van Rooyen et. al. [65] investigated the most relevant hypotheses suggested at that time, including several of the hypotheses mentioned above. They concluded that none of them can explain the origin of fairy circles. In addition, they suggested self-organization as a possible mechanism for their formation. After that, several works have proposed self-organization to explain fairy circles. Experimental works conclude, without any mathematical model, that the mechanism to generate fairy circles is related to low levels of water and/or nutrients in the soil [67, 75, 77]. Several works based on mathematical modeling have also proposed self-organization to explain the formation of fairy circles [66, 69, 71, 74]. There are two articles that reject the self-organization hypothesis [81, 82]. Nevertheless, the authors of these works misunderstand the conditions of self-organization and its effects in the availability of water in the circles.

We identify two types of mathematical modeling which try to explain the formation and permanence of fairy circles. The first kind of mathematical modeling is associated with spatial instabilities that generate patterns and localized structures in space, which the authors interpreted as fairy circles [66, 70, 71, 74]. Figure 1.8 illustrates the numerical results of fairy circles from some of these works. We consider that this explanation, related to a spatial instability, omits relevant features of fairy circles such as the flat area devoid of any vegetation, and the presence of only one fringe of high biomass density on the border.

We have proposed a second kind of mathematical modeling, in a region of parameters far from any spatial instability, as a possible explanation of

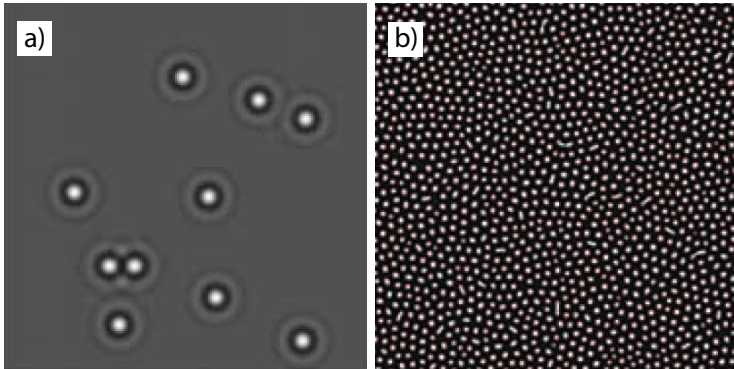


*Figure 1.8: Spatial instability and pattern formation as explanation of fairy circles. Figure a) shows numerical simulations of few gaps (source [66]). Figure b) shows numerical simulations of several gaps (source [74]) .*

fairy circles [69, 73, 91]. Our mechanism is based on the strong nonlocal competition among individual plants (mediated by a Lorentzian type of Kernel) as the main ingredient to explain the formation of fairy circles. The strong nonlocal coupling affects the interaction among fronts (in the bistable regime) and is able to modify this interaction from attractive to repulsive. This strong nonlocal interaction might induce the stabilization of localized structures that we interpret as fairy circles. Our mechanism can explain the main features of fairy circles such as the relation between their size and the availability of resources, the circular area devoid of any vegetation, and the single fringe on the borders of fairy circles.

This thesis is organized as follows. Following this brief introduction, in Chapter 2 we study the strong nonlocal coupling in a bistable model of population dynamics. We find that this kind of coupling varies the asymptotic behavior of fronts. In addition, the analysis to evaluate the symmetry breaking instability changes. We prove that fairy circles and flat spots become stable in a precise range of parameters by the effect of strong nonlocal competition in the bistable regime. Finally in this chapter, we study the interaction among fairy circles. We show that the interaction between

fairy circles is repulsive and modifies the size of the structures. In Chapter 3, we apply the results obtained in Chapter 2 to other models of vegetation. We modify these models to include a strong nonlocal coupling. Our results, by considering a standard interaction-redistribution model, are in agreement with field observations and they replicate the main features of fairy circles in Namibia. Moreover, we show that a reaction-diffusion type of model, incorporating strong nonlocal coupling, also exhibits this mechanism in a range of parameters. In Chapter 4, we analyze the formation of spots of vegetation in the Andean highlands in Bolivia. We study how a generic interaction-redistribution model, through a symmetry breaking type of instability, generates spots. The numerical and theoretical wavelength of these spots, considering realistic parameters, agrees to field observations. In Chapter 5, we study the formation of spirals of vegetation in a system that couples vegetation and wild herbivores as a predator-prey model. We find a mechanism that induces the formation of spirals. Through field observations, we obtain that the spirals of vegetation have a width of few centimeters and a length of few meters. On the time scale, our estimation gives a period of rotation of the order of 10 years. In Chapter 6, we conclude and discuss our results.

## Chapter 2

# Effects of strong nonlocal coupling in a bistable model

The emergence of localized structures, also called dissipative solitons, has attracted considerable attention in many areas of natural science, such as chemistry, physics, plant ecology, and optics [92–97]. These stable solutions arise in a dissipative environment and belong to the class of dissipative structures found far from equilibrium [98]. In most cases, the spatial coupling is local for which transport processes like diffraction, dispersion, or diffusion are described by the Laplace operator. The coupling between this process and nonlinearity in dissipative environment, leads to a self-organization phenomenon that is responsible for the formation of either extended or localized patterns. This behavior also occurs in many natural dissipative systems with nonlocal coupling such as firing of cells [93, 99], propagation of infectious diseases [100], population dynamics [101, 102], nonlinear optic [94, 103], fluids [104], granular [105], neural science [106], and vegetation patterns [11, 27]. This issue has been abundantly discussed and is by now well understood. So far, however, far from any pattern forming instability, fronts dynamics leading to formation of localized structures in these systems

has received scant attention [101, 102, 107–109]. These nonlinear waves can be seen as a solution that connects two stable steady states. They are characterized by a continuous parameters, the front position, which accounts for the position of the largest spatial variation of the front.

Nonlocal functions, also known as influence or kernel functions, can be classified into two types, depending on whether this function decays asymptotically faster or slower than an exponential function, which corresponds to a weak or strong influence function, respectively [110]. Front interaction is usually characterized by the behavior of the tail of one front around the position of the other front. This situation corresponds to the case of weak influence functions. However, for strong influence functions, the interaction is controlled by the whole influence function and not only by the asymptotic behavior of the front tails. More importantly, the nature of the interaction between fronts is affected by the choice of the influence function. When considering a weak nonlocal coupling, the asymptotic behavior of front solutions is described by either exponential decay or damping oscillation. In the former, front interaction is attractive and decays exponentially with the distance between the fronts. Therefore, bound states resulting from fronts interaction are unstable. However, in the latter, fronts interaction alternates between attractive and repulsive with an intensity that decays exponentially with the distance between fronts [101, 102, 107–109]. For a fixed value of parameters, a family of stable one dimensional localized structures with different sizes has been reported by these authors.

In this chapter, we show that front dynamics mediated by strong nonlocal coupling like Lorentzian type of kernel in bistable media leads to the formation of stable localized structures. Indeed, strong nonlocal interaction could induce a repulsion between fronts, which decreases with the front separation. A balance between this interaction and tendency of an uniform state to invade the other one at constant speed is responsible for stabilizing localized states. Thus, a deformation of this domain returns to its equilibrium size. For large systems, these structures have an intrinsic width, which is determined by the dynamical parameters and not by the boundary

conditions. A single localized structure possesses a fringe and a plateau. We demonstrate also that the kinetic laws governing front interaction obey a power law. This mechanism is robust in one dimension one and two. The generality of our analysis suggests that the strong nonlocal coupling leading to the stabilization of localized structures is a universal phenomenon which does not depend on a specific type of model equation. Our theoretical prediction should therefore be applicable to any spatially extended system with strong nonlocal coupling.

## 2.1 Strong versus weak nonlocal coupling

We aforementioned, in the introduction, that the interaction between plants, including competition and facilitation, is naturally nonlocal. Moreover, the functions that control the interaction between plants can be different and generate, as a consequence, different phenomena. The effect of weak nonlocal kernels, i.e. functions that decay faster than exponential, has been studied by several authors in contexts that goes from optics to populations dynamics [99, 101, 111–113]. On the other hand, experimental measurements have shown that strong nonlocal coupling is present in systems such as optics [114–116] and vegetation [117].

In this chapter, we focus on a strong nonlocal interaction [69, 73, 91, 110], i.e. an interaction mediated by a kernel that decays slower than exponential. Then, we choose the Lorentzian-like function

$$f_{\sigma}(\mathbf{r}) = \frac{N_n}{1 + |\mathbf{r}|^n/\sigma^n}. \quad (2.1)$$

In the kernel function  $f_{\sigma}(\mathbf{r})$ ,

$$N_n = \left( \int \frac{d\mathbf{r}}{1 + |\mathbf{r}|^n/\sigma^n} \right)^{-1}$$

is a normalization constant that could be calculated in one or two dimensions. The parameter  $\sigma$  accounts for the typical range of interaction, and the parameter  $n$  describes the power of decay in the Lorentzian-like function. Figure 2.1 shows the difference between the one dimensional profile of a Gaussian kernel and a Lorentzian kernel. The profile of an exponential kernel is also illustrated to show the limit between strong and weak nonlocal coupling. As can be seen from the figure, the tail of a Lorentzian function decays much slower than the one of a Gaussian function. We show, in this chapter, that the effect of the tail in the nonlocal coupling mediated by a Lorentzian kernel determines the nature of the interaction between fronts which leads to the formation of fairy circles.

## 2.2 A simple bistable model with strong nonlocal coupling

In this chapter our approach is based on the system

$$\partial_t u = f(u) + \nabla^2 u, \quad (2.2)$$

where  $f(u)$  is a function of  $u$ . This equation is the well-known F-KPP equation [29, 30] when  $f(u) = u(1 - u)$ . However, in order to have bistability, we consider  $f(u) = u(u - 1)(\alpha - u)$ . The last case is called by some authors the Nagumo model [101, 118, 119]. To describe the competition between plants discussed above, we incorporate a nonlocal coupling of the form of the Lorentzian. Then, the model is

$$\partial_t u = u(u - 1)(\alpha - u) + \nabla^2 u + \epsilon u \int_{-\infty}^{\infty} K(\mathbf{r}') u^2(\mathbf{r} + \mathbf{r}', t) d\mathbf{r}', \quad (2.3)$$

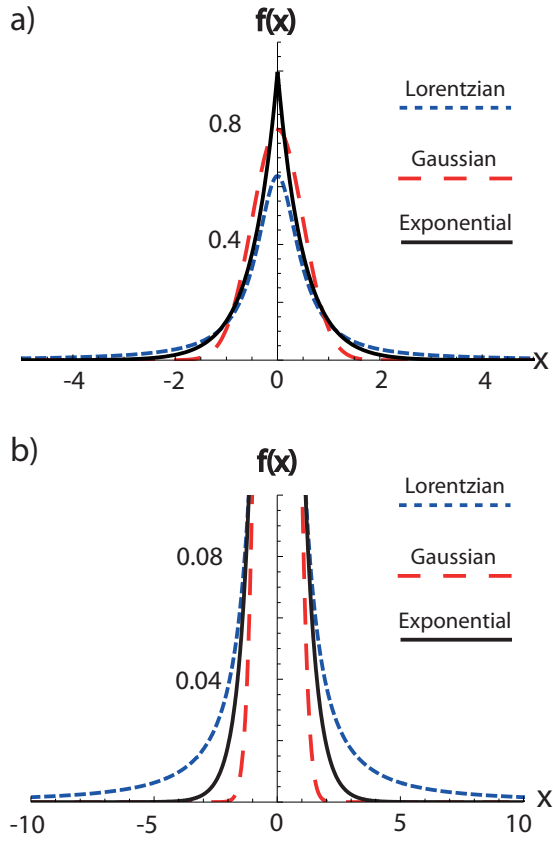


Figure 2.1: Spatial profiles of the Exponential, Gaussian and the Lorentzian kernel. The Lorentzian kernel is given by  $f_{\sigma}(x) = \frac{(\pi\sigma)^{-1}}{1+x^2/\sigma^2}$ . The Gaussian kernel is given by  $\sigma \exp(-x^2/2\sigma^2)/\sqrt{2\pi}$ . The Exponential kernel is given by  $\exp(-x/\sigma)/2\sigma$ . Figure a) shows the typical shape of the kernels, and Figure b) shows a zoom to observe the decaying of the tails. The three kernels have the parameter  $\sigma = 0.5$ .

where  $u$  is a normalized scalar field that represents the population density. The adversity parameter  $\alpha$ , also called the aridity, accounts for the relative advantage between the non-populated state and the full populated state. The normalized diffusion is described by the Laplacian  $\nabla^2$ , and the intensity of the nonlocal coupling is given by  $\epsilon$ . The function  $K(\mathbf{r}) = \delta(\mathbf{r}) - f_\sigma(\mathbf{r})$  considers the kernel function  $f_\sigma(\mathbf{r})$  and the Dirac  $\delta$  function. The Dirac  $\delta$  function is introduced in our model in order that the homogeneous steady states is not affected by the nonlocal coupling.

### 2.3 Symmetry breaking instability

It is easy to prove that Eq. (2.3) has three spatial uniform solutions. The unpopulated state  $u = 0$  is stable. The state  $u = \alpha$  is unstable and represents the minimum value that the population should exceed to survive. Finally, the uniform full-populated state  $u = 1$  may be stable or unstable. The Turing instability [120] of the full-populated state leads to a pattern regime.

We perturb the homogeneous steady state  $u = 1$  for  $n = 2$ , with a finite wavelength perturbation of the form  $\delta_0 \exp(i\mathbf{k}\mathbf{r} + \lambda t)$ . The eigenvalue given by this perturbation is

$$\lambda(k) = 2\epsilon + \alpha - 1 - k^2 - 2\epsilon \exp(-\sigma k), \quad (2.4)$$

where  $k = |\mathbf{k}|$ . The most unstable mode, obtained by imposing  $\partial\lambda/\partial k = 0$ , is

$$k_c = \sigma \epsilon \exp(-\sigma k_c). \quad (2.5)$$

Replacing Eq. (2.5) in Eq. (2.4), the bifurcation where the homogeneous full-populated state becomes unstable corresponds to  $\lambda = 0$ . At the bifurcation point,  $k_c^0 = \left(\sqrt{1 + \sigma^2(2\epsilon + \alpha - 1)} - 1\right) / \sigma$ . Thus, the threshold of the symmetry breaking bifurcation is given by

$$\beta = \epsilon \sigma^2 \exp[-\beta], \quad (2.6)$$

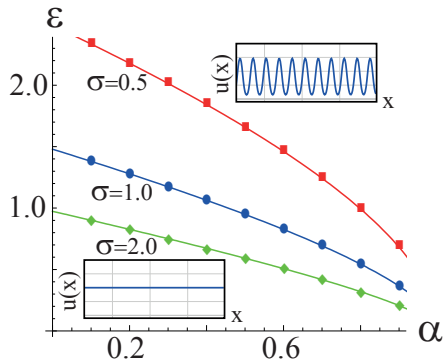


Figure 2.2: Instability region of the nonlocal equation (2.3) in 1D. Red squares, blue circles and green diamonds show the instability threshold for  $\sigma = 0.5$ ,  $\sigma = 1.0$  and  $\sigma = 2.0$  respectively, obtained from numerical simulations of Eq. (2.3). The instability threshold predicted by Eq. 2.6 is given by the solid lines for different  $\sigma$ , as shown. The lower (upper) inset shows a typical homogeneous (pattern) state. The parameter is  $n = 2$ .

where  $\beta = \sqrt{1 + \sigma^2(2\epsilon + \alpha - 1)} - 1$ .

Above the bifurcation, periodic states emerge (an example is shown in the upper inset of Figure 2.2). The wavelength is intrinsic to the dynamics of the system. The Eq. (2.3) in one dimension with a weak nonlocal coupling mediated by an exponential function has been studied [101, 102]. In two dimensions, this spatial instability can generate different patterns such as stripes and hexagons.

Figure 2.2 illustrates that Eq. (2.6) fits with the numerical results obtained from Eq. 2.3. The lower inset shows the homogeneous state  $u = 1$  and the upper inset shows a typical pattern state after the bifurcation. The spatial instability threshold appears by increasing the values of  $\sigma$ ,  $\epsilon$  or  $\alpha$  as shown in Figure 2.2.

## 2.4 Single fronts

A solution that connects two different states is called a front. Fronts can be classified into four main types: i) Fronts that connect one stable and one unstable homogeneous steady state, which have been investigated in depth [29, 30, 121]. ii) Fronts that connect two stable homogeneous steady states [122–125]. iii) Fronts that connect one stable homogeneous steady state and one stable pattern [126]. iv) Fronts that connect two stable patterns [126]. Numerical simulations of Eq. (2.3) in Figure 2.3 show a front that connects two stable homogeneous steady states with fixed boundary conditions. The area that connects both states is called interface or core, and it is illustrated also in Fig 2.3. The interface of the front can have some speed in the direction of the less favorable state, we call this speed the front speed. The point where both states are equally favorable is called the Maxwell point [125, 127, 128]. At this point ( $\alpha = 1/2$ ), the front is motionless.

We focus on a bistable regime, far from any pattern forming instability. We consider a front solution of Eq. (2.3) connecting the two stable homogeneous states.

In the case without nonlocal coupling ( $\epsilon = 0$ ), at the Maxwell point, the solution of the front that connects the bare state  $u = 0$  with the full populated state  $u = 1$  is [125]

$$u_{\pm}(x - x_0) = \frac{1}{2} \left( 1 \pm \tanh \left( \frac{x - x_0}{2\sqrt{2}} \right) \right), \quad (2.7)$$

where  $x_0$  is the core of the front. The asymptotic behavior of the front  $u_+$  at  $x = -\infty$  is  $u_+ = \exp \left( (x - x_0)/\sqrt{2} \right)$ . The asymptotic behavior at  $x = \infty$  is  $u_+ = 1 - \exp \left( -(x - x_0)/\sqrt{2} \right)$ . Figure 2.3 illustrates numerical solutions of the model Eq. (2.3) with  $\alpha = 1/2$  and  $\epsilon = 0$ , which correspond to the solution (2.7).

We introduce a small parameter  $\eta$  which measures the distance to the Maxwell point as  $\alpha = 1/2 - \eta$ , with  $\eta \ll 1$ . Numerical simulations of

Eq. (2.3) are illustrated in Figure 2.4. We observe that, when  $\eta \neq 0$ , the front solution moves with a constant speed. Then, we use the ansatz

$$u_k(x, t) = u_+(x - x_0(t)) + W(x, u_+), \quad (2.8)$$

where  $W(x, x_+)$  and  $\partial_t x_0$  are small corrections. All the temporal dependence is through  $x_0(t)$ . Note that, the same analysis could be formulated for  $u_-(x, t)$ .

By introducing the ansatz (2.8) in Eq. (2.3), we obtain

$$-\partial_x u_+ \partial_t x_0 = \eta(u_+ - u_+^2) + LW + h.o.t, \quad (2.9)$$

where *h.o.t* is the acronym for “high order terms” which are negligible in our analysis. The linear operator  $L$  has the form

$$L = -\frac{1}{2} + 3u_+(1 - u_+). \quad (2.10)$$

We use the inner product defined through

$$\langle g|h \rangle = \int_{-\infty}^{\infty} g(x) h(x) dx, \quad (2.11)$$

where  $g(x)$  and  $h(x)$  are real functions.

With this inner product, the linear operator  $L$  is self-adjoint and  $\partial_x x_+$  is an element of its kernel ( $L\partial_x x_+ = 0$ ). At the first order in  $\eta$ , applying the solvability condition to Eq. (2.9), we get

$$-\partial_t x_0 \langle \partial_x u_+ | \partial_x u_+ \rangle = \eta \langle \partial_x u_+ | u_+(1 - u_+) \rangle.$$

Solving the inner product, we find that the speed of the front is

$$\partial_t x_0 = -\sqrt{2}\eta.$$

Indeed, as we mention above, the front is motionless for  $\eta = 0$ . If  $\eta > 0$ , the populated state will invade the bare state. If  $\eta < 0$ , the bare state will invade the populated state.

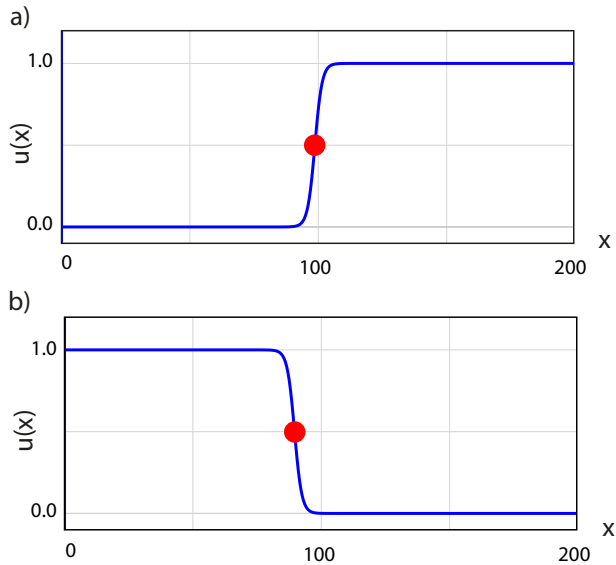


Figure 2.3: Front profile obtained from numerical simulations of Eq. (2.3). The parameters are  $\alpha = 1/2$  and  $\epsilon = 0$ . Figures a) and b) illustrate the solutions  $u_+$  and  $u_-$  in Eq. (2.7).

In order to analyze the effect of the strong nonlocal coupling in the asymptotic behavior of the front profile at the Maxwell point, we explore the vicinity of  $\epsilon = 0$ . Around the barren state ( $u = 0$ ), the inclusion of the nonlocal interaction does not modify the asymptotic behavior of the front, since the nonlocality in model (2.3) is nonlinear. We then examine the effect of the nonlocal term around the uniformly vegetated state ( $u = 1$ ). For this purpose, we assume that the asymptotic behavior of the front obeys an exponential law of the form

$$u_+(x \gg x_0) = 1 - a \exp(-b(x - x_0)),$$

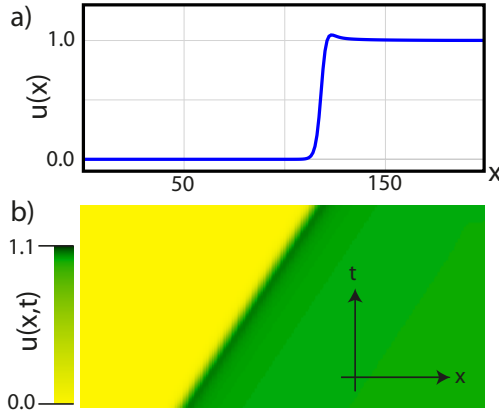


Figure 2.4: Front propagation obtained from numerical simulations of Eq. (2.3). (a) Front profile. (b) Spatiotemporal diagram that shows the front movement with a constant speed. The parameters are  $\alpha = 0.51$ ,  $\sigma = 0.7$ ,  $n = 2$ , and  $\epsilon = 1.0$ .

where  $a$  is a constant. The exponent  $b$  obeys the equation

$$b^2 - \frac{1}{2} + \epsilon [3 - 2g_\sigma(b)] = 0, \quad (2.12)$$

where

$$g_\sigma(b) = \int_{-\infty}^{\infty} \cosh(bx) f_\sigma(x) dx. \quad (2.13)$$

Equation (2.12) has been used to explain the emergence of localized domains. When  $b$  has an imaginary part, spatially damped oscillations on the front profile are induced, leading to the stabilization of localized domain. This mechanism is well documented for local and nonlocal one-dimensional systems [101, 107, 108, 125].

However, the function  $g_\sigma(b)$  exists when the kernel decays faster than exponential, i.e. a weak nonlocal coupling. In the case of strong nonlocal

interaction,  $g_\sigma(b)$  diverges and the above analysis is not valid. To avoid this problem, we perform an expansion of the solution  $u(x)$  in the small parameter  $\epsilon$  as follows

$$u(x) = u_0(x) + \epsilon u_1(x) + \epsilon^2 u_2(x) + \dots, \quad (2.14)$$

where  $u_0 = u_+$  is the motionless front given by Eq. (2.7). Introducing (2.14) in Eq. (2.3) and performing expansion in terms of  $\epsilon$ , we get at the first order

$$(\partial_{xx} - 1/2 + 3u_0(1 - u_0)) u_1 = u_0 \int_{-\infty}^{\infty} u_0^2(x + x') f_\sigma(x') dx' - u_0^3.$$

If we center our approach in the region where  $x \gg x_0$ , neglecting all the exponential correction, we find

$$(\partial_{xx} - 1/2) u_1 = - \int_{x-x_0}^{\infty} f_\sigma(x') dx'. \quad (2.15)$$

As  $x - x_0 \gg 1$ , we approximate the function  $f_\sigma(x')$ , defined by Eq. (2.1), in the following manner

$$f_\sigma(x') \approx \frac{\sigma^n N_n}{x'^n}.$$

Then, the asymptotic behavior of the front in the limit  $x \rightarrow +\infty$  is given by

$$u(x) \approx 1 + \frac{2\epsilon\sigma^n N_n}{(n-1)(x-x_0)^{n-1}}. \quad (2.16)$$

Equation (2.16) tells us that just one single peak exists in the profile. This peak grows with the intensity and the range of the nonlocal interaction. Figure 2.5 illustrates this result and numerical simulation of Eq. (2.3). Figure a) shows the profile of the front. Figure b) shows the profile of the front around  $u = 1$  and the asymptotic behavior in a semi-log scale

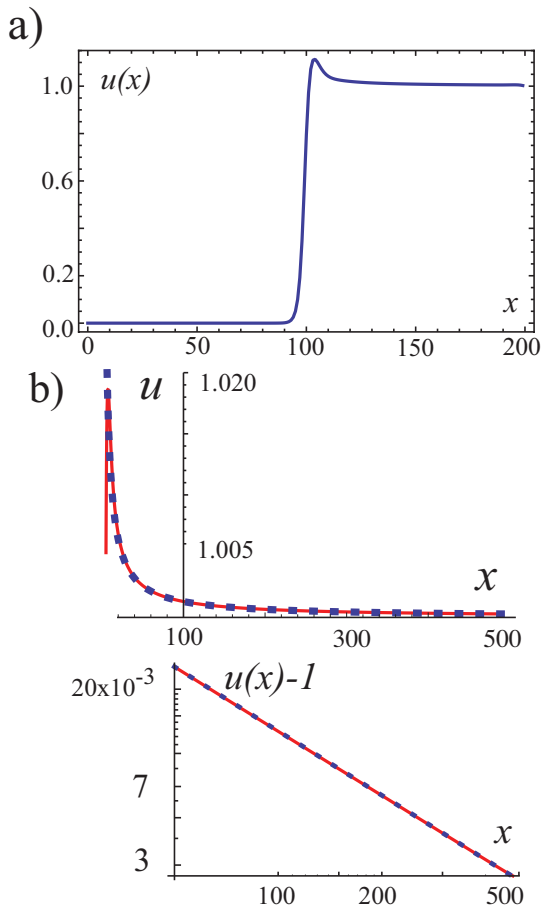


Figure 2.5: Numerical solutions of model (2.3) with the Lorentzian kernel (2.1). (a) Front profile at the Maxwell point  $\alpha = 0.5$ ; other parameters are  $\sigma = 2.0$ ,  $n = 2.0$  and  $\epsilon = 0.35$ . (b) Decay of front to the uniformly vegetated state for  $\alpha = 0.5$ ,  $\sigma = 2.0$ ,  $n = 2.0$  and  $\epsilon = 0.1$ . In (b), the top panel shows the comparison between the numerical calculation (dotted line) and the analytical estimation (2.16) (continuous line), while the bottom panel displays the same comparison in a semi-log plot. Figure credit: Daniel Escaff.

that confirms the power law in Eq. (2.16). We can observe an agreement without any fit parameter between our theoretical and numerical results. Note that, the numerical results also predict the existence of only one peak in the profile near the core. This single peak is in concordance with the feature of fairy circles in their border, where one can observe only one peak of higher vegetation in the edge between the bare state and the matrix of vegetation.

## 2.5 Fairy circles

Far from a symmetry breaking instability, localized structures can be stabilized as a consequence of fronts interaction. This behavior occurs when the spatial profile of the front has damped oscillations in the localized structure [101, 107, 108, 125]. This mechanism is not applicable to the formation of fairy circles because the oscillations around the bare state are not allowed. Here, we show that bistability and strong nonlocal coupling can stabilize localized structures without damped oscillations. Also we show some features of these structures that are in agreement with fairy circles such as the relations between the area and the rainfall or the maximum in the biomass found along the border of fairy circles.

Equation (2.3) admits stable localized structures with a flat area in one and two dimensions. Figure 2.6 illustrates these structures that we interpreted as fairy circles. Numerical simulations show that these structures have one single fringe of higher biomass along their border (See Figure 2.6), as is observed in fairy circles in Namibia (See Figure 1.5a). This feature can be explained since the vegetation on the border of fairy circles has access to more water from the bare soil in the circle. In other words, the vegetation along the border has less competition than the vegetation in the matrix. This result is in agreement with Eq. (2.16), where we showed that one single front has one maximum in the core.

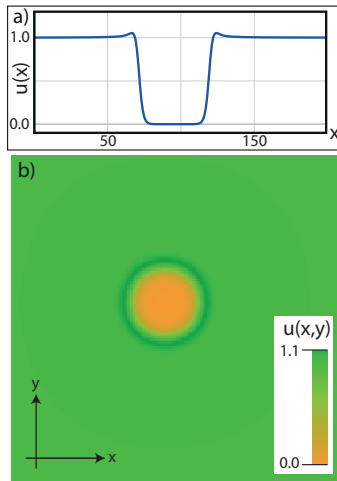


Figure 2.6: Stationary fairy circle performed by numerical simulations of Eq. (2.3). (a) One dimension with  $\alpha = 0.492$ ,  $\sigma = 0.8$ ,  $n = 2.0$  and  $\epsilon = 0.5$ . (b) Two dimensions with  $\alpha = 0.46$ ,  $\sigma = 0.1$ ,  $n = 2.5$  and  $\epsilon = 10.0$ .

In this section, we describe analytically the fairy circles in one dimension. In order to solve this problem, we center our analysis on a region far from the spatial instability showed in Eq. (2.6). In addition, we focus on a region near the Maxwell point and considering small intensity of the nonlocal coupling. We assume that a fairy circle in one dimension is the superposition of two fronts, which come from Eq. (2.7), with an extra small perturbation. Then, our ansatz is

$$u(x, t) = u_+(x - \delta(t)) + u_-(x + \delta(t)) + W(x, u_+, u_-), \quad (2.17)$$

where  $2\delta$  is the size of the localized structure,  $W$  is a small correction and  $u_{\pm}$  are defined in Eq. (2.7).

Replacing the ansatz (2.17) in Eq. (2.3), and neglecting smaller terms, we

obtain

$$\begin{aligned}
-(\partial_x u_+ - \partial_x u_-)\partial_t \delta &= LW + 3u_+ u_- (1 - u_+ - u_-) \\
&\quad - \eta(u_+ + u_-)(u_+ + u_- - 1) \\
&\quad + \epsilon u \int_{-\infty}^{\infty} K(x') u^2(x + x', t) dx', \quad (2.18)
\end{aligned}$$

where the linear operator  $L$  is given by

$$L = -\frac{1}{2} - 6u_+ u_- + 3(u_+ + u_- - u_+^2 - u_-^2). \quad (2.19)$$

We consider again the inner product (2.11). Then,  $L$  is self-adjoint. Note that  $\partial_x u_+$  and  $\partial_x u_-$  are not eigenfunctions of  $L$ . However, when we neglect exponentially small corrections,  $L\partial_x u_{\pm} \approx 0$ . Applying the inner product between  $\partial_x u_+$  and Eq. (2.18), and neglecting small corrections, we get

$$-\partial_t \delta \langle \partial_x u_+ | \partial_x u_+ \rangle = \eta \langle \partial_x u_+ | u_+(1 - u_+) \rangle + \epsilon G,$$

where

$$G = \left\langle \partial_x u_+ | u_+ \int_{-\infty}^{\infty} K(x') (u_+(x + x', t) + u_-(x + x', t))^2 dx' \right\rangle.$$

As we are near the Maxwell point, the distance between the fronts is large, i.e.,  $\delta \gg 1$ . Neglecting smaller terms than  $\epsilon/\delta^{n-1}$ , we obtain

$$\partial_t \delta = \frac{3\sqrt{2}\epsilon N_n \sigma^n}{(n-1)(2\delta)^{n-1}} - \sqrt{2}\eta. \quad (2.20)$$

Obviously, this equation is valid in the limit  $\partial_t \delta \sim \epsilon/\delta^{n-1} \sim \eta \ll 1$ . Let us set  $n = 2$  and  $N_2 = 1/\pi\sigma$ . Then, Eq. (2.20) becomes

$$\partial_t \Delta = \frac{6\sqrt{2}\epsilon\sigma}{\pi\Delta} - 2\sqrt{2} \left( \frac{1}{2} - \alpha \right), \quad (2.21)$$

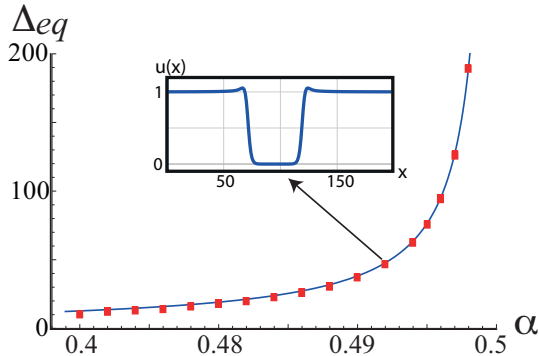


Figure 2.7: Width of fairy circles as a function of the aridity parameter  $\alpha$  in one dimension. The blue solid line corresponds to the theoretical result in Eq. (2.22). The red squares were performed by numerical simulations of Eq. (2.3). The inset represent the profile of the population (or biomass density) in at the indicated value. The parameters are  $\sigma = 0.8$ ,  $n = 2$ , and  $\epsilon = 0.5$ .

where  $\Delta = 2\delta$  is the distance separating the two interacting fronts. This distance has an equilibrium state given by

$$\Delta_{eq} = \frac{3\epsilon\sigma}{\left(\frac{1}{2} - \alpha\right)\pi}. \quad (2.22)$$

Then, the width of fairy circles increases as a function of the aridity  $\alpha$ . At the Maxwell point, the size of the structure diverges. Numerical simulations of the full model (2.3) are illustrated in Figure 2.7. These numerical simulations are in agreement with our theoretical results, without any fit parameter. However, this simple result does not give us information about the minimum value of  $\alpha$  where fairy circles exist (in Figure 2.7, this value is  $\alpha \approx 0.4$ ).

The linear stability analysis of the solution (2.22) in Eq. (2.21) gives the



*Figure 2.8: Flat spot in Namibia. The photo has been taken on March 1st, 2015.*

eigenvalue

$$\lambda = -\frac{2\sqrt{2}\pi\left(\frac{1}{2} - \alpha\right)^2}{3\sigma\epsilon}.$$

Then, we can conclude that the width of fairy circles is stable for competition between plants ( $\epsilon > 0$ ). Note that, in the case of facilitation between plants ( $\epsilon < 0$ ), the localized structure becomes unstable. This result shows that strong nonlocal competition, and not facilitation, is the key ingredient to stabilize fairy circles.

## 2.6 Flat spots

We have analyzed in the previous section the formation of fairy circles. We have shown that their domain of existence ranges  $\alpha < 1/2$ . In this section

we analyze another type of localized structures which we call flat spots. The flat spots consist in a circular flat area covered by vegetation and a matrix of bare soil. An example of such behavior is shown in Figure 2.8. This photo has been obtained in Namibia, in a region near to fairy circles. Numerical simulations of the Nagumo model with Lorentzian-like nonlocal coupling, Eq. (2.3), have been performed. Figure 2.9 shows a numerical example of flat spots in one and two dimensions. The boundary conditions in the numerical simulations are fixed at  $u = 0$ . In order to obtain flat spots, it is necessary an initial condition with enough vegetation to develop them. Note that, these localized structures are far from any symmetry breaking instability and devoid of oscillatory tails.

Here, we study analytically and numerically the formation of flat spots in one dimension. The flat spots exist for aridity values higher than the Maxwell point ( $\alpha > 1/2$ ). In what follows, we analyze in one dimension their formation. We consider  $\epsilon \ll 1$  and  $\alpha - 1/2 = \eta \ll 1$  in order to develop our mathematical analysis. Here, our ansatz for one flat spot is given by

$$u(x, t) = u_+(x + \delta(t)) + u_-(x - \delta(t)) - 1 + W, \quad (2.23)$$

where  $W$  is small correction,  $u_{\pm}$  is defined in Eq. (2.7) and the width of the flat spot is  $2\delta$ . Introducing the ansatz (2.23) in Eq. (2.3) and neglecting high order terms, we derive

$$\begin{aligned} (\partial_x u_+ - \partial_x u_-) \partial_t \delta &= -(u_+ + u_- - 1)(u_+ + u_- - 2) \left( u_+ + u_- - \frac{3}{2} \right) \\ &+ \epsilon (u_+ + u_- - 1) \int_{-\infty}^{\infty} K(x') u^2(x + x', t) dx' \\ &+ \eta \left( (u_+ + u_- - 1)^2 - (u_+ + u_- - 1) \right) \\ &+ \partial_{xx} (u_+ + u_-) + LW, \end{aligned} \quad (2.24)$$

where the linear operator  $L$  is given by

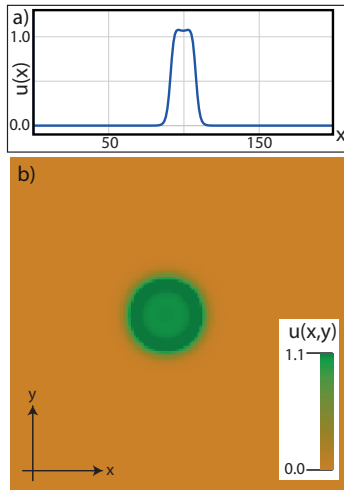


Figure 2.9: Stationary flat spot performed by numerical simulations of Eq. (2.3). (a) One dimension with  $\alpha = 0.52$ ,  $\sigma = 0.8$ ,  $n = 2.0$  and  $\epsilon = 0.5$ . (b) Two dimensions with  $\alpha = 0.56$ ,  $\sigma = 0.1$ ,  $n = 2.5$  and  $\epsilon = 10.0$ .

$$L = -3(u_+ + u_- - 1)^2 + 3(u_+ + u_- - 1) - \frac{(u_+ + u_- - 1)}{2}. \quad (2.25)$$

We use the inner product defined in Eq. (2.11). Applying the inner product between  $\partial_x u_+$  and Eq. (2.24), neglecting small corrections, we obtain

$$\partial_t \delta \langle \partial_x u_+ | \partial_x u_+ \rangle = -\eta \langle \partial_x u_+ | u_+(1 - u_+) \rangle + \epsilon G,$$

where

$$G = \left\langle \partial_x u_+ \left| u_+ \int_{-\infty}^{\infty} K(x') (u_+(x + x', t) + u_-(x + x', t) - 1)^2 dx' \right. \right\rangle.$$

As we are near to the Maxwell point,  $\delta \gg 1$ . Then, neglecting terms smaller

than  $\epsilon/\delta^{n-1}$ , we get

$$\partial_t \delta = \frac{3\sqrt{2}\epsilon N_n \sigma^n}{(n-1)(2\delta)^{n-1}} - \sqrt{2}\eta. \quad (2.26)$$

This equation is valid in the limit  $\partial_t \delta \sim \epsilon/\delta^{n-1} \sim \eta \ll 1$ . In order to have a well defined integral, necessarily we have  $n > 1$  in one dimension. Note that, this result shows us that competition between plants generates a repulsive front interaction, which may generate flat spots.

We fix the value  $n = 2$  and  $N_2 = 1/\pi\sigma$ . Then, Eq. (2.26) becomes

$$\partial_t \Delta = \frac{6\sqrt{2}\epsilon\sigma}{\pi\Delta} - 2\sqrt{2} \left( \alpha - \frac{1}{2} \right), \quad (2.27)$$

where  $\Delta = 2\delta$  is the size of the localized structures. The size has an equilibrium state given by

$$\Delta_{eq} = \frac{3\epsilon\sigma}{\pi \left( \alpha - \frac{1}{2} \right)}. \quad (2.28)$$

At the Maxwell point,  $\alpha = 1/2$ , the width of the localized structure diverges. At lower levels of adversity ( $\alpha < 1/2$ ), flat spots do not exist.

In order to check the formula (2.28), we perform numerical simulations of the full model (2.3) and compare them with the equilibrium width provided by Eq. (2.28). Figure 2.10 illustrates the size of flat spots as a function of the aridity. Then, numerical simulations in the full model (2.3) agree with the result in Eq. (2.28). The size of flat spots decreases with the aridity. In fact, we can expect that the total area of vegetation decreases as the aridity increases (for example, when the rainfall decreases).

The linear stability analysis of the solution (2.28) in Eq. (2.27) gives the eigenvalue

$$\lambda = -\frac{2\sqrt{2}\pi \left( \alpha - \frac{1}{2} \right)^2}{3\sigma\epsilon}.$$

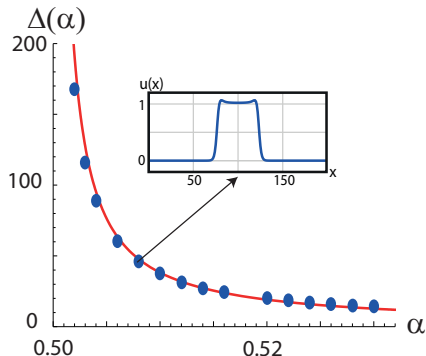


Figure 2.10: Width of a flat spot, as a function of aridity  $\alpha$  in one dimension. The solid line corresponds to the analytical prediction from Eq. (2.28). The dots are performed by numerical simulations of Eq. (2.3). The inset is the spatial profile of biomass. The parameters are  $\sigma = 0.8$ ,  $n = 2$  and  $\epsilon = 0.5$ .

With this result, we can conclude that the width of flat spots is stable for plant competition ( $\epsilon > 0$ ). On the other hand, facilitation between plants ( $\epsilon < 0$ ) generate an attractive interaction between fronts. That attractive interaction changes the flat spots from stable to unstable.

## 2.7 Conditions for the appearance of fairy circles and flat spots

In this section, we establish the bifurcation diagram for both types of localized vegetation structures. We fix the length of the competition between plants  $\sigma$ , and we vary the degree of aridity  $\alpha$  and the strength of the competitive interaction  $\epsilon$ . We numerically establish a stability range of a single fairy circle and the localized patch in a one-dimensional setting. This analysis is summarized in the parameter plane  $(\alpha, \epsilon)$  of Figure 2.11.

For  $\alpha < 1/2$ , a single fairy circle is stable in the region FC, as indicated in Figure 2.11. This stability region is bounded from below by dots and bounded from the left by the Maxwell point ( $\alpha = 1/2$ ). Dynamically speaking, dots correspond to a saddle-node bifurcation. The parameter zone A indicates the regime where a fairy circle shrinks and disappears.

For large values of the strength of the competition  $\epsilon$ , the uniformly vegetated state becomes unstable via a pattern-forming instability. The threshold associated with this instability is represented by a solid line. This line is obtained by plotting formula Eq. (2.6). This spatial instability avoid the existence of fairy circles in the region C and may allow for the formation of periodic structures.

For  $\alpha > 1/2$ , a single fairy circle grows at infinity and disappears and a flat spot appears. This structure is stable in the region FS, as shown in the bifurcation diagram of Figure 2.11. The region B corresponds to a high degree of aridity. In this zone of parameters, a localized patch shrinks and disappears, and the transition towards a bare state occurs.

## 2.8 Interaction of fairy circles

In the previous sections, we have shown where a single fairy circle exists and we have estimated analytically and numerically its size when it is isolated in space (without interaction with other fairy circles). In this section, we analyze the situation where two or more fairy circles are present in the same system.

The interaction of fairy circles affects their size. More precisely, the size of a single fairy circle decreases in the presence of others. This feature could be explained by the fact that adding an extra fairy circle provides a reservoir of more water in its surrounding. This reservoir of extra water provides a similar effect as decreasing the aridity in the system. In fact, in agreement

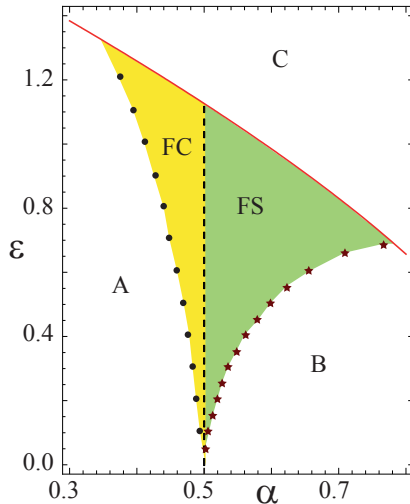


Figure 2.11: Bifurcation diagram of localized structures for model Eq. (2.3) in one dimension, in parameter plane  $(\alpha, \epsilon)$ . The other parameters are  $\sigma = 0.8$  and  $n = 2$ .

with field observations, the size of the fairy circle decreases as the aridity decreases.

However, the change in the size is not the only effect that can be detected. Another important feature is that the interaction of fairy circles is repulsive. Figure 2.12 illustrates the time evolution of two fairy circles obtained by numerical simulations of Eq. (2.3). As can be seen from this figure, the distance between two fairy circles increases until they are close enough to the borders of the system. The boundary conditions in the numerical simulations are fixed to one.

In order to study the interaction of fairy circles, we focus on the one dimensional system with the exponent of the Lorentzian-like function  $n = 2$ ,  $\epsilon \ll 1$  and  $\alpha - 1/2 \ll 1$ . To start, we consider a system with two fairy circles

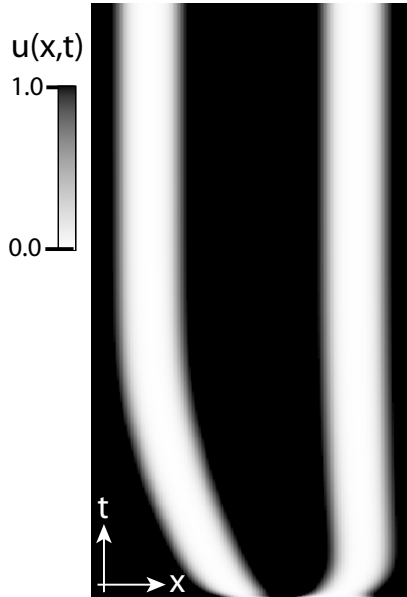


Figure 2.12: Spatio-temporal diagram of the interaction of two fairy circles in one dimension in the nonlocal model (2.3). The parameters are  $\alpha = 0.48$ ,  $\epsilon = 0.5$ ,  $\sigma = 0.8$  and  $n = 2$ . The boundary condition is  $u = 1.0$ .

as shown in Figure 2.13. To simplify the analysis, without loss of generality, we choose the origin ( $x = 0$ ) at the center of the fairy circle located on the left hand side corresponding to the red dot in Figure 2.13. These two fairy circles are separated by a distance  $L$ . We consider the following ansatz corresponding to the linear superposition of two fairy circles in which we add a small perturbation  $W$ :

$$\begin{aligned}
 u_{2FC}(x, t) = & u_+(x - 3\Delta(t)/2 - L(t)) + u_-(x - \Delta(t)/2 - L(t)) \\
 & + u_-(x + \Delta(t)/2) + u_+(x - \Delta(t)/2) - 1 + W, \quad (2.29)
 \end{aligned}$$

where  $u_{\pm}$  are defined in Eq. (2.7). We assume in addition that the two

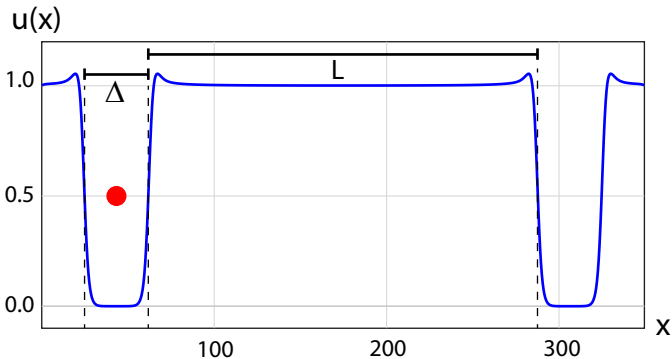


Figure 2.13: Two stationary fairy circles interacting in one dimension. The results were carried out from numerical simulations of Eq. (2.3). The borders are fixed at  $u = 1$ . The parameters are  $\alpha = 0.49$ ,  $\sigma = 0.8$ ,  $n = 2.0$  and  $\epsilon = 0.5$ .

interacting fairy circles are far from each other, i.e.  $L \gg 1$ . We also consider large width solutions, i.e.  $\Delta \gg 1$ .

Replacing the ansatz (2.29) in the Eq. (2.3) and calculating the inner product (2.11) with  $\partial_x u_+(x - \Delta/2)$ , we obtain

$$\partial_t \Delta = \frac{6\sqrt{2}\epsilon\sigma}{\pi} \left( \frac{1}{\Delta} - \frac{1}{L} + \frac{1}{L + \Delta} \right) - 2\sqrt{2} \left( \frac{1}{2} - \alpha \right). \quad (2.30)$$

The equilibrium width is solution of the following equation:

$$\frac{1}{2} - \alpha = \frac{3\epsilon\sigma}{\pi} \left( \frac{1}{\Delta} - \frac{1}{L} + \frac{1}{L + \Delta} \right) \quad (2.31)$$

We can easily solve Eq. (2.31) in terms of  $\Delta$ . The results are plotted in Figure 2.14. The solid line indicate the plot of  $\Delta$  as a function of  $L$  for

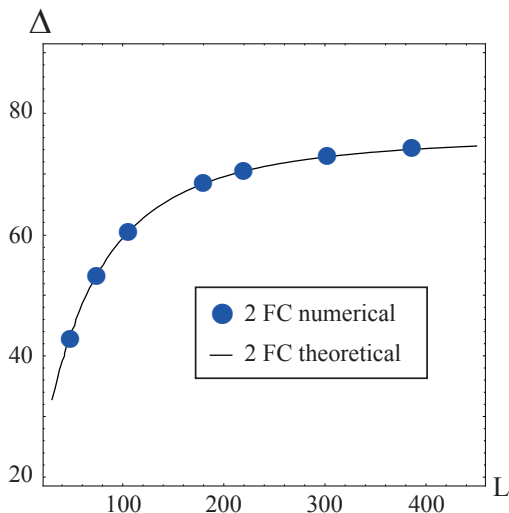


Figure 2.14: Width  $\Delta$  of two fairy circles interacting as a function of the distance  $L$  between them. The parameters are  $\alpha = 0.495$ ,  $\sigma = 0.8$ ,  $n = 2$  and  $\epsilon = 0.5$ .

fixed parameters. In this figure, we add results for numerical simulations of the full model Eq. (2.3) with blue dots. Figure 2.14 shows an agreement between the results obtained from Eq. (2.31) and the ones estimated by numerical simulations of the full model Eq. (2.3).

To study the interaction among  $N$  fairy circles, first we calculate the effect of the interaction between an odd number  $(2N + 1)$  of fairy circles. Second, we achieve the equivalent result for an even number  $(2N)$  of fairy circles.

Let us consider a solution of Eq. (2.3) with an odd number of fairy circles, as illustrated in Figure 2.15. The linear superposition of an odd number of fairy circles with a small perturbation  $W$  reads as follows

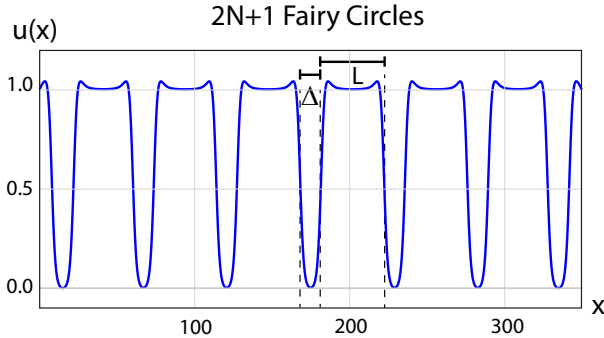


Figure 2.15: Seven stationary fairy circles interacting in one dimension. The results were performed by numerical simulations of Eq. (2.3). The borders are fixed at  $u = 1$ . The parameters are  $\alpha = 0.49$ ,  $\sigma = 0.8$ ,  $n = 2.0$  and  $\epsilon = 0.5$ .

$$\begin{aligned}
 u_{(2N)FC}(x, t) &= +u_-(x + \Delta(t)/2) + u_+(x - \Delta(t)/2) \\
 &+ \sum_{i=1}^N \left( u_-(x + \Delta(t)/2 - i(\Delta + L)) \right. \\
 &\quad \left. + u_+(x - \Delta(t)/2 - i(\Delta + L)) \right) \\
 &+ \sum_{i=1}^N \left( u_-(x + \Delta(t)/2 + i(\Delta + L)) \right. \\
 &\quad \left. + u_+(x - \Delta(t)/2 + i(\Delta + L)) \right) \\
 &- 1 - 2N + W,
 \end{aligned} \tag{2.32}$$

where  $u_{\pm}$  are defined in Eq. (2.7),  $L$  is the distance between the central fairy circle and one of its neighbors and  $\Delta$  is the size of the central fairy circle.

Then, replacing  $u_{(2N)FC}(x, t)$  in Eq. (2.3) and calculating the inner product

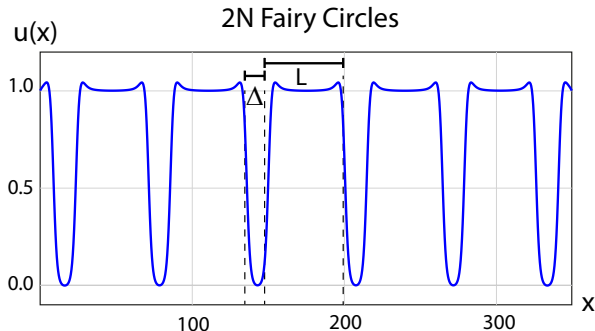


Figure 2.16: Six stationary fairy circles interacting in one dimension. The results were carried out from numerical simulations of Eq. (2.3). The borders are fixed at  $u = 1$ . The parameters are  $\alpha = 0.49$ ,  $\sigma = 0.8$ ,  $n = 2.0$  and  $\epsilon = 0.5$ .

(2.11) with  $\partial_x u_+(x - \Delta/2)$ , we find

$$\begin{aligned} \partial_t \Delta &= \frac{6\sqrt{2}\epsilon\sigma}{\pi} \left( \frac{1}{\Delta} - \sum_{i=1}^N \frac{2\Delta}{i^2 (\Delta + L)^2 - \Delta^2} \right) \\ &\quad - 2\sqrt{2} \left( \frac{1}{2} - \alpha \right). \end{aligned} \quad (2.33)$$

Then, the equilibrium width associated to an odd number of fairy circles is a solution of the equation

$$\frac{1}{2} - \alpha = \frac{3\epsilon\sigma}{\pi} \left( \frac{1}{\Delta} - \sum_{i=1}^N \frac{2\Delta}{i^2 (\Delta + L)^2 - \Delta^2} \right). \quad (2.34)$$

For solutions involving an even number of fairy circles, like the one illustrated in Figure 2.16, a similar analysis as above leads to the time evolution equation for the width

$$\partial_t \Delta = \frac{6\sqrt{2}\epsilon\sigma}{\pi} \left( \frac{1}{\Delta} - \sum_{i=1}^N \frac{2\Delta}{i^2 (\Delta + L)^2 - \Delta^2} \right)$$

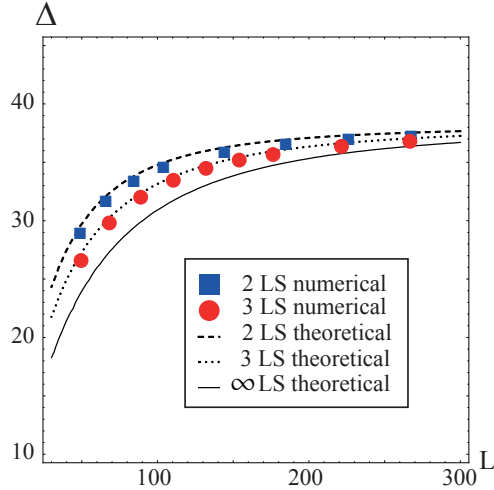


Figure 2.17: Width  $\Delta$  as a function of the distance  $L$  among fairy circles. The number of fairy circles is mentioned in the inset. The parameters are  $\alpha = 0.49$ ,  $\sigma = 0.8$ ,  $n = 2$  and  $\epsilon = 0.5$ .

$$+ \frac{\Delta}{N(\Delta + L)(N(\Delta + L) + \Delta)} - 2\sqrt{2} \left( \frac{1}{2} - \alpha \right), \quad (2.35)$$

where  $\Delta$  is the width of one the central fairy circles and  $L$  is the distance between the central fairy circles. The equilibrium width for an even number of fairy circles is solution of the following equation:

$$\begin{aligned} \frac{1}{2} - \alpha &= \frac{3\epsilon\sigma}{\pi} \left( \frac{1}{\Delta} - \sum_{i=1}^N \frac{2\Delta}{i^2(\Delta + L)^2 - \Delta^2} \right. \\ &\quad \left. + \frac{\Delta}{N(\Delta + L)(N(\Delta + L) + \Delta)} \right). \end{aligned} \quad (2.36)$$

When  $N$  is large, Eq. (2.34) and (2.36) become

$$\frac{1}{2} - \alpha = \frac{3\epsilon\sigma}{\pi} \left( \frac{1}{\Delta} - \sum_{i=1}^{\infty} \frac{2\Delta}{i^2(\Delta + L)^2 - \Delta^2} \right).$$

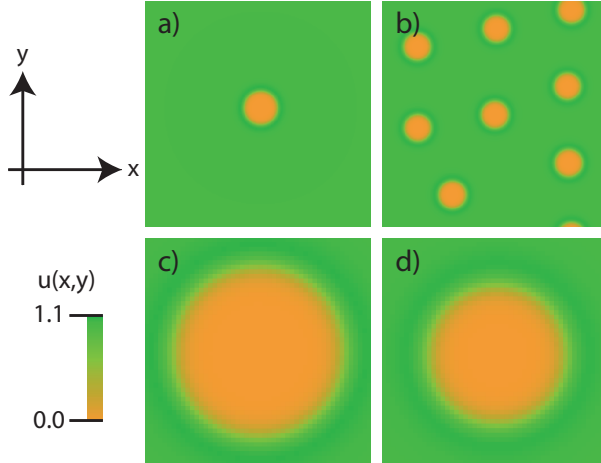


Figure 2.18: Difference in size between isolated fairy circle and a fairy circle surrounded by several others in two dimensions. The results are performed by numerical simulations of Eq. (2.3). Figure a) shows an isolated fairy circle in a system of length  $256 \times 256$ . Figure b) shows a fairy circle surrounded by other seven. Figure c) and d) are a zoom ( $60 \times 60$ ) of a) and b) respectively. The parameters are  $\alpha = 0.45$ ,  $\sigma = 0.1$ ,  $n = 2.5$  and  $\epsilon = 10$ .

Then

$$\sum_{i=1}^{\infty} \frac{2\Delta}{i^2 (\Delta + L)^2 - \Delta^2} = \frac{L + \Delta - \pi\Delta \cot\left(\frac{\pi\Delta}{L+\Delta}\right)}{\Delta(L + \Delta)},$$

and we obtain

$$\frac{1}{2} - \alpha = \frac{3\epsilon\sigma}{L + \Delta} \cot\left(\frac{\pi\Delta}{L + \Delta}\right). \quad (2.37)$$

At the Maxwell point  $\alpha = 1/2$ , the argument of the cotangent function should be  $\pi\Delta/(L + \Delta) = \pi/2$ . This implies that  $L = \Delta$ .

The results obtained from Eq. (2.34), (2.36) and (2.37) are plotted in Figure 2.17. With even and odd number of fairy circles, we achieve a match between

these formulas and the results obtained from numerical simulations of the full model Eq. (2.3).

Nonetheless, the field observations are in a two dimensional system and our theoretical results are in one dimension. It is important to note that, in two dimension the result is qualitatively the same. In fact, Figure 2.18 shows a numerical example in two dimensions. We can observe how an isolated fairy circle is bigger than a fairy circle surrounded by other fairy circles. The area of the fairy circle in Fig a) and c) is around 50% bigger than the area of the central fairy circle in b) and d). Analytically, the 2D problem is out of the scope of this thesis. We shall investigate this problem in the near future at least for a large diameter of fairy circles.

## Chapter 3

# Fairy circles in vegetation models for arid regions

The purpose of this chapter is to report, in more realistic models of vegetation, on the occurrence of fairy circles with varying intrinsic size in a regime far from any Turing instability [120]. We consider the regime where the bistability between the bare and the uniformly vegetated states takes place. The size of the fairy circle is determined by the strong nonlocal competitive interaction between plants mediated by a Lorentzian type of kernel function. The size of the fairy circles is thus determined rather by the system's dynamical parameters and not by external factors such as termites or ants. In accordance with field observations, we demonstrate that the diameter of a fairy circle increases in more arid environments, and each isolated fairy circle exhibits one single fringe with high biomass density. In order to show that our mechanism is model-independent, we incorporate the Lorentzian-like nonlocal coupling in two ecological models: the generic interaction-redistribution model [11, 27] and the reaction-diffusion type of model that includes water transport [19, 62]. We prove that both models support stable fairy circles. We show that when fairy circles' di-

iameter exceeds a given maximum size, i.e. maximum aridity, it results in a deformation of their circular shape. When the aridity is lower than a given threshold, fairy circles shrink and disappear. Finally, we establish a bridge between the generic interaction-redistribution model [27,66] and the paradigmatic Nagumo model for population dynamics [73,101,102], and in one dimension, we derive analytically a formula which describes how the size of the fairy circle evolves as a function of aridity.

### 3.1 The strong nonlocal logistic-type model

To explain the formation of fairy circles in more realistic models of vegetation, we consider isotropic conditions in the system, including flat territories and homogeneous environmental conditions in time and space [11]. The topography in Namibia does not change in scale for the majority of the fairy circles (as illustrated in Figure 3.1a and 3.1b ). Thus the flat territory assumption is reasonable. The longtime scale of fairy circles [65,72] enables us to consider homogeneous environmental conditions.

The standard interaction-redistribution type of model takes into account the nonlocal interaction by facilitation or competition [11,27,129]. The facilitation in arid conditions is related in this model with the shade that plants generate, and their range of interaction is proportional to the diameter of the canopy of the aerial structures of the plants. In this arid climatic condition, plants should then compete for the extraction of water or nutrients. To do that, every plant spreads its roots to increase water or nutrients uptake. This adaptation increases competition between neighboring plants and at plant communities level, via nonlocal interaction, which accounts for the transport processes of water in the soil, and nutrients [11,27,66]. Then, the competition in arid regions is related to the competition by roots for the water/nutrients in the soil, and its range of interaction is given by the length of the roots. In the case of semiarid or arid regions, the typical range

of competition could be at least one order of magnitude higher than the facilitation.

We consider a single species that dominates the plant community behavior. The biomass density  $b(\mathbf{r}, t)$  describes the biomass per unit area, at point  $\mathbf{r} = (x, y)$  and at time  $t$ , of the dominant species. The spatio-temporal evolution of these plants, i.e. their growth and death processes, is described by the following logistic type of equation [27,66]

$$\partial_t b = b(1 - b)M_f - \mu b M_c + \nabla^2 b. \quad (3.1)$$

On the right-hand side, the first term accounts for the growth rate and the saturation of the biomass. In this term,  $M_f$  describes how the facilitation between plants increases the growth rate. The second term models the natural death of plants and their destruction by any external factor such as grazing of herbivores, harvesting of termites, or fire. In this term, the aridity  $\mu$  is the parameter which controls the mortality rate related to absence of water or any other adversity condition, and  $M_c$  accounts for the increasing of the plants' rate of mortality through the competition by roots. The last term,  $\nabla^2 b$  corresponds to the diffusion given by the seed dispersal and the lateral growth of the plants. In order to model aggressive competition, competition  $M_c$  and aridity  $\mu$  are in the same term in Eq. (3.1) [24,27]. Some models consider the competition in the saturation term, varying the carrying capacity, to describe similar general behaviors [14]. When  $M_f$  and  $M_c$  are constants, Eq. (3.1) corresponds to the standard logistic model. However, we consider  $M_f$  and  $M_c$  as functions of  $b$ . Indeed, both functions must be positive, grow with the biomass density, and go to one as  $b$  goes to zero.

When the water is scarce, plants adapt their roots in order to survive. This adaptation can increase the length of the roots or their strength to uptake water. Here, in contrast with other models of plant ecology which consider weak nonlocal competition [11, 19, 27], we define the competition as the

strong nonlocal function mediated by a Lorentzian-like kernel

$$M_c = \exp\left(\xi_c \int \frac{N_n b(\mathbf{r} + \mathbf{r}', t)}{1 + (|\mathbf{r}'|/L_c)^n} d\mathbf{r}'\right), \quad (3.2)$$

where  $\xi_c$  corresponds to the intensity of the competition,  $n$  describes how the nonlocal competition decays with the distance,  $L_c$  is the characteristic length of competition, and the normalization constant is

$$N_n = \left(\int \frac{N_n b(\mathbf{r} + \mathbf{r}', t)}{1 + (|\mathbf{r}'|/L_c)^n} d\mathbf{r}'\right)^{-1}.$$

The characteristic length  $L_c$  is related to the size of the roots, and its natural expression is given by  $L_c = L_0 b^p$ . The dependence of  $L_c$  on the variable  $b$  reveals the relation between the roots and the size of the plants and is called the allometric factor, where  $p$  is the allometric exponent and  $L_0$  is a constant. This relation is explicit in several works [19, 27, 62] and can generate some different behaviors [24]. Nevertheless, we use a constant  $L_c$  as a simplification in order to continue our analysis, i.e., we fix the allometric exponent  $p = 0$ . Then, we consider that the value  $L_c$  is the length of the roots.

Facilitation could be nonlocal as is the competition. This function  $M_f$  describes the positive feedback between plants that increases the vegetation growth. In the facilitation function  $M_f$ , the parameter  $\xi_f$  corresponds to the intensity of the competition and  $L_f$  is its characteristic length. However, as the range of action of the facilitation is orders of magnitude smaller than the competition [67, 79], we focus on the limit where the length of the facilitation is negligible  $L_f \approx 0$ . Then, the facilitation is described by the local function

$$M_f = \exp(\xi_f b).$$

We have considered this local facilitation in the analytical calculations and the numerical simulations in this chapter.

Nonetheless, the presence of facilitation is essential to generate bistability in the system. In fact, the presence of the stable bare solution and the homogeneous stable vegetation for the same set of parameters is impossible without facilitation. The existence of bistability has been studied in several works [11, 27, 66]. Indeed, the bare solutions  $b_0 = 0$  is stable (unstable) when  $\mu > 1$  ( $\mu < 1$ ) and the other solutions are given by

$$\mu = (1 - b_s) \exp(\Lambda b_s), \quad (3.3)$$

where  $\Lambda = \xi_f - \xi_c$ . When  $\Lambda > 1$  and  $1 < \mu < \exp(\Lambda - 1) / \Lambda$ , an unstable solution ( $b_-$ ) and a stable solution ( $b_+$ ) appear. The solution  $b_+$  also exists for  $\mu < 1$ , for any value of  $\Lambda$ .

## 3.2 Fairy circles in the nonlocal logistic-type model

As in the previous chapter, here we also focus on the region of bistability, where the bare state ( $b = 0$ ) and the homogeneous vegetated state are stable. We consider a set of parameters far from any spatial or temporal instability to avoid oscillations in time or space.

Another important ingredient in our approach to understand fairy circles is the nonlocal interaction. Several authors have developed their work on vegetation dynamics by considering a weak nonlocal coupling [11, 27, 62] such as a Gaussian or an exponential function, which decay asymptotically faster than a Lorentzian-type of kernel [110]. The weak nonlocal competition exhibits a spatial instability which generates patterns such as spots, gaps and stripes. In the absence of spatial oscillations, domains of bare state surrounded by uniform vegetation are unstable. These domains should diverge or shrink, according to the parameters of the system, for any small or large perturbation. To find the existence of stable localized structures like the ones described in Chapter 2, we should consider a strong nonlocal competition as the one defined in (3.2). This nonlocal competition can modify

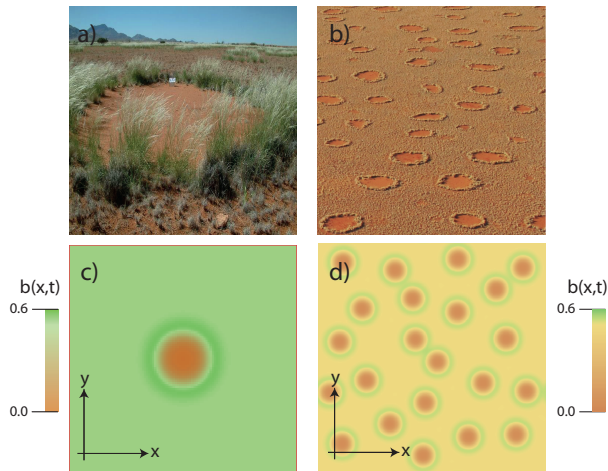


Figure 3.1: Figures a) and b) show typical fairy circles observed in the pro-Namibia zone of the west coast of southern Africa. Figures c) and d) are snapshots of biomass density obtained by numerical simulations of the model equation (3.1) on a system size of  $110 \times 90$  for c) and  $256 \times 256$  for d). The parameters in c) and d) are  $n = 4$ ,  $L_c = 1.5$ ,  $\xi_c = 1.2$ ,  $\xi_f = 3$  and  $\mu = 1.23$ . Inside the circles the density is zero and outside the circles corresponds to the uniform vegetated state. The photo in a) is courtesy of A. Scott, NamibRand Nature Reserve and the photo in b) is courtesy of N. Juergen.

the nature of the long-range interaction from attractive to repulsive. As a consequence, domains of bare state embedded by vegetation become stable. Figure 3.1c shows one stable fairy circle obtained by numerical simulations of Eq. (3.1). This localized structure has the same shape as the fairy circle in Namibia observed in Figure 3.1a. Several fairy circles interacting are performed by numerical simulations of Eq. (3.1). They are illustrated in Figure 3.1d, which fit with the observations of several fairy circles in Namibia as shown in Figure 3.1b. We observe that fairy circles in Namibia and in our numerical simulations from Eq. (3.1) have a fringe with high

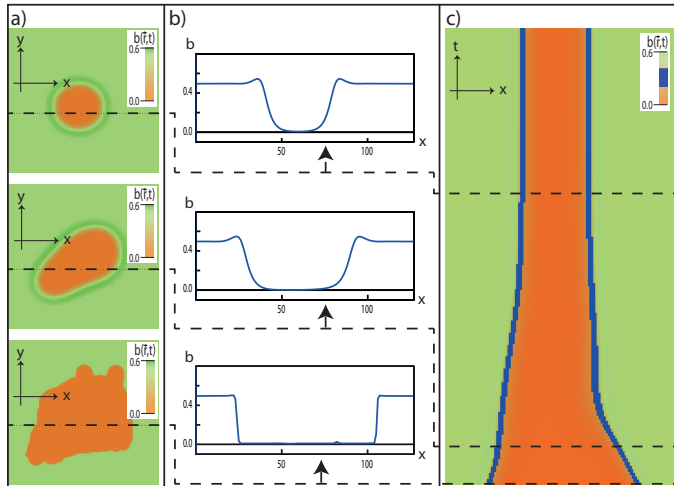


Figure 3.2: Numerical simulation of the dynamics in the model equation (3.1) with parameters  $n = 1$ ,  $L_c = 1.5$ ,  $\xi_c = 1.2$ ,  $\xi_f = 3$  and  $\mu = 1.231$ . Figure a) illustrates three different moments in the formation of a two dimensional fairy circle. Figure b) is the profile in the indicated cross-section of the structure. Figure c) shows the indicated cross section along the  $x$ -direction during time evolution.

biomass density along the border of the bare area in each circle.

The results observed in Figure 3.1 are when the system is in the equilibrium. Furthermore, Eq. (3.1) gives us some information about the dynamical behavior of fairy circles. For instance, Figure 3.2 shows how a non-homogeneous initial condition for  $b(x, y)$  can generate a fairy circle. Figure 3.2a shows (from the lower to the upper inset) the initial condition, a moment still under evolution, and the final equilibrium. We can observe how irregular initial condition evolves to a softer structure, and to a perfect circle with a fixed size at the end. Figure 3.2b shows the profiles along a specific cross-section in the structure, as indicated. Finally, Figure 3.2c is the spatio-temporal evolution of the profile described in Figure 3.2b. This

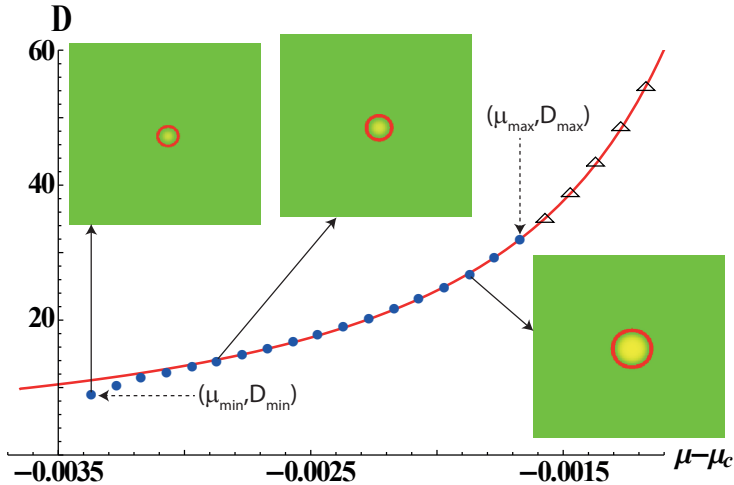


Figure 3.3: The diameter of the fairy circle as a function of the relative aridity with respect to the critical value  $\mu_c = 1.233$  obtained by numerical simulations of the model equation (3.1). Full dots indicate stable fairy circles, and triangles indicate unstable fairy circles. The parameters are  $n = 4$ ,  $L_c = 1.5$ ,  $\xi_c = 1.2$  and  $\xi_f = 3$ . The solid line fits with the function  $(a/(\mu_c - \mu)^\alpha)$ , with  $a = 0.002$  and  $\alpha = 1.51$ . The insets are the fairy circles for the indicated dots.

spatio-temporal diagram confirms us the stability of fairy circles.

In Namibia, fairy circles have some features as illustrated in Figure 3.1 a) and b). For instance, fairy circles have a circular flat area devoid of any vegetation. Also, a fringe with higher biomass density is exhibited along the border of the bare area [65,67]. These features are complemented by a longtime stability observed by different authors [65,72]. As we mentioned before, all these features match with our numerical simulations obtained from Eq. (3.1), which are showed in Figure 3.1 c) and d).

Another important characteristic observed among fairy circles is related to their size. Several field observations suggest that the diameter of fairy circles

increases with the aridity [65,67,74]. Figure 3.3 illustrates the size of fairy circles, obtained from numerical simulations of Eq. (3.1), as a function of the aridity  $\mu$ . We observe that the diameter of numerical fairy circles increases with the aridity. When the value of the aridity decreases enough, the fairy circles shrink and disappear by a saddle-node at  $\mu_{min}$ . When the aridity increases, there is a value  $\mu_{max}$  where the fairy circles exhibit a radial instability and become stripes. Note that, if the initial condition is quite circular, the above mentioned instability is slow with respect to the time evolution of the size (However, after a long term, the final result with  $\mu > \mu_{max}$  is a stripe). The value  $\mu_c$  represents the Maxwell point, where a flat front that connects both states (obtained numerically) is motionless.

The aforementioned features are qualitative. Moreover, the reported ratio between the maximum and the minimum diameter of fairy circles in Namibia is around 5 [65,72] or at least 2.5 [67]. Our numerical results get a ratio  $D_{max}/D_{min} \approx 4$ , which agree with field observations. In addition, the reported values of the roots length range from  $0.3m$  [68] to  $0.9m$  [67], and the maximum average diameter is  $8m \sim 10m$  [65,67]. Using this, we estimate that the ratio between the maximum diameter and the roots length is  $10 \sim 30$ . The numerical result obtained for this ratio (shown in Figure 3.3) is around 20, in concordance with field observations.

### 3.3 Analytical description in the nonlocal logistic-type model

In order to obtain an analytical description of fairy circles, we restrict our analysis to a one dimensional system with a small intensity in the nonlocal competition  $\xi_c$ . However, the general analytical description of these structures is still complicated. To solve that problem, we work near the point where the bistability arise. From Eqs. (3.3), we know that this critical point is given by  $\mu_c = 1$ ,  $\Lambda_c = 1$  and  $b_c = 0$ . We introduce the small parameter  $\gamma \ll 1$  as  $\Lambda = \Lambda_c + \gamma$ . The aridity is given by  $\mu = \mu_c + \mu_2\gamma^2 + \dots$ . The

intensity of the nonlocal competition  $\xi_c = \epsilon_1 \gamma$  is small. Finally, we express the biomass density as  $b = b_c + b_1 \gamma + b_2 \gamma^2 + \dots$ . Then, expanding at the third order of  $\gamma$ , the solvability condition gives

$$\begin{aligned} \partial_t b_1 = & \left( b_1 - \frac{b_1^2}{2} - \mu_2 \right) b_1 + \partial_{xx} b_1 \\ & + \epsilon_1 b_1 \left( b_1 - \int \frac{N_n b_1(x + x', t) dx'}{1 + x'^n / L_c^n} \right). \end{aligned} \quad (3.4)$$

This equation has the same form as the Eq. (2.3) studied in Chapter 2.

In absence of competition ( $\epsilon_1 = 0$ ) and with  $\mu_2 = 4/9$ , Eq. (3.4) has a motionless front solution given by

$$b_{\pm}(x - x_0) = \frac{2}{3} \left( 1 \pm \tanh \left( \frac{x - x_0}{12} \right) \right),$$

where  $x_0$  is the core of the front.

Considering  $\mu_M - \mu_2 = \eta \ll 1$  the distance to the Maxwell point  $\mu_M$ , we can develop the same analysis as in the Section 2.5 to study the interaction between two fronts. For  $n = 2$  we add a small correction to the superposition of the fronts  $b_+(x - \Delta/2)$  and  $b_-(x + \Delta/2)$ . Then, applying the solvability condition, we get the dynamical equation for the size  $\Delta$  of the structure

$$\partial_t \Delta = \frac{48 L_c \epsilon_1}{\pi \Delta} - 36 \eta. \quad (3.5)$$

Then, the width of equilibrium is given by

$$\Delta = \frac{4 L_c \epsilon_1}{3 \eta \pi}. \quad (3.6)$$

This result predicts that the size of the structure grows with the aridity. Equation (3.6) also illustrates how the range and the intensity of the strong nonlocal interaction result in an increase in the size of fairy circles.

It is possible to obtain a more general result for any value of  $n$ . In this case, the solution of the equilibrium width resulting from the front interaction is

$$\Delta = 2L_c \left( \frac{2\epsilon_1 (n/2 - 1)!^2}{3\pi (\mu_M - \mu_2) (n - 1)!} \right)^{1/(n-1)}.$$

This expression, valid strictly in one dimension, shows that the width of the fairy circle increases with the aridity parameter, similar to those observed in two dimensions as shown in Figure 3.3. To have a positive real distance  $\Delta$ ,  $\mu_2$  must be smaller than  $\mu_M$ . The value of  $\Delta$  grows as  $\mu_2$  goes to  $\mu_M$  and diverges at the Maxwell point. Intuitively, the region without vegetation grows with the aridity because there are less resources for plants. The analytical understanding of the two dimensional problem, which involves curvature effects, is a work in progress. However, the change of the fairy circles diameter as a function of the aridity (in two-dimensional numerical simulations) agrees with the results obtained from the analytical calculations in one dimension.

### 3.4 Numerical simulations of fairy circles in the strong nonlocal reaction-diffusion type of model

In this section, we consider a reaction-diffusion type of model in order to show the robustness of the proposed mechanism in vegetation dynamics. This type of model has been used to explain the formation of stripes located on the slope of hills [12, 34, 47]. Labyrinth patterns, spots and gaps have also been studied using this type of equation [15, 19]. Moreover, the formation of rings [60, 62] and some studies on ecological diversity [130] have considered similar modeling. In general, these models consider a dynamical equation to describe the biomass density and another one to describe the water dynamics in the soil [15, 74, 76]. Nonetheless, the dynamics of the water in the surface of the ground is also modeled in some works [19, 71].

Several reaction-diffusion type of model consider a local interaction. However, the increment of the water uptake through the lateral expansion of the roots is modeled by a nonlocal interaction [19,60]. A weak nonlocal kernel, Gaussian or exponential, is usually considered. We modify the weak nonlocal interaction, incorporating a Lorentzian-type of kernel, to replicate the localized structures obtained before. Then, based on the model in [19,62], our reaction-diffusion model is

$$\begin{aligned}\partial_t b &= G_b b(1-b) - \mu b + \delta_b \nabla^2 b \\ \partial_t w &= p - (1-\rho b)w - \beta G_w w + \delta_w \nabla^2 w.\end{aligned}\tag{3.7}$$

All the parameters are normalized. We can consider  $b$  as the normalized biomass density per unit area,  $w$  is the normalized water present in the soil,  $\mu$  represents the mortality,  $p$  is the normalized rainfall,  $\rho$  accounts for the evaporation reduction due to shading,  $\beta$  is the normalized consumption rate per unit of biomass of water in the soil,  $\delta_b$  is the normalized biomass diffusion rate that describes the lateral growth of the plants and the seed dispersion,  $\delta_w$  corresponds to the normalized water diffusion,  $G_b$  stands for the increase in the growth of the biomass due to the water consumption through the roots, and  $\beta G_w$  is its corresponding consumption of water. Note that  $G_b$  and  $G_w$  are nonlocal functions, and are defined by

$$G_b = \int g(\mathbf{r}, \mathbf{r}', b) w(\mathbf{r}', t) d\mathbf{r}'$$

and

$$G_w = \int g(\mathbf{r}', \mathbf{r}, b) b(\mathbf{r}', t) d\mathbf{r}'.$$

In order to simplify our work, we consider

$$g(\mathbf{r}, \mathbf{r}', b) = \frac{N_n (1 + \eta b(\mathbf{r}, t))^2}{1 + (|\mathbf{r} - \mathbf{r}'|/\sigma_0)^n},\tag{3.8}$$

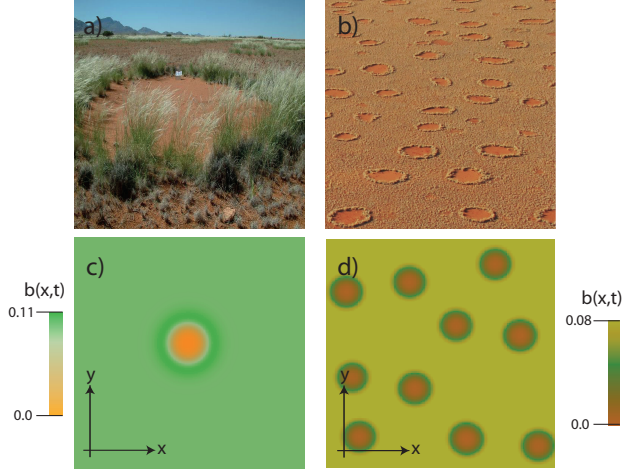


Figure 3.4: Figures a) and b) show typical fairy circles observed in the pro-Namibia zone of the west coast of southern Africa. Figures c) and d) are snapshots of biomass density obtained by numerical simulations of the model equation (3.7) on a system size of  $110 \times 90$  for c) and  $256 \times 256$  for d). The parameters in c) and d) are  $\mu = 0.4143$ ,  $\delta_b = \delta_w = 1$ ,  $\rho = 6$ ,  $\beta = 5$ ,  $p = 0.29$ ,  $\alpha = 10$ ,  $q = 0.05$ ,  $f = 0.1$ ,  $\sigma_0 = 1$ , and  $n = 3$ . Inside the circles the density is zero and outside the circles corresponds to the uniform vegetated state. The photo in a) is courtesy of A. Scott, NamibRand Nature Reserve and the photo in b) is courtesy of N. Juergen.

where  $N_n$  is the normalization constant,  $\sigma_0$  is the characteristic length of competition,  $n$  describes how the nonlocal interaction decays with the distance and the term  $(1 + \eta b(\mathbf{r}, t))^2$  describes the root-augmentation feedback [19, 40, 131]. The full model should consider the term proportional to  $\eta$  as an allometric factor. However, the form of Eq. (3.8) is a simplification in order to develop fast numerical simulations.

As in the model (2.3), Eq. (3.7) exhibits bistability. The model (3.7) is more complex and its bistability between two homogeneous states emerges

for a certain range of parameters as in Eq. (3.1). For this range of parameters, and by including a strong nonlocal coupling, we performed numerical simulations of Eq. (3.7) to show the formation of fairy circles in reaction-diffusion type of models in vegetation. These numerical simulations of a single fairy circle and for a group of them are illustrated in Figure 3.4 c) and d), respectively. Figure 3.4 a) and b) are photos of fairy circles in Namibia that correspond to the numerical structures illustrated in b) and c). These structures are stable through the nonlocal interaction and the bistability of the system. In a qualitative way, these structures have the same behavior and features as in the structures obtained from Eq. (3.1). Nevertheless, a deep study of these systems is required in order to get a better understanding of the strong nonlocal competition effect in a reaction-diffusion type of model.

## Chapter 4

# Spots in a semiarid region in the highlands

Besides systems which are spectacular due to the size of their structure which may exceed 20 meters [1,11,65], there is however another very broad and ubiquitous class of vegetation patterns for which an interpretation as localized structures appear relevant [58,62]. These structures appear at small spatial scales (from ten centimeters to few meters), and they are related to a very pervasive feature of plant development, namely clonal reproduction. Many plants or plant structures are made of elementary components referred to as ramets, which clone themselves to duplicate and grow in order to form larger entities of vegetation, i.e. patches, which are also called spots. Ramets are basic plant architectural units, built upon one main axis (stem) and features leaves, roots and buds. The main ramet axis may ramify or extend (organogenesis versus extension) as in any plant development scheme, but the most peculiar property of clonal plants, which is a part of the broader category of reiteration processes [132], is that ramets replicate themselves several times to extend the size of the patch (spot). The spots may not only extend in area but also undergo a change of their over-

all shape. In two-dimensional space, this may lead either to the splitting of the spot (for instance, due to die-back of the central part) [133], or to the possible merging of different spots [134]. The former leads to vegetation patches apparently distinct yet genetically homogeneous, whereas the latter outcome may result in vegetation patches of heterogeneous genetic identity [134]. Both cases result in blurring by clonal reproduction of the notion of individual plant.

Clonal reproduction is particularly notable among plant forms of small size such as grasses, herbs and shrubs. It also appears of increasing importance in ecosystems that are resource deprived and/or that experience strong climatic constraints (e.g. clonal propagation of “*Olea europaea* subsp. *laperirei*” in the climatic conditions in the Saharan mountains [135]) or grazing [136]. A pioneering work aimed at investigating clonal plant as self-organized localized structures was carried out in reference to a desert grass in the Negev desert [58,60]. In this chapter, we shall consider another constraining environmental context, which corresponds to high altitude tropical dry-lands with a special reference to the Andes. There, plants are constrained by cold temperature and low rainfall to evapotranspiration ratio, while often experiencing grazing pressure from camelids (llamas, alpacas). In this environment, spot-forming grasses are important constituents of the vegetation cover [137]. Vegetation patches appear to be made of several tiny ramets that are called tillers. The plants belong to the species “*Festuca orthophylla* (Poaceae)”. This species can locally dominate the vegetation within the study area by forming largely mono-dominant patches contrasting with bare soils (Figure 4.1).

Here we aim to model and interpret clonal morphologies in the Andes as localized structures by considering the generic interaction-redistribution model [11,27,66]. We explore how the model may account for localized structures occurring as spots, to create isolated clonal vegetation patches within a bare soil matrix. We will show that by considering the available data on ramet morphology and biomass dynamics of the reference ecosystem, the model is able to predict macroscopic features in the observed patterns such

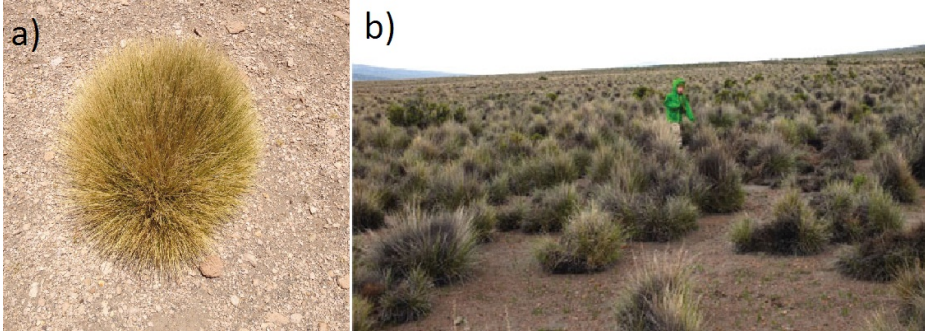


Figure 4.1: *Festuca orthophylla* also known as *paja brava*. Figure a) shows an isolated spot near San Pedro de Atacama, Chile. Figure b) show several spots in the Sajama National Park, Bolivia. Figure b credit: F. Anthelme.

as the spot size and inter-spot distance. A thorough interpretation is carried out based on the available information to provide realistic values for the model parameters. On this basis, we intend to show that using this array of parameter values relating to processes at ramet scale, the model is able to provide predictions at the scale for which plant biomass displays the maximum level of spatial variation (as illustrated in Figure 4.1).

## 4.1 The logistic-type model

As aforementioned, there are several models to describe the self-organization in vegetation dynamics. In this chapter, we consider the logistic-type model that we took into account in Chapter 3. However, in this chapter our approach is based on a different kind of nonlocal interaction. This model is defined by

$$\partial_t b = b(1-b)M_f - \mu b M_c + D\nabla^2 b, \quad (4.1)$$

where  $b(x, t)$  represents the normalized biomass density per unit area. The first term on the right-hand side expresses the logistic growth and saturation

of the biomass, and  $M_f$  describes how the facilitation increases this growth rate. In the second term, the aridity  $\mu$  is the parameter that controls the mortality rate related to the absence of water and other factors such as herbivores or any other adversity component, and  $M_c$  accounts for how the competition among plants increases the rate of mortality. The last term corresponds to the diffusion given by the seed dispersal and the lateral growth of the plants  $D\nabla^2$ . When  $M_f$  and  $M_c$  are constants, Eq. (4.1) corresponds to the standard logistic model. However, we consider  $M_f$  and  $M_c$  as functions of  $b$ .

In this chapter we use a Gaussian-type of kernel for facilitation  $M_f$  and competition  $M_c$

$$M_{f,c} = \exp\left(\xi_{f,c} \int K_{f,c}(|\mathbf{r} - \mathbf{r}'|) b(\mathbf{r}', t) d\mathbf{r}'\right), \quad (4.2)$$

where

$$K_{f,c}(|\mathbf{r} + \mathbf{r}'|) = N_{f,c} \exp\left(-\frac{|\mathbf{r} - \mathbf{r}'|^2}{L_{f,c}^2}\right)$$

and

$$N_{f,c} = \left(\int \exp\left(-\frac{|\mathbf{r}'|^2}{L_{f,c}^2}\right) d\mathbf{r}'\right)^{-1}.$$

For studying the homogeneous states of Eq. (4.1), we reduce the model to

$$\partial_t b = b(1 - b) \exp(\xi_f b) - \mu b \exp(\xi_c b). \quad (4.3)$$

The solution of this equation  $b_0 = 0$  represents a territory devoid of vegetation. The zero solution is stable (unstable) for  $\mu > 1$  ( $\mu < 1$ ). Besides there are other two positive solutions  $b_{s\pm}$ , which exist for  $\Lambda = \xi_f - \xi_c > 1$  and  $1 < \mu < \exp(\Lambda - 1) / \Lambda$ . The solution  $b_{s+}$  also exists for any value of  $\Lambda$  and  $\mu < 1$ . These solutions are described by the equation

$$\mu = (1 - b_s) \exp(\Lambda b_s). \quad (4.4)$$

The solution  $b_{s-}$  is unstable. Nevertheless, without space the solution  $b_{s+}$  is stable. Figure 4.2 illustrates the homogeneous steady states and their stability without space.

## 4.2 Spatial instability of the homogeneous state

In this section we study the spatial instability of the solution  $b_{s+}$ . In contrast with Section 2.3, here we develop the standard method to find the region where the homogeneous steady state  $b_{s+}$  becomes unstable. Indeed, we consider perturbations of the form

$$b(\mathbf{r}, t) = b_{s+} + \delta \exp(\lambda t + i\mathbf{k}\mathbf{r}) + c.c., \quad (4.5)$$

where  $\delta$  is the amplitude of the perturbation with a wave vector  $\mathbf{k}$  and its associated eigenvalue  $\lambda$ .

Introducing (4.5) in Eq. (4.1) we obtain, at the first order in  $\delta$  and neglecting the contribution of  $D \ll 1$ , the value for the eigenvalue  $\lambda$  as a function of  $k = |\mathbf{k}|$

$$\begin{aligned} \lambda = & \exp(\xi_f b_{s+}) \left( (1 - 2b_{s+}) + b_{s+} (1 - b_{s+}) \xi_f \exp(-k^2 L_f^2/4) \right) \\ & - \mu \exp(\xi_c b_{s+}) \left( 1 + b_{s+} \xi_c \exp(-k^2 L_c^2/4) \right). \end{aligned} \quad (4.6)$$

The  $k_c$  that maximizes the value of  $\lambda$  is given by

$$\frac{\partial \lambda}{\partial k} = 0.$$

We have

$$\begin{aligned} 0 = & -\frac{k L_f^2}{2} (1 - b_{s+}) \exp(\xi_f b_{s+}) \xi_f \exp(-k^2 L_f^2/4) \\ & + \mu \frac{k L_c^2}{2} \exp(\xi_c b_{s+}) \xi_c \exp(-k^2 L_c^2/4). \end{aligned}$$

Considering the relation between  $\mu$  and  $b_{s+}$  given by Eq. (4.4), we get the value of a  $k$  different from zero

$$k_c^2 = \frac{4 \log(L_c^2 \xi_c / L_f^2 \xi_f)}{L_c^2 - L_f^2} \quad (4.7)$$

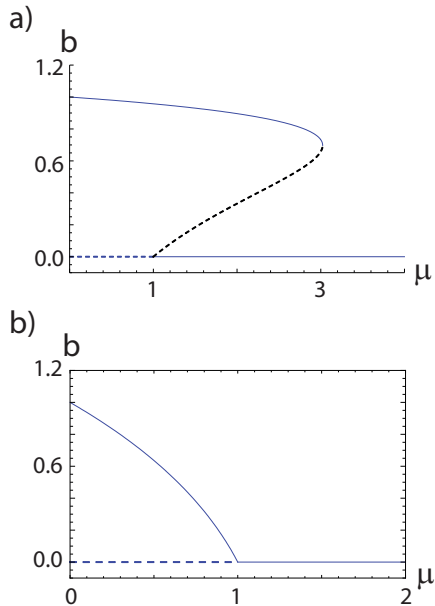


Figure 4.2: Homogeneous steady states of Eq. (4.3). The upper solid branch represents the solutions  $b_{s+}$ . The dashed line between  $b_0 = 0$  and  $b_{s+}$  corresponds to  $b_{s-}$ . Solid lines illustrate stable states, whilst dashed lines illustrates the unstable states. Figure a) corresponds to  $\Lambda = 3.3$  and Figure b) corresponds to  $\Lambda = 0.5$ .

and the unstable wavelength

$$\lambda_c = \pi \sqrt{\frac{L_c^2 - L_f^2}{\log(L_c^2 \xi_c / L_f^2 \xi_f)}}. \quad (4.8)$$

Now we compute the threshold where  $\lambda$  in Eq. (4.6) becomes zero, and consequently the solution  $b_{s+}$  loses its stability. This threshold is defined by

$$1 = (1 - b_c) \left( \xi_f \exp\left(-k_c^2 L_f^2 / 4\right) - \xi_c \exp\left(-k_c^2 L_c^2 / 4\right) \right). \quad (4.9)$$

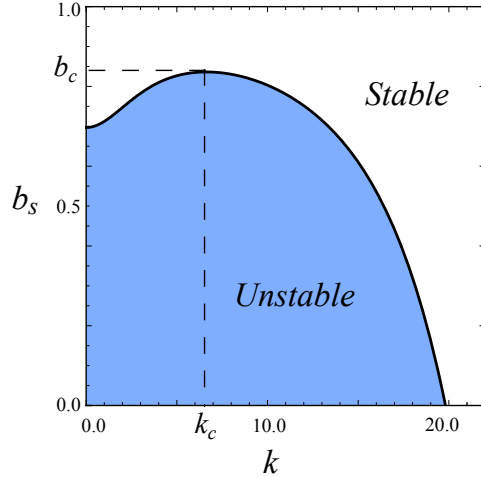


Figure 4.3: Marginal stability curve for  $b_{s+}$  given by Eq. (4.9). The parameters used are  $\xi_c = 5.9$ ,  $\xi_f = 9.1$ ,  $L_c = 0.4$  and  $L_f = 0.15$ . The stability versus instability domains are separated by a solid line. The values  $b_c$  and  $k_c$  correspond to the threshold at which the spatial instability appears.

The domain of instability includes the wavenumber of the fastest growing modulation. The critical wavenumber corresponds to the situation where the homogeneous steady state  $b_+$  exhibits a pattern forming instability. Figure 4.3 shows the threshold given by Eq. (4.9). This figure illustrates the maximum  $b_c$ , which becomes unstable and corresponds to the critical wavenumber  $k_c$ .

### 4.3 Measurement of the parameters

Large areas experiencing tropical alpine environments are encountered in Africa and South/Central America, Southeast Asia and various islands, while 90% of these environments are observed in the Andes [138]. These

areas experience cold minimum temperatures that constrain plant development [139], along with some distinctive features: (i) an inversion of rainfall gradients in the form of increasing aridity at higher elevation, (ii) strong variations in temperatures, and (iii) the absence of persisting snow cover contrary to most alpine environments [139, 140]. In this study, we specifically refer to the Sajama National Park in Bolivia for which climatic features, as described in [141], fit the overall descriptions of tropical alpine environment. Notably, the annual precipitation is around 350mm and is concentrated between November and March. Locations in the Sajama National Park, where direct observations have been carried out by one collaborator (F. Anthelme), experience the same climate. The estimation of the parameters was developed by F. Anthelme and P. Coueron.

The singular characteristics of tropical alpine environment make some plant life forms specific to these regions, or at least permit them to be found there at higher abundance. Spots of grasses are frequently observed and often are a dominant life form in tropical alpine environment [142]. There, spots of grasses display a typical two phase structure having a limited lateral growth and a high density of tall stems at spot center (Figure 4.1). The humidity in spots is higher than in the bare soil as a result of the facilitation by shading. Nonetheless, spots in dry environments also have a negative impact on other plants, because of strong competitive traits [143].

## **Interpretation of the spot pattern in the Sajama National Park**

Here,  $b$  is the above-ground biomass density irrespective of the below-ground part. The density is defined with respect to the observed maximal local biomass, which is found in the middle of a vegetation patch. In the case of “*F. orthophylla*”, we assume accordingly that a density of 1 is reached in the center of every mature, non-senescent spot, while the density decreases towards the periphery as described in [144]. For simplicity, the model does not distinguish the live and dead fractions of the biomass as in [144]. The

average biomass density over a spot is estimated at around 0.5. The overall basal area of the spots is reported to be around 15-20%, a range of values which appears stable across space from both literature [144] and direct measurements carried out by F. Anthelme in the Sajama National Park. We therefore assess the overall biomass density of this typical pattern as  $\tilde{b} \approx 0.1$ .

Associated parameters to the nonlocal interaction are, firstly, the ranges of interactions ( $L_f$  and  $L_c$ , i.e. the ranges of the Gaussian kernels) which reflect ramet morphology and, secondly, the intensity of the interaction (expressed by  $\xi_f$  and  $\xi_c$ ). The overall biomass dynamics is ruled by the aridity  $\mu$ .

## Morphological parameters

Based on the available published data and direct field observations (Figure 4.4), we set  $L_c$  to be the observed length of lateral roots (i.e. 40 cm). We assess the range of the facilitation effect resulting from lateral shading (integrating the effect of dusk and dawn sun inclinations) and protection from grazing as half the height of an average mature ramet. In the case of the “*F. orthophylla*” grass, the average height of live tiller leaves is about 20–30 cm, and in accordance with the modelling of interactions through Gaussian kernels, we set  $L_f$  to 10–15 cm.

## Facilitative and competitive feedbacks from the above-ground biomass

The intensity of facilitation and competition (parameters  $\xi_f$  and  $\xi_c$ ) is first assessed with respect to the influence of vegetation on soil moisture (considered via the volumetric soil moisture content, vol%) within the shallow rooting zone. In the topsoil that is actually explored by spot roots (<40–50 cm), soil moisture proved to be virtually undetectable during the dry season



Figure 4.4: Lateral extent of the superficial rooting system at the periphery of a small tussock of “*Festuca orthophylla*”. Photo credit: F. Anthelme.

irrespective of the location [144]. But during the rainy season, strong variations were observed in time (depending on the occurrence of rain showers) as well as in space (under vegetation cover versus in open ground). Maximal values of soil volumetric moisture were reported to be above 5.5% under a grass spot while they do not exceeded 1.5% in the absence of vegetation. Moreover, a mulching experiment allowed soil moisture content to reach as much as 19.4% [144], emphasizing the pervasive role of evaporation in depleting the scarce topsoil water resource. Besides it has been reported that the spot aerial part was at least as efficient as the mulch in decreasing the hottest mid-day soil surface temperature and henceforth the evaporative demand. Hence reinterpreting the published results allowed us to separate the relative effects of water in the soil consumption by grass tillers (competition) from the protection against evaporation (facilitation). It thereby appears that the reduction of evaporation by grass cover represents a possible increase in maximal volumetric soil moisture content up to 12 times the maximal content found in bare areas. Conversely, the potential water demand from well-developed tillers represents around 9 times the bare soil content. The overall balance appears thus positive thereby illustrating the predominance of facilitation over competition that helps tillers survive

adverse climatic conditions as soon as they are part of a spot.

From those observations, we may infer that at the center of a modal tussock the soil moisture was around 2.5 times the level it reached under bare ground, far away from any vegetation influence. Reasoning on moisture values averaged over a rainy season instead of maximal values yields a lower, yet a positive value of around 1.5 under vegetation. It is reasonable to think that maximal values render better the functioning of the system, which is probably based on pulses of vegetation development triggered by discrete rainfall events. For instance, Barbier et al. [129] described the functioning of a semiarid system. They conclude that the higher difference, in terms of water budget between vegetated and bare locations, was mostly noted during the days following a rain shower before progressively fading away as the topsoil water dries up everywhere.

To transfer the above values into the parameters of the model (i.e.  $\xi_f$  and  $\xi_c$ ), we refer to the effect of unusually low rainfall, as reported by Monteiro et al. [144], who compared biomass production between 2007–2008 (considered as a normal rainy season, 384mm) and 2006–2007 (poor season, 327mm, minus 15%). As a response of “*F. orthophylla*” to the decrease in rainfall, the mean standing spot biomass dwindled by 40% (table 5 in [144]). But such a strong decrease was not a direct result of tiller death but rather reflected a reduction of the green fraction in the well-developed tillers [144], and caution is needed while interpreting it. On the other hand, studies of water-limited ecosystems with annual rainfall around 350mm per year have reported that grass biomass reduction accompanying a 15% rainfall decrease is about 30% [145]. From this observation and assuming a linear response of biomass production to any water resource fluctuations of reasonable amplitude, we set a ratio of 2 (0.3/0.15) and apply it to variation in soil moisture determined by a tiller bunch of modal size, as described above. According to the model, this variation is equal to  $\exp(\xi_f b^t)$  for moisture increase and to  $\exp(\xi_c b^t)$  for moisture decrease, where  $b^t$  is the average biomass density of tillers over a spot, which is around 0.5. Thus, we obtain the parameters  $\xi_f = 6.3$ ,  $\xi_c = 5.8$ , and consequently  $\Lambda \approx 0.5$ . This result gives a vegetation

system weakly cooperative considering the only aspect of vegetation feedback on biomass production is through soil water resource. This weakening of the positive balance is due to the strong demand of the grassy cover for transpiration. However, plant biomass also exerts another kind of positive feedback since it acts as a protection against grazing. This second source of facilitation can be considered as additive to soil moisture variations since it is independent of the soil water resource. We will assess it in the subsequent discussion as part of the overall biomass dynamics.

## Overall biomass dynamics

The aridity  $\mu$  is the ratio of the plant biomass lost at low biomass levels (i.e. far under the logistic saturation). In this ecosystem, biomass loss features two components, which are senescence of live plant material as well as live biomass destruction by grazing. These two causes determine additive fractions of  $\mu$ , i.e.  $\mu = \mu_o + \mu_g$  relating to senescence and grazing, respectively.

The aridity fundamentally expresses the potential development of a small amount of live plant biomass (typically a small bunch of young ramets), which does not benefit from developed plants. The young plant will either die out if the conditions are also unfavorable ( $\mu > 1$ ) or develop at a rate, which is a decreasing function of  $\mu$ . Qualitatively, we expect  $\mu$  to be a decreasing function of rainfall. From experimental results [144] and direct field observations, it appears that without any facilitative effects by large pre-existing biomass, tiller development is very weak and may not completely balance decay. So  $\mu_0$  should be substantially larger than 1.

In the case of "F. orthophylla", we shall rely on an experiment reported in [146] that provides elements to assess the grazing-related part of  $\mu$ : after experimental burning (i.e. removal of most of the above-ground biomass), the biomass regrowth is dependent on the root system which has been spared by fire. In fenced plots that were not accessible to camelids, the

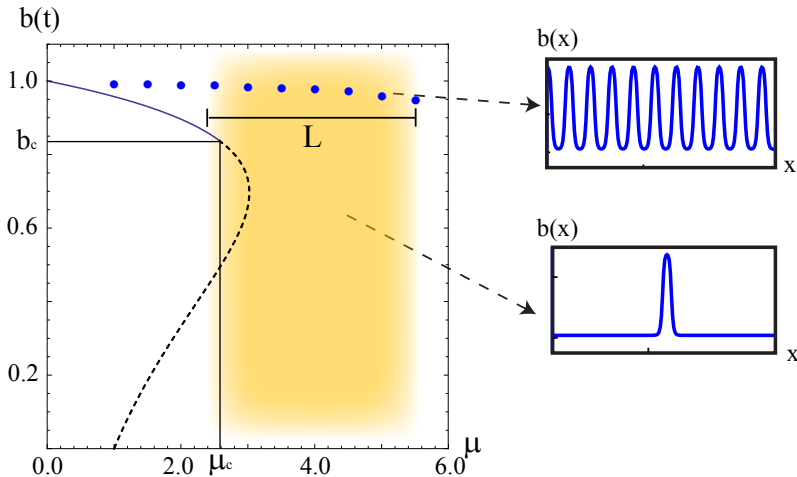


Figure 4.5: One-dimensional bifurcation diagram and localized structures from Eq. (4.1). The solid and dashed lines correspond to stable and unstable homogeneous steady states ( $b_{s+}$  and  $b_{s-}$ ), respectively, obtained analytically from Eq. (4.4) and (4.9). The dots are the maximal biomass density values obtained at the center of the periodic structures for the one-dimensional simulations of the patterns. The pattern is illustrated in the upper inset. The domain where localized solutions exist is denoted by  $L$ . A localized spot is illustrated in the bottom inset. The parameters are  $\xi_c = 5.9$ ,  $\xi_f = 9.1$ ,  $L_c = 0.4$ ,  $L_f = 0.15$  and  $D = 0.01$ . The insets consider  $\mu = 4.5$ .

total biomass production during the first year of regrowth was seven times higher than in unfenced plots subjected to grazing. Assuming an exponential regrowth curve at plot scale, since the system restarts from virtually no above-ground biomass, it yields:  $\mu_g = \log(b_f/b_u)/t_f$ , where  $b_f/b_u$  is the ratio (at the end of the first year after burning of biomass) between fenced and unfenced spots, and  $t_f$  is 1 year or around 2 tiller generations [144]. Accordingly, we assess  $\mu_g = \log(7)/2 = 1$ .

Another aspect of the same experimental design also showed that, around

the biomass levels of the patterns observed in the studied area ( $\tilde{b}$ ), fencing out camelids determined a small increase in biomass production ( $\sim 10\%$ ). This indicates that shielding a large share of young and productive tillers against grazing is an important component of the positive feedback that a grass stand exerts on its own dynamics. To assess the magnitude of such a protecting effect and deduce the final value of  $\xi_f$ , we relate the slight increase in the biomass production  $\Delta_s$  between fenced and unfenced situations to  $\mu_g$  and  $\xi_f^0 = 6.3$ , which corresponds to the value assessed at the previous point and refers to the aspect of vegetation feedback on soil moisture. Thus, we obtain  $\xi_f = 9.1$  and  $\Lambda = 3.3$ .

Our last step is to assess  $\mu_0$  via  $\mu$ . For this, we assume that the observable small-sized spots (as in Figure 4.4) represent the minimal concentration of biomass which allows the survival of a spot in spite of environmental adversity. We then relate their biomass density (over an individual small spot) to  $\mu$  by assuming that equation (4.1) applies at individual spot scale while it was previously applied to describe the homogeneous biomass density over the whole pattern. Thus, with  $\Lambda \approx 3.3$  as previously assessed, we obtain that the values of  $\mu$  are of the order of 3.0, which implies  $\mu_0$  of the order of 2.0.

## 4.4 Localized spots of vegetation

There are some works that explain the formation of localized spots in different regions that come from a spatial instability [38, 56]. However, these works take into account simplified models with local interaction. In this chapter we focus on model (4.1), which considers nonlocal interaction through the integral terms of competition and facilitation described in (4.2).

Figure 4.5 shows a bifurcation diagram in the plane  $\mu - b$  that considers the spatial instability described in Section 4.2. The solid (dashed) line corresponds to stable (unstable) homogeneous steady states. We observe

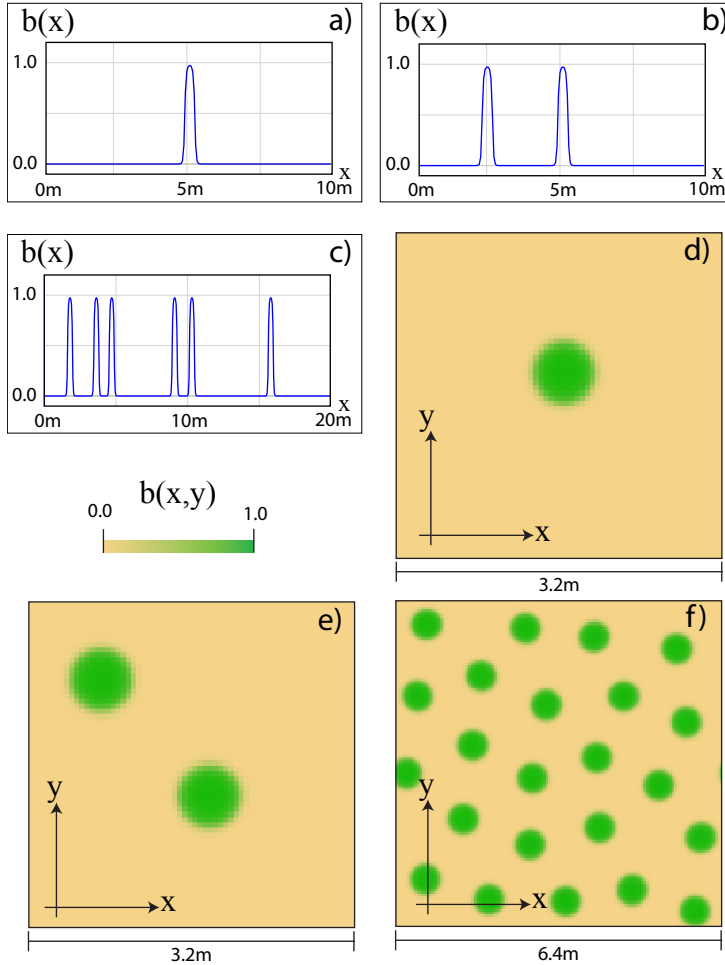


Figure 4.6: Localized vegetation spots in one and two dimensions. The Figure shows the variation of the number of localized structures according to the initial conditions used for simulations, in one dimension (a-c) and in two dimensions (d-f). All panels display the variation of biomass density in one or two dimensions. The results were obtained by numerical simulations of Eq. (4.1). The parameter values are  $\xi_c = 5.9$ ,  $\xi_f = 9.1$ ,  $L_c = 0.4$ ,  $L_f = 0.15$ ,  $D = 0.01$  and  $\mu = 4.5$ .

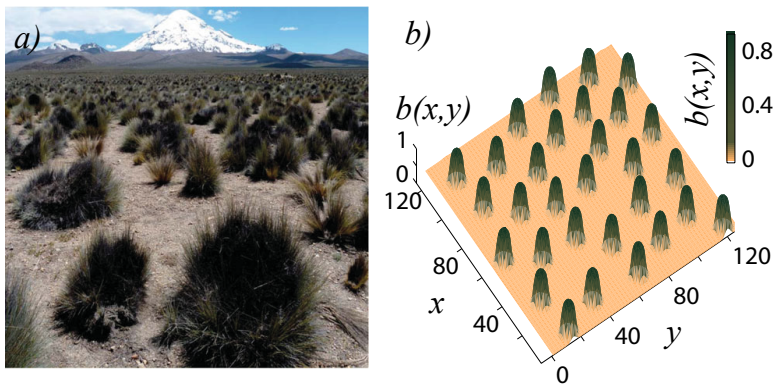


Figure 4.7: Overall comparison of a system of spots of *Festuca orthophylla* (observed in the Sajama National Park, Bolivia) in Figure a) with numerical simulations of Eq. (4.1) displayed in Figure b). The simulated system displays a mean distance between spots centers that agrees with the range of values observed in the field (i.e. 0.8–1 m). Figure a) credit: F. Anthelme.

the point  $\mu_c$  where the homogeneous state  $b_{s+}$  becomes unstable from Eq. (4.9) and (4.4). The dots show numerically the region where the pattern exists (an example is illustrated in the upper inset of Figure 4.5). Note that the region that exhibits the pattern is much bigger than the one where the solution  $b_{s+}$  is unstable. Also the region  $L$ , which presents localized spots as the one illustrated in the bottom inset of Figure 4.5, persists beyond the homogeneous solution. The number of peaks in the localized spots, as the ones illustrated in Figure 4.6 for one and two dimensional systems, are determined by the initial conditions used. The condition under which localized structures and periodic patterns appear are closely related. When the Turing instability becomes subcritical, there exists a pinning domain where localized structures are stable. These results are relevant to show that spots of vegetation are stable on a large domain and they are able to survive through important variations in the environmental conditions

such as differences in annual rainfall or changes in the number of herbivores present in the area.

We use the parameters estimated above to compute the wavelength expected for the pattern corresponding to the first non-zero Fourier mode to become unstable. It yields 0.95 m, i.e. within the range of distances between spots centers measured in the field (0.8–1 m). The wavenumber  $\lambda_c$  strongly depends on the values taken for the ranges of facilitative and competitive interactions between ramets. Simulations for  $L_f = 0.1$  meters and  $L_c = 0.4$  meters also reached a wavelength around 1m and closely mimicked the observed patterns as illustrated in Figure 4.7.

## Chapter 5

# Spiral vegetation patterns

Beyond the context of vegetation patterns, spiral waves that rotate around their cores with uniform frequency have also been explained as a result of self-organized behavior. They were first observed in the context of the Belousov-Zhabotinsky reaction [147, 148]. Their formation is related to the presence of excitability in the system [149, 150]: a strong response to a weak stimulus that can propagate across the media. In fact, spirals have been observed in other chemical contexts, such as Carbon-monoxide oxidation on Platinum surfaces [151], or in chemical gardens [152]. Furthermore, spiral patterns are present in many biological contexts, for instance calcium waves in slime mould aggregates [153], heart tissue [154], neural excitable waves in the neocortex [155], and the growth surface of nacre [156].

The aim of this chapter is to discuss the possibility of excitable behavior on pasturelands, and the appearance of spiral patterns as a consequence of this excitability. We first document spiral shaped patterns of grass, observed in high-altitude wetlands in the north of Chile. Then, we propose a mechanism capable to induce excitability in the grass population. The key of this mechanism is the grazing of herbivores. In order to give a more quantitative

description of the process, we model mathematically this mechanism in the framework of population dynamics. Specifically, we model the grass dynamics with an equation similar to the one used by Klausmeier [12], and the herbivore activity by the predator-prey Lotka-Volterra model [157, 158]. The resulting model is able to reproduce the spiral shaped pattern.

## 5.1 Field observations

In this section we document the observation of spiral patterns of grass biomass in high-altitude wetlands in the north of Chile. Grasses belong to genus “*deyeuxia*” [159]. Figure 5.1 displays the typical shape of these structures. They consist of a spiraled arm that emerges from a core point, as shown in Figure 5.1 a). It is also frequent to observe two cores connected by the same arm (see Figure 5.1 b). Figure 5.1 c) displays a larger zone populated with this sort of structures. In the convex (external) side of the spiral arm, taller plants are observed. The concave (internal) region of the spiral arm is in part covered by dead grass. This feature can be attributed to a rotating movement of the biomass due to the birth-death dynamics of the grass. Note that grazing is a relevant factor in the death of the grass on this area.

We have observed these spiral structures in a high-altitude wetland. Sufficiently close to the water, the biomass is uniformly distributed over the territory, while far from the water, the land is almost barren. Along the border of the vegetated zone where pattern formation takes place, regions with rings or spirals can be found.

More precisely, we have detected spiral formation in Bofedal de Quepiaco (4553 m above sea level), Vado Putana (4238 m above sea level) and Vado Incahuasi (4250 m above sea level, 2 km East of Vado Putana) in the surroundings of San Pedro de Atacama. Figures 5.2 a) and 5.2 b) show two of these locations, indicating where spirals have been found. Here, the

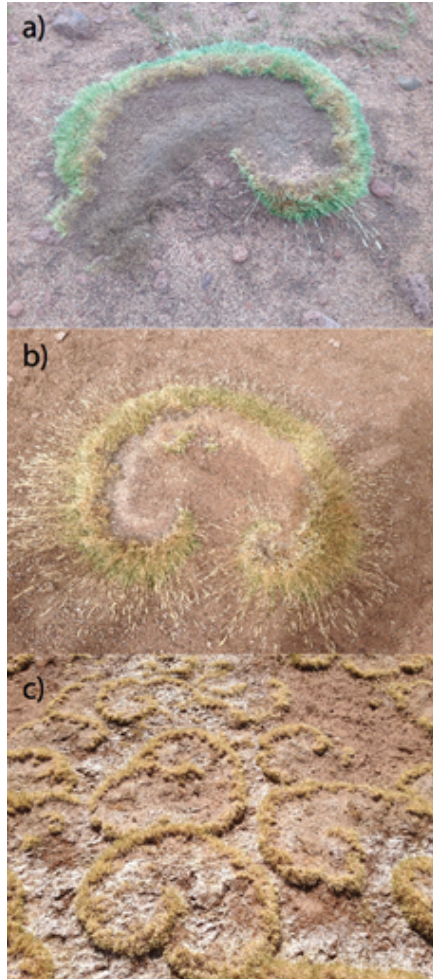


*Figure 5.1: Spiral vegetation patterns in the region of San Pedro de Atacama, Chile. The singular spiral in a) was photographed in Vado Putana, March 2015. The double spiral in b) was photographed in Bofedal de Quepiaco, March 2015. Several spirals in c) were photographed in Vado Putana, March 2014.*

| Measurement    | Length | Width | Int. height | Ext. height | $\alpha$ | $R^2$ |
|----------------|--------|-------|-------------|-------------|----------|-------|
| Average        | 2.24   | 0.084 | 0.019       | 0.038       | 0.16     | 0.91  |
| Std. Deviation | 0.73   | 0.043 | 0.008       | 0.016       | 0.12     | 0.10  |

*Table 5.1: Average data for 24 spiral patterns in the north of Chile. The table shows the average value and the standard deviation for the length, width, height, the Archimedean fit and the  $R^2$  of the Archimedean fit.*

grass is subject to adverse conditions. In fact, the climatological station of Machuca (9 km from Vado Putana) records an annual average temperature of 5.8 °C, and a total rainfall per year of 37 mm. Besides the adverse environmental conditions, vicunas (herbivore member of the South American camelids) graze in these zones, increasing the mortality rate of the grass, as other animals do in different high-Andean wetlands [160]. Figure 5.2 c) shows vicunas grazing in Vado Putana. We should emphasize that the above mentioned features of the wetlands are quite generic in Andean highlands, so spiral formations should be expected in other locations of Chile, Bolivia, Argentina, and Peru.

In table 5.1 we summarize the typical dimensions of the observed spirals. First row shows the average over 24 spirals, and the second row the standard deviation. Even though the dispersion is significant, showing some level of heterogeneity in the structures, the pattern takes place in the scale of a few meters, or less. As previously mentioned, it is possible to say from this data that the measure of biomass in the external side of the spiral arm is higher than the internal one.

We also measured the distance  $r$ , of a point in the arm, to the core of the spiral, as a function of the rotation angle  $\theta$ . In general, the assumption of Archimedean spiral  $r = \alpha(\theta - \theta_0)$  fits the data well, in agreement with the prediction made in the context of chemical reactions [148]. The last two columns of table 5.1 summarize our results for the Archimedean fit. The dispersion of  $\alpha$  is high. However, the coefficient  $R^2$  of the linear regression indicates a good linear fit for each individual spiral. Figure 5.3 shows spirals



*Figure 5.2: Regions where spiral vegetation patterns have been found. Figure a) shows Bofedal de Quepiaco ( $23^{\circ}4'55''$  S,  $67^{\circ}35'54''$  W), a wetland area in the 78 km of route 27 (East from San Pedro de Atacama in direction to Paso Jama). Figure b) shows Vado Putana ( $22^{\circ}32'12''$  S,  $68^{\circ}2'8''$  W), also a wetland, at 66 km North of San Pedro de Atacama along route B-245. Vicunas are seen grazing in these two locations. The square show the areas of several spirals in both places. Figure c) shows a group of vicunas grazing in Vado Putana, near the area with spirals.*

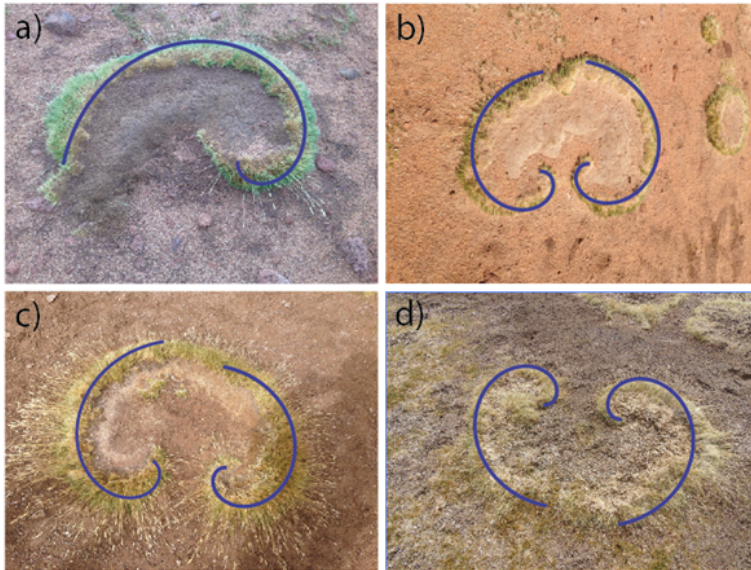


*Figure 5.3: Archimedean spirals (blue curves) overlapped onto spiral vegetation patterns. Spirals in a) and b) correspond to Vado Putana. Spirals in c) and d) correspond to Bofedal de Quepiaco.*

observed in the field with Archimedean spirals superimposed.

It is worthwhile to notice that the symmetry of chirality (the sense of rotation) does not seem to be broken in this process. In fact, we have observed the same number of clockwise-spirals and counterclockwise-spirals.

## 5.2 Mechanism for excitability

Winfrey [161] has speculated about the possibility of excitable behaviors in pastureland, and even conjectured the possible existence of what they called “fairy spirals”.

Our main hypothesis to explain spiral formation is related to the aridity and the presence of vicunas grazing in the zone. Under such adverse conditions, we have considered that the barren state is the only stable fixed point (if a stable vegetated state exists and its basin of attraction is small, then it is not relevant for the present discussion). The main ingredient is the excitability of the barren state, that can be explained as a sequence of basic steps: an external perturbation makes the grass biomass exceed a threshold; as a result the grass begins to grow; this increase in the biomass attracts the activity of herbivores in the zone; and this additional grazing leads to the local extinction of the grass. The lateral growth of the plants gives the necessary initial condition to trigger the local process. By incorporating the possibility of spatial heterogeneity, this excitable behavior leads to the formation of spiral waves which sustain the grass population.

### 5.3 Mathematical model

Even though many self-organization models have been proposed to describe pattern formation in arid or semiarid landscapes [11,15,19,50], in our present work we use the Klausmeier’s reaction-diffusion model [12]. This model was originally proposed to explain stripe formation in sloped landscapes [12,47], but it has also been used to model pattern formation in flat territories [40]. The model can be adapted to our hypothesis that states that the relevant ingredient for the existence of spirals is the interaction between the plants and the grazing of herbivores. We obtain from Klausmeier’s model [12,34,47] the dynamics of the vegetation and the value of water as a function of the biomass (neglecting the water dependence in time). Using this, we model the dynamics of the predator (we refer to the herbivores as the “predator”) by the standard Lotka-Volterra model [157,158]. Our chosen model has two advantages: its simplicity; and many of the values of its parameters have been already reported in the literature. More realistic models of grazing [162] and vegetation [19] also allowed the formation of spirals.

The original equations from the reaction-diffusion model in Klausmeier 1999 are

$$\begin{aligned}\partial_T N &= RJWN^2 - (M + V)N + \delta(\partial_{XX} + \partial_{YY})N, \\ \partial_T W &= A - LW - RWN^2 + U\partial_X W,\end{aligned}$$

where  $N(X, Y, T)$  is the grass biomass density and  $W(X, Y, t)$  is the water available in the soil. The parameter  $A$  is the water that arrives to the soil (basically underground sources that come from the wetland),  $M$  is the rate of biomass mortality without vicunas,  $V$  is the rate of biomass mortality induced by vicunas,  $L$  is the evaporation rate of water,  $RWN$  is the water uptake rate of plants,  $J$  is the biomass increase per unit of water consumed, the diffusion coefficient  $\delta$  represents the seed dispersion and the lateral growth of plants, and the value of  $U$  represents the slope of the topography. For simplicity, we assume that there are no other explicit spatial dependence. We split the rate of mortality into two contributions: the rate  $M$  without vicunas; and the rate  $V$  that depends only on the grazing pressure of vicunas [163].

Considering that water  $W$  changes much faster than the biomass density  $N$ , we consider that the water is in equilibrium for a given value of biomass density. Assuming for simplicity that the topography is flat ( $U = 0$ ), then we obtain

$$W = \frac{A}{L + RN^2}.$$

Finally, our Equation for the grazing of vicunas takes the same form as the well-known equation for predator dynamics in the Lotka-Volterra model [157,158]. Our full mathematical model is described by

$$\partial_T N = RJWN^2 - (M + V)N + \delta(\partial_{XX} + \partial_{YY})N, \quad (5.1)$$

$$\partial_T V = CVN - DV, \quad (5.2)$$

$$W = \frac{A}{L + RN^2}, \quad (5.3)$$

where  $V(X, Y, T)$  is a field that is related to the grazing of vicunas and represents the rate of biomass mortality related only with the grazing of vicunas. The grazing of vicunas increases at ratio  $CN$  and decreases at ratio  $D$ . Strictly speaking, the field  $V$  does not represent the density of vicunas, which are bigger than the spiral sizes. Here, in order to make a mean-field description of the vegetation dynamics, we have considered a “grazing field” that accounts for the presence of grazing activity. In other words,  $V$  should be directly seen as the grazing contribution to the mortality rate of grass, not as the vicuna density. Furthermore, this contribution to the mortality rate depends on the grass biomass due to the nonlinear predator-prey interaction, which we have modeled using the classical Lotka-Volterra model. For that reason, we have ignored any transport term (as diffusion) in Eq. (5.2); spatial heterogeneities in the field  $V$  are directly induced by heterogeneities in the grass biomass  $N$ .

## 5.4 Excitability of the system

In order to simplify our analytical analysis of the excitability of the model, we normalize the previous equations. Considering the value of  $W$  in Eq. (5.3) and the following change of variables

$$\begin{aligned} N &= n\sqrt{\frac{L}{R}}, \\ x &= X\sqrt{\frac{C}{\delta}}\sqrt{\frac{L}{R}}, \\ y &= Y\sqrt{\frac{C}{\delta}}\sqrt{\frac{L}{R}}, \\ M &= mC\sqrt{\frac{L}{R}}, \end{aligned}$$

$$\begin{aligned}
t &= TC\sqrt{\frac{L}{R}}, \\
A &= a\frac{CL}{JR}, \\
V &= vC\sqrt{\frac{L}{R}}, \\
D &= dC\sqrt{\frac{L}{R}},
\end{aligned} \tag{5.4}$$

equations (5.1) and (5.2) become the normalized equations

$$\partial_t n = \frac{an^2}{1+n^2} - (m+v)n + (\partial_{xx} + \partial_{yy})n \tag{5.5}$$

and

$$\partial_t v = nv - dv. \tag{5.6}$$

While the original equations have 8 parameters, the normalized equations (5.5) and (5.6) have 3. These normalized equations simplify the analysis of the dynamics and we use them to explain the mechanism of excitability.

Defining the functions

$$f(n, v) = \frac{an^2}{1+n^2} - (m+v)n$$

and

$$g(n, v) = nv - dv,$$

and ignoring for the sake of simplicity the spatial variations, we obtain a dynamical system of the form:

$$\begin{aligned}
\partial_t n &= f(n, v) \\
\partial_t v &= g(n, v)
\end{aligned}$$

Depending on the values of the three parameters, this system can have up to four fixed points  $S_i = (n_i, v_i)$ . The fixed point  $S_0 = (0, 0)$  always exists and is stable. The fixed point

$$S_1 = \left( \frac{a - \sqrt{a^2 - 4m^2}}{2m}, 0 \right)$$

is unstable and exists when  $a > 2m$ . The fixed point

$$S_2 = \left( \frac{a + \sqrt{a^2 - 4m^2}}{2m}, 0 \right)$$

exists also when  $a > 2m$ . This solution,  $S_2$ , is stable when  $d > n_2$  and is unstable when  $d < n_2$ . The last solution

$$S_3 = \left( d, \frac{ad}{1 + d^2} - m \right)$$

exists when  $ad > m(1 + d^2)$ . The solution  $S_3$  is stable when  $d > 1$  and is unstable when  $d < 1$ .

This system has another interesting feature; the zero solution  $S_0 = (0, 0)$  can be excitable if the parameters fulfill certain conditions. In other words, some small perturbations induce large excursions before returning to the zero solution. We observe this behavior when  $a > 2m$  and  $d < 1$ .

Figure 5.4 shows the phase portrait  $(n, v)$  in the regime of excitability. In the phase portrait we observe the nullclines  $f(n, v) = 0$  and  $g(n, v) = 0$ , the fixed points and the trajectory that is initiated at a point indicated by a square.

Therefore, the barren state  $S_0$  is the only stable fixed point in this region of parameters. If the initial condition verifies  $f(n, v) > 0$  (see Figure 5.4), the system performs a large excursion before returning to the barren state

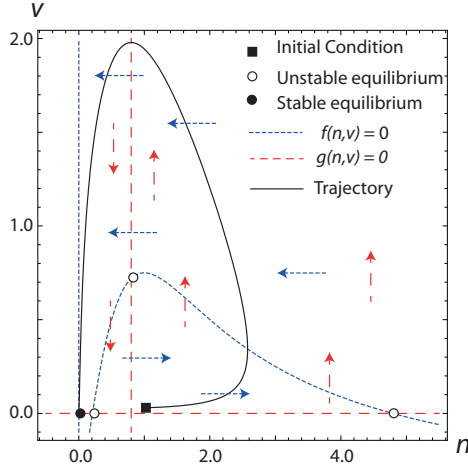


Figure 5.4: The phase portrait for Eqs. (5.5) and (5.6) with  $a = 2.5$ ,  $m = 0.5$ , and  $d = 0.8$ . The dashed lines represent the nullclines and the circles represent the fixed points as indicated in the legend. The solid curve represents a trajectory that begins at a point (solid square) located to the right of the unstable fixed point (open circle), and describes a large excursion before approaching the stable equilibrium (solid circle). The arrows represent the sign of  $f(n, v)$  and  $g(n, v)$  as indicated.

$S_0$ . In other words, the system displays an excitable loop that is induced by the grazing. Indeed, if we ignore the presence of vicunas (equivalent to fixing  $v = 0$  in our equations), the vegetated state  $S_2$  becomes stable and the system exhibits bistability instead of excitability.

## 5.5 Numerical simulations

By considering the presence of spatial heterogeneities, the previous mechanism (section 5.4) can induce the propagation of the excitation and can

sustain the presence of vegetation via a spatially structured pattern. For instance, in one spatial dimension a local perturbation can excite its vicinity and generate a “grass pulse” that advances with constant speed over the barren state.

In two spatial dimensions, a possible realization of a constant-speed wave front takes the shape of a spiral that rotates with constant frequency. In Winfree 1972 [148], the author shows that in the context of chemical reactions, the rotating pattern has (ignoring higher-order effects of curvature) the shape of an Archimedean spiral. This geometric implication is generic and applies to the vegetation model proposed in this article.

We have considered vegetation parameters according to literature of vegetation dynamics in semiarid conditions [12, 62]. Figure 5.5 displays the typical spiral waves exhibited by the model in this regime. In this figure the size of the spirals are of the order of 2m in length and 6cm in width, in agreement with the field data from table 5.1. The period of spirals (the time to rotate  $360^\circ$ ) in Figure 5.5 is of the order of 5 years. Nonetheless, long term measurements are necessary to obtain a precise value.

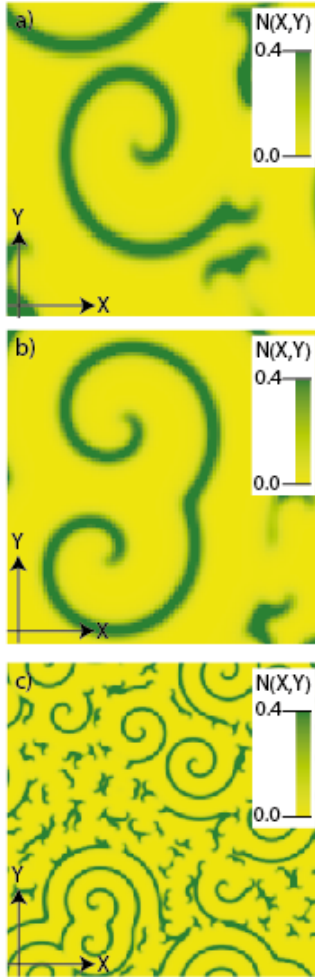


Figure 5.5: Numerical simulations of spirals based on our model equations (1), (2) and (3). Figure A shows a single spiral in 1 m<sup>2</sup>. Figure B shows a double spiral in 1 m<sup>2</sup>. Figure C shows several spirals in 16 m<sup>2</sup>. The parameters are  $L=4$  [year<sup>-1</sup>],  $R=100$  [year<sup>-1</sup> kg<sup>-2</sup> m<sup>4</sup>],  $J=0.003$ ,  $M=1.8$  [year<sup>-1</sup>],  $\delta = 10^{-4}6.25$ [m<sup>2</sup>/year],  $C=20$  [m<sup>2</sup> kg<sup>-1</sup> year<sup>-1</sup>],  $D=2$  and  $A=666.6$  [kg m<sup>-2</sup> year<sup>-1</sup>].

## Chapter 6

# Conclusions and discussion

Desertification is a central problem in ecology. Our ability to understand how vegetation manages to survive in arid and semiarid ecosystems can help in the development of future strategies to preserve or make use of scarce soil resources. The aim of this thesis is, through mathematical models, understand how arid or semiarid ecosystems restore and preserve the vegetation. We have focused particularly on the effect of nonlocal interactions between individual plants, and the self-organization of vegetation on flat landscapes. This type of research is necessary to set the base of an adequate biological productivity of arid and semiarid ecosystems.

In this thesis, we have investigated the role of a strong nonlocal coupling in a bistable model. This prototype model of population dynamics could be applied to vegetation dynamics. In this context, we have shown that, far from any symmetry breaking instability, localized vegetation structures can be stabilized for large values of the aridity parameter. Their formation is attributed to the interaction between fronts mediated by a strong nonlocal coupling in the form of a Lorentzian. We have identified the following scenario. By increasing the level of the aridity, a large bare area embedded

in a uniform vegetated state can be formed. This structure has a single fringe peak that appears in the spatial profile of the biomass. We have interpreted this behavior as a fairy circle. When increasing further the degree of aridity, flat spots of vegetation can be formed in the system. These structures have a peak surrounded by the bare state. Both localized structures have varying width as a function of aridity. In contrast, the width of localized vegetation structures, which are close to the symmetry breaking instability, is determined by the most unstable wavelength [66]. We have established analytically a formula, in one-dimensional systems, for the width of fairy circles and flat spots as functions of the level of aridity. The width of these localized structures is intrinsic to the dynamics of arid ecosystems and is independent of external environmental effects, such as termites or ants. In addition, we have studied the interaction between fairy circles. We have found a formula that describes the relation between the parameters of the system, the size of the fairy circles and the distance between them. The results of direct numerical simulations of our strong nonlocal bistable model agree with the analytical findings. The analytical results are in one dimension. However, we expect to develop the equivalent in two dimensions in the near future.

We applied the aforementioned mechanism based on strong nonlocal coupling to realistic models of vegetation in arid regions. Numerical simulations show how the circular shape of fairy circles are formed. In agreement with field observations, we prove that as the aridity parameter increases, the diameter of fairy circles increases as well. Two ecological models are used to understand the formation and the influence of the aridity level on the formation of fairy circles. We attribute their stabilization to two main ingredients. First, the ecosystem should operate in the bistability region between homogeneous states. Second, the strong competitive interaction between plants should be incorporated in the modeling. Termites or other external factors could create initial conditions for the formation of fairy circles. However, they do not explain the observed circular shape. Our mechanism leading to the formation of stable fairy circles could be applied to various spatially extended systems with strong nonlocal coupling such as optics (see appendix

A). Nevertheless, on this topic, it is important to carry out more controlled experiments to confirm the results.

All previous results are obtained in a regime far from any symmetry breaking instability. In the second part of this thesis, we have investigated the formation of localized structures of vegetation in the vicinity of a symmetry breaking instability. We show that systems of vegetation spots made of clonal plants, observable in the Andes (Bolivia), can be interpreted as localized structures. In order to understand this phenomenon, we have studied a generic interaction-redistribution model which considers weak nonlocal interaction. We have found that this model replicates the main features of the observed spots of vegetation, considering realistic parameters. Yet, to progress in our understanding of the phenomenon, we need additional observations at landscape and plant scales. On a broader scale, it would be useful to acquire aerial photographs of patterns to check their characteristics over rainfall gradients. In the Sajama National Park patterns look aperiodic, while spots appear to have a modal size. Nonetheless, this should be systematically checked in diverse locations and conditions. If our interpretation based on localized structures is correct, spots systems may shift towards periodic structures under wetter climates.

In the last part of this thesis, we have reported the appearance of spiral vegetation patterns in high-altitude wetlands in the north of Chile. These formations can be attributed to an excitable behavior of the barren state. We have proposed a mechanism, for this excitable behavior, based on the interaction between the grass and its predator (an herbivore member of the South American camelids, the vicuna), and the adverse environmental conditions of the zone. The numerical simulations of the mathematical model, which account for the excitability of the barren state, agree with field observations. It has been considered a simple model to describe plants dynamics. However, other models that include more sophisticated interactions such as nonlocal coupling between plants [11, 19, 27, 60] could induce spirals if we consider the interaction between plants and grazing of animals. We could take into account other ways to include the “predator-prey” interaction be-

tween herbivores and plants [93,162].

# Bibliography

- [1] W. A. Macfadyen, "Vegetation patterns in the semi-desert plains of british somaliland," *The Geographical Journal* **116**(4/6), pp. 199–211, 1950.
- [2] W. Macfadyen, "Soil and vegetation in british somaliland," *Nature* **165**, p. 121, 1950.
- [3] P. Greig-Smith, "Pattern in vegetation," *Journal of Ecology* **67**(3), pp. 755–779, 1979.
- [4] R. L. Ives, "Desert ripples [n. am.]," *American Journal of Science* **244**(7), pp. 492–501, 1946.
- [5] G. A. Worrall, "Tree patterns in the sudan," *Journal of Soil Science* **11**(1), pp. 63–67, 1960.
- [6] L. White, "Vegetation arcs in jordan," *The Journal of Ecology* , pp. 461–464, 1969.
- [7] G. A. Worrall, "The butana grass patterns," *Journal of Soil Science* **10**(1), pp. 34–53, 1959.
- [8] L. White, "Brousse tigrée patterns in southern niger," *The Journal of Ecology* , pp. 549–553, 1970.

- [9] L. White, "Vegetation stripes on sheet wash surfaces," *The Journal of Ecology*, pp. 615–622, 1971.
- [10] V. Deblauwe, *Modulation des structures de végétation auto-organisées en milieu aride*. PhD thesis, Université Libre de Bruxelles, 2010.
- [11] R. Lefever and O. Lejeune, "On the origin of tiger bush," *Bulletin of Mathematical Biology* **59**(2), pp. 263–294, 1997.
- [12] C. A. Klausmeier, "Regular and irregular patterns in semiarid vegetation," *Science* **284**(5421), pp. 1826–1828, 1999.
- [13] O. Lejeune and M. Tlidi, "A model for the explanation of vegetation stripes (tiger bush)," *Journal of Vegetation Science* **10**(2), pp. 201–208, 1999.
- [14] O. Lejeune, P. Couteron, and R. Lefever, "Short range co-operativity competing with long range inhibition explains vegetation patterns," *Acta Oecologica* **20**(3), pp. 171 – 183, 1999.
- [15] J. von Hardenberg, E. Meron, M. Shachak, and Y. Zarmi, "Diversity of vegetation patterns and desertification," *Phys. Rev. Lett.* **87**, p. 198101, Oct 2001.
- [16] P. Couteron and O. Lejeune, "Periodic spotted patterns in semi-arid vegetation explained by a propagation-inhibition model," *Journal of Ecology* **89**(4), pp. 616–628, 2001.
- [17] E. Meron, E. Gilad, J. von Hardenberg, M. Shachak, and Y. Zarmi, "Vegetation patterns along a rainfall gradient," *Chaos, Solitons & Fractals* **19**(2), pp. 367–376, 2004.
- [18] M. Rietkerk, S. C. Dekker, P. C. de Ruiter, and J. van de Koppel, "Self-organized patchiness and catastrophic shifts in ecosystems," *Science* **305**(5692), pp. 1926–1929, 2004.

- [19] E. Gilad, J. von Hardenberg, A. Provenzale, M. Shachak, and E. Meron, “Ecosystem engineers: From pattern formation to habitat creation,” *Phys. Rev. Lett.* **93**, p. 098105, Aug 2004.
- [20] M. Rietkerk and J. van de Koppel, “Regular pattern formation in real ecosystems,” *Trends in Ecology & Evolution* **23**(3), pp. 169 – 175, 2008.
- [21] F. Borgogno, P. D’Odorico, F. Laio, and L. Ridolfi, “Mathematical models of vegetation pattern formation in ecohydrology,” *Reviews of Geophysics* **47**(1), p. RG1005, 2009. RG1005.
- [22] V. Deblauwe, N. Barbier, P. Couteron, O. Lejeune, and J. Bogaert, “The global biogeography of semi-arid periodic vegetation patterns,” *Global Ecology and Biogeography* **17**(6), pp. 715–723, 2008.
- [23] V. Deblauwe, P. Couteron, O. Lejeune, J. Bogaert, and N. Barbier, “Environmental modulation of self-organized periodic vegetation patterns in sudan,” *Ecography* **34**(6), pp. 990–1001, 2011.
- [24] R. Lefever and J. W. Turner, “A quantitative theory of vegetation patterns based on plant structure and the non-local fkpp equation,” *Comptes Rendus Mecanique* **340**(11), pp. 818 – 828, 2012.
- [25] O. Lejeune, M. Tlidi, and R. Lefever, “Vegetation spots and stripes: Dissipative structures in arid landscapes,” *International Journal of Quantum Chemistry* **98**(2), pp. 261–271, 2004.
- [26] E. Gilad, J. von Hardenberg, A. Provenzale, M. Shachak, and E. Meron, “A mathematical model of plants as ecosystem engineers,” *Journal of Theoretical Biology* **244**(4), pp. 680 – 691, 2007.
- [27] R. Lefever, N. Barbier, P. Couteron, and O. Lejeune, “Deeply gapped vegetation patterns: On crown/root allometry, criticality and desertification,” *Journal of Theoretical Biology* **261**(2), pp. 194 – 209, 2009.

- [28] E. Meron, “Pattern-formation approach to modelling spatially extended ecosystems,” *Ecological Modelling* **234**, pp. 70 – 82, 2012. Modelling clonal plant growth: From Ecological concepts to Mathematics.
- [29] R. A. Fisher, “The wave of advance of advantageous genes,” *Annals of Eugenics* **7**(4), pp. 355–369, 1937.
- [30] A. N. Kolmogorov, I. G. Petrovsky, and N. S. Piskunov, “Etude de l’équation de la diffusion avec croissance de la quantité de matière et son application à un problème biologique,” *Moscow Univ. Math. Bull* **1**, pp. 1–25, 1937.
- [31] P. F. Verhulst, “Recherches mathématiques sur la loi d’accroissement de la population.,” *Nouveaux Mémoires de l’Académie Royale des Sciences et Belles-Lettres de Bruxelles* **18**, pp. 14–54, 1845.
- [32] R. Martinez-Garcia, J. M. Calabrese, E. Hernandez-Garcia, and C. Lopez, “Vegetation pattern formation in semiarid systems without facilitative mechanisms,” *Geophysical Research Letters* **40**(23), pp. 6143–6147, 2013.
- [33] R. Martinez-Garcia, J. M. Calabrese, E. Hernandez-Garcia, and C. Lopez, “Minimal mechanisms for vegetation patterns in semi-arid regions,” *Philosophical Transactions of the Royal Society of London A: Mathematical, Physical and Engineering Sciences* **372**(2027), p. 20140068, 2014.
- [34] J. A. Sherratt and G. J. Lord, “Nonlinear dynamics and pattern bifurcations in a model for vegetation stripes in semi-arid environments,” *Theoretical Population Biology* **71**(1), pp. 1 – 11, 2007.
- [35] A. Manor and N. M. Shnerb, “Facilitation, competition, and vegetation patchiness: From scale free distribution to patterns,” *Journal of Theoretical Biology* **253**(4), pp. 838 – 842, 2008.

- [36] J. A. Sherratt, “Pattern solutions of the klausmeier model for banded vegetation in semi-arid environments i,” *Nonlinearity* **23**(10), p. 2657, 2010.
- [37] J. A. Sherratt, “Pattern solutions of the klausmeier model for banded vegetation in semi-arid environments ii: patterns with the largest possible propagation speeds,” *Proceedings of the Royal Society of London A: Mathematical, Physical and Engineering Sciences* **467**(2135), pp. 3272–3294, 2011.
- [38] G. Bel, A. Hagberg, and E. Meron, “Gradual regime shifts in spatially extended ecosystems,” *Theoretical Ecology* **5**(4), pp. 591–604, 2012.
- [39] J. A. Sherratt and A. D. Synodinos, “Vegetation patterns and desertification waves in semi-arid environments: mathematical models based on local facilitation in plants,” *Discrete Cont Dyn Syst Ser B* **17**, pp. 2815–2827, 2012.
- [40] Y. R. Zelnik, S. Kinast, H. Yizhaq, G. Bel, and E. Meron, “Regime shifts in models of dryland vegetation,” *Philosophical Transactions of the Royal Society of London A: Mathematical, Physical and Engineering Sciences* **371**(2004), p. 20120358, 2013.
- [41] J. A. Sherratt, “History-dependent patterns of whole ecosystems,” *Ecological Complexity* **14**, pp. 8 – 20, 2013. Special Issue on the occasion of Horst Malchow’s 60th birthday.
- [42] J. A. Sherratt, “Pattern solutions of the klausmeier model for banded vegetation in semi-arid environments iii: The transition between homoclinic solutions,” *Physica D: Nonlinear Phenomena* **242**(1), pp. 30 – 41, 2013.
- [43] J. A. Sherratt, “Pattern solutions of the klausmeier model for banded vegetation in semiarid environments iv: Slowly moving patterns and their stability,” *SIAM Journal on Applied Mathematics* **73**(1), pp. 330–350, 2013.

- [44] J. A. Sherratt, “Pattern solutions of the klausmeier model for banded vegetation in semiarid environments v: The transition from patterns to desert,” *SIAM Journal on Applied Mathematics* **73**(4), pp. 1347–1367, 2013.
- [45] H. Yizhaq, S. Sela, T. Svoray, S. Assouline, and G. Bel, “Effects of heterogeneous soil-water diffusivity on vegetation pattern formation,” *Water Resources Research* **50**(7), pp. 5743–5758, 2014.
- [46] K. Gowda, H. Riecke, and M. Silber, “Transitions between patterned states in vegetation models for semiarid ecosystems,” *Phys. Rev. E* **89**, p. 022701, Feb 2014.
- [47] J. A. Sherratt, “Using wavelength and slope to infer the historical origin of semiarid vegetation bands,” *Proceedings of the National Academy of Sciences* **112**(14), pp. 4202–4207, 2015.
- [48] E. Meron, *Nonlinear physics of ecosystems*, CRC Press, Boca Raton, 2015.
- [49] R. HilleRisLambers, M. Rietkerk, F. van den Bosch, H. H. T. Prins, and H. de Kroon, “Vegetation pattern formation in semi-arid grazing systems,” *Ecology* **82**(1), pp. 50–61, 2001.
- [50] M. Rietkerk, M. C. Boerlijst, F. Langevelde, R. HilleRisLambers, J. van de Koppel, L. Kumar, H. H. T. Prins, and A. A. M. de Roos, “Self-organization of vegetation in arid ecosystems,” *The American Naturalist* **160**(4), pp. 524–530, 2002.
- [51] P. D’Odorico, F. Laio, and L. Ridolfi, “Vegetation patterns induced by random climate fluctuations,” *Geophysical Research Letters* **33**(19), p. L19404, 2006. L19404.
- [52] L. Ridolfi, P. D’Odorico, and F. Laio, *Noise-induced phenomena in the environmental sciences*, Cambridge University Press, 2011.

- [53] R. Martinez-Garcia, J. M. Calabrese, and C. Lopez, “Spatial patterns in mesic savannas: The local facilitation limit and the role of demographic stochasticity,” *Journal of Theoretical Biology* **333**, pp. 156 – 165, 2013.
- [54] A. J. Sherratt, “An analysis of vegetation stripe formation in semi-arid landscapes,” *Journal of Mathematical Biology* **51**(2), pp. 183–197, 2005.
- [55] T. Okayasu and Y. Aizawa, “Systematic analysis of periodic vegetation patterns,” *Progress of Theoretical Physics* **106**(4), pp. 705–720, 2001.
- [56] O. Lejeune, M. Tlidi, and P. Couteron, “Localized vegetation patches: A self-organized response to resource scarcity,” *Phys. Rev. E* **66**, p. 010901, Jul 2002.
- [57] P. D’Odorico, F. Laio, and L. Ridolfi, “Patterns as indicators of productivity enhancement by facilitation and competition in dryland vegetation,” *Journal of Geophysical Research: Biogeosciences* **111**(G3), p. G03010, 2006. G03010.
- [58] E. Meron, H. Yizhaq, and E. Gilad, “Localized structures in dryland vegetation: Forms and functions,” *Chaos* **17**(3), p. 037109, 2007.
- [59] P. Couteron, F. Anthelme, M. Clerc, D. Escaff, C. Fernandez-Oto, and M. Tlidi, “Plant clonal morphologies and spatial patterns as self-organized responses to resource-limited environments,” *Philosophical Transactions of the Royal Society of London A: Mathematical, Physical and Engineering Sciences* **372**(2027), p. 20140102, 2014.
- [60] E. Sheffer, H. Yizhaq, E. Gilad, M. Shachak, and E. Meron, “Why do plants in resource-deprived environments form rings?,” *Ecological Complexity* **4**(4), pp. 192 – 200, 2007.
- [61] J. von Hardenberg, A. Y. Kletter, H. Yizhaq, J. Nathan, and E. Meron, “Periodic versus scale-free patterns in dryland vegetation,”

*Proceedings of the Royal Society of London B: Biological Sciences* **277**, pp. 1771 – 1776, 2010.

- [62] E. Sheffer, H. Yizhaq, M. Shachak, and E. Meron, “Mechanisms of vegetation-ring formation in water-limited systems,” *Journal of Theoretical Biology* **273**(1), pp. 138 – 146, 2011.
- [63] G. Theron, “Die verskynsel van kaal kolle in kaokoland, suidwes-afrika,” *Journal of the South African Biological Society* **20**, pp. 43–53, 1979.
- [64] E. Moll, “The origin and distribution of fairy rings in namibia,” in *Proceedings of the 13th Plenary Meeting AETFAT, Malawi*, **2**, pp. 1203–1209, 1994.
- [65] M. van Rooyen, G. Theron, N. van Rooyen, W. Jankowitz, and W. Matthews, “Mysterious circles in the namib desert: review of hypotheses on their origin,” *Journal of Arid Environments* **57**(4), pp. 467 – 485, 2004.
- [66] M. Tlidi, R. Lefever, and A. Vladimirov, *On Vegetation Clustering, Localized Bare Soil Spots and Fairy Circles*, pp. 1–22. Springer Berlin Heidelberg, Berlin, Heidelberg, 2008.
- [67] M. D. Cramer and N. N. Barger, “Are namibian "fairy circles"? the consequence of self-organizing spatial vegetation patterning?,” *PLoS ONE* **8**, pp. 1–12, 08 2013.
- [68] N. Juergens, “The biological underpinnings of namib desert fairy circles,” *Science* **339**(6127), pp. 1618–1621, 2013.
- [69] C. Fernandez-Oto, M. Tlidi, D. Escaff, and M. G. Clerc, “Strong interaction between plants induces circular barren patches: fairy circles,” *Philosophical Transactions of the Royal Society of London A: Mathematical, Physical and Engineering Sciences* **372**(2027), p. 20140009, 2014.

- [70] S. Getzin, K. Wiegand, T. Wiegand, H. Yizhaq, J. von Hardenberg, and E. Meron, “Clarifying misunderstandings regarding vegetation self-organisation and spatial patterns of fairy circles in namibia: a response to recent termite hypotheses,” *Ecological Entomology* **40**(6), pp. 669–675, 2015.
- [71] S. Getzin, H. Yizhaq, B. Bell, T. E. Erickson, A. C. Postle, I. Katra, O. Tzuk, Y. R. Zelnik, K. Wiegand, T. Wiegand, and E. Meron, “Discovery of fairy circles in australia supports self-organization theory,” *Proceedings of the National Academy of Sciences* **113**(13), pp. 3551–3556, 2016.
- [72] W. R. Tschinkel, “The life cycle and life span of namibian fairy circles,” *PLoS ONE* **7**, pp. 1–17, 06 2012.
- [73] C. Fernandez-Oto, M. G. Clerc, D. Escaff, and M. Tlidi, “Strong non-local coupling stabilizes localized structures: An analysis based on front dynamics,” *Phys. Rev. Lett.* **110**, p. 174101, Apr 2013.
- [74] S. Getzin, K. Wiegand, T. Wiegand, H. Yizhaq, J. von Hardenberg, and E. Meron, “Adopting a spatially explicit perspective to study the mysterious fairy circles of namibia,” *Ecography* **38**(1), pp. 1–11, 2014.
- [75] W. R. Tschinkel, “Experiments testing the causes of namibian fairy circles,” *PLoS ONE* **10**, pp. 1–22, 10 2015.
- [76] Y. R. Zelnik, E. Meron, and G. Bel, “Gradual regime shifts in fairy circles,” *Proceedings of the National Academy of Sciences* **112**(40), pp. 12327–12331, 2015.
- [77] M. D. Cramer, N. N. Barger, and W. R. Tschinkel, “Edaphic properties enable facilitative and competitive interactions resulting in fairy circle formation,” *Ecography*, 2016. Accepted.
- [78] T. Becker and S. Getzin, “The fairy circles of kaokoland (north-west namibia) origin, distribution, and characteristics,” *Basic and Applied Ecology* **1**(2), pp. 149 – 159, 2000.

- [79] C. Albrecht, J. Joubert, and P. De Rycke, "Origin of the enigmatic, circular, barren patches ('fairy rings') of the pro-namib," *South African Journal of Science* **97**(1), pp. 23–28, 2001.
- [80] T. Becker, "Das phänomen der feenkreise (fairy circles) im kaokoland (nw namibia)," *Basic and Applied Dryland Research* **1**, pp. 121–137, 11 2007.
- [81] N. Juergens, K. E. P. Vlieghe, C. Bohn, B. Erni, F. Gunter, J. Oldeland, B. Rudolph, and M. D. Picker, "Weaknesses in the plant competition hypothesis for fairy circle formation and evidence supporting the sand termite hypothesis," *Ecological Entomology* **40**(6), pp. 661–668, 2015.
- [82] N. Juergens, "Exploring common ground for different hypotheses on namib fairy circles," *Ecography* **38**(1), pp. 12–14, 2015.
- [83] K. Vlieghe, M. Picker, V. Ross-Gillespie, and B. Erni, "Herbivory by subterranean termite colonies and the development of fairy circles in sw namibia," *Ecological Entomology* **40**(1), pp. 42–49, 2015.
- [84] M. D. Picker, V. Ross-Gillespie, K. Vlieghe, and E. Moll, "Ants and the enigmatic namibian fairy circles-cause and effect?," *Ecological Entomology* **37**(1), pp. 33–42, 2012.
- [85] J. Meyer, F. Senejoux, H. Heyman, N. Meyer, and M. Meyer, "The occurrence of triterpenoids from euphorbia gummifera inside the fairy circles of garub in the southern namibian pro-desert," *South African Journal of Botany* **98**, pp. 10 – 15, 2015.
- [86] J.-B. Ramond, A. Pienaar, A. Armstrong, M. Seely, and D. A. Cowan, "Niche-partitioning of edaphic microbial communities in the namib desert gravel plain fairy circles," *PLoS ONE* **9**, pp. 1–9, 10 2014.
- [87] W. Jankowitz, M. V. Rooyen, D. Shaw, J. Kaumba, and N. V. Rooyen, "Mysterious circles in the namib desert," *South African Journal of Botany* **74**(2), pp. 332 – 334, 2008.

- [88] Y. Naude, M. van Rooyen, and E. Rohwer, “Evidence for a geochemical origin of the mysterious circles in the pro-namib desert,” *Journal of Arid Environments* **75**(5), pp. 446 – 456, 2011.
- [89] L. Fraley, “Response of shortgrass plains vegetation to gamma radiation-iii. nine years of chronic irradiation,” *Environmental and Experimental Botany* **27**(2), pp. 193 – 201, 1987.
- [90] F. J. Walsh, A. D. Sparrow, P. Kendrick, and J. Schofield, “Fairy circles or ghosts of termitaria? pavement termites as alternative causes of circular patterns in vegetation of desert australia,” *Proceedings of the National Academy of Sciences* **113**(37), pp. E5365–E5367, 2016.
- [91] D. Escaff, C. Fernandez-Oto, M. G. Clerc, and M. Tlidi, “Localized vegetation patterns, fairy circles, and localized patches in arid landscapes,” *Phys. Rev. E* **91**, p. 022924, Feb 2015.
- [92] V. S. Zykov and A. T. Winfree, *Simulation of Wave Processes in Excitable Media*, John Wiley & Sons, Inc., New York, USA, 1992.
- [93] J. D. Murray, *Mathematical biology I: an introduction*, Springer-Verlag, New York, 3rd ed., 2002.
- [94] P. Mandel and M. Tlidi, “Transverse dynamics in cavity nonlinear optics (2000-2003),” *Journal of Optics B: Quantum and Semiclassical Optics* **6**(9), p. R60, 2004.
- [95] A. Ankiewicz and N. Akhmediev, *Dissipative Solitons: From Optics to Biology and Medicine*, Springer, Berlin Heidelberg, 2008.
- [96] O. Descalzi, M. G. Clerc, S. Residori, and G. Assanto, *Localized states in physics: solitons and patterns*, Springer, New York, USA, 2011.
- [97] M. Tlidi, K. Staliunas, K. Panajotov, A. G. Vladimirov, and M. G. Clerc, “Localized structures in dissipative media: from optics to plant ecology,” *Philosophical Transactions of the Royal Society of London A: Mathematical, Physical and Engineering Sciences* **372**(2027), p. 20140101, 2014.

- [98] P. Glansdorff and I. Prigogine, *Structure, stability and fluctuations*, 1971.
- [99] C. Lopez and E. Hernandez-Garcia, “Fluctuations impact on a pattern-forming model of population dynamics with non-local interactions,” *Physica D: Nonlinear Phenomena* **199**, pp. 223 – 234, 2004. Trends in Pattern Formation: Stability , Control and Fluctuations.
- [100] Y. Takeuchi, Y. Iwasa, and K. Sato, *Mathematics for life science and medicine*, Springer, Berlin Heidelberg, 2007.
- [101] M. G. Clerc, D. Escaff, and V. M. Kenkre, “Patterns and localized structures in population dynamics,” *Phys. Rev. E* **72**, p. 056217, Nov 2005.
- [102] M. G. Clerc, D. Escaff, and V. M. Kenkre, “Analytical studies of fronts, colonies, and patterns: Combination of the allee effect and nonlocal competition interactions,” *Phys. Rev. E* **82**, p. 036210, Sep 2010.
- [103] M. Tlidi, P. Mandel, and R. Lefever, “Localized structures and localized patterns in optical bistability,” *Phys. Rev. Lett.* **73**, pp. 640–643, Aug 1994.
- [104] J. Wu, R. Keolian, and I. Rudnick, “Observation of a nonpropagating hydrodynamic soliton,” *Phys. Rev. Lett.* **52**, pp. 1421–1424, Apr 1984.
- [105] P. B. Umbanhowar, F. Melo, and H. L. Swinney, “Localized excitations in a vertically vibrated granular layer,” *Nature* **382**(6594), pp. 793–796, 1996.
- [106] S. Coombes, “Waves, bumps, and patterns in neural field theories,” *Biological Cybernetics* **93**(2), pp. 91–108, 2005.
- [107] L. Gelens, D. Gomila, G. Van der Sande, M. A. Matias, and P. Colet, “Nonlocality-induced front-interaction enhancement,” *Phys. Rev. Lett.* **104**, p. 154101, Apr 2010.

- [108] P. Colet, M. A. Matías, L. Gelens, and D. Gomila, “Formation of localized structures in bistable systems through nonlocal spatial coupling. i. general framework,” *Phys. Rev. E* **89**, p. 012914, Jan 2014.
- [109] L. Gelens, M. A. Matías, D. Gomila, T. Dorissen, and P. Colet, “Formation of localized structures in bistable systems through nonlocal spatial coupling. ii. the nonlocal ginzburg-landau equation,” *Phys. Rev. E* **89**, p. 012915, Jan 2014.
- [110] D. Escaff, “Non-local defect interaction in one-dimension: weak versus strong non-locality,” *The European Physical Journal D* **62**(1), pp. 33–38, 2011.
- [111] Y. Kuramoto, D. Battogtokh, and H. Nakao, “Multiaffine chemical turbulence,” *Phys. Rev. Lett.* **81**, pp. 3543–3546, Oct 1998.
- [112] S.-i. Shima and Y. Kuramoto, “Rotating spiral waves with phase-randomized core in nonlocally coupled oscillators,” *Phys. Rev. E* **69**, p. 036213, Mar 2004.
- [113] L. Gelens, G. Van der Sande, P. Tassin, M. Tlidi, P. Kockaert, D. Gomila, I. Veretennicoff, and J. Danckaert, “Impact of nonlocal interactions in dissipative systems: Towards minimal-sized localized structures,” *Phys. Rev. A* **75**, p. 063812, Jun 2007.
- [114] X. Hutsebaut, C. Cambournac, M. Haelterman, J. Beeckman, and K. Neyts, “Measurement of the self-induced waveguide of a solitonlike optical beam in a nematic liquid crystal,” *J. Opt. Soc. Am. B* **22**, pp. 1424–1431, Jul 2005.
- [115] J. F. Henninot, J. F. Blach, and M. Warenghem, “Experimental study of the nonlocality of spatial optical solitons excited in nematic liquid crystal,” *Journal of Optics A: Pure and Applied Optics* **9**(1), p. 20, 2007.

- [116] A. Minovich, D. N. Neshev, A. Dreischuh, W. Krolikowski, and Y. S. Kivshar, “Experimental reconstruction of nonlocal response of thermal nonlinear optical media,” *Opt. Lett.* **32**, pp. 1599–1601, Jun 2007.
- [117] H. F. Howe and L. C. Westley, *Ecology of Pollination and Seed Dispersal*, pp. 262–283. Blackwell Publishing Ltd., 2009.
- [118] H. McKean, “Nagumo’s equation,” *Advances in Mathematics* **4**(3), pp. 209 – 223, 1970.
- [119] M. Kot, *Elements of mathematical ecology*, Cambridge University Press, 2001.
- [120] A. M. Turing, “The chemical basis of morphogenesis,” *Philosophical Transactions of the Royal Society of London B: Biological Sciences* **237**(641), pp. 37–72, 1952.
- [121] W. van Saarloos, “Front propagation into unstable states,” *Physics Reports* **386**, pp. 29 – 222, 2003.
- [122] P. C. Fife and J. B. McLeod, “The approach of solutions of nonlinear diffusion equations to travelling wave solutions,” *Bull. Amer. Math. Soc.* **81**, pp. 1076–1078, 11 1975.
- [123] P. C. Fife, *Mathematical aspects of reacting and diffusing systems*, vol. 28, Springer-Verlag, New York, 1979.
- [124] M. C. Cross and P. C. Hohenberg, “Pattern formation outside of equilibrium,” *Rev. Mod. Phys.* **65**, pp. 851–1112, Jul 1993.
- [125] P. Coullet, “Localized patterns and fronts in nonequilibrium systems,” *International Journal of Bifurcation and Chaos* **12**(11), pp. 2445–2457, 2002.
- [126] Y. Pomeau, “Front motion, metastability and subcritical bifurcations in hydrodynamics,” *Physica D: Nonlinear Phenomena* **23**(1), pp. 3 – 11, 1986.

- [127] R. E. Goldstein, G. H. Gunaratne, L. Gil, and P. Coulet, “Hydrodynamic and interfacial patterns with broken space-time symmetry,” *Phys. Rev. A* **43**, pp. 6700–6721, Jun 1991.
- [128] A. G. Vladimirov, R. Lefever, and M. Tlidi, “Relative stability of multipeak localized patterns of cavity solitons,” *Phys. Rev. A* **84**, p. 043848, Oct 2011.
- [129] N. Barbier, P. Couteron, R. Lefever, V. Deblauwe, and O. Lejeune, “Spatial decoupling of facilitation and competition at the origin of gapped vegetation patterns,” *Ecology* **89**(6), pp. 1521–1531, 2008.
- [130] J. Nathan, Y. Osem, M. Shachak, and E. Meron, “Linking functional diversity to resource availability and disturbance: a mechanistic approach for water-limited plant communities,” *Journal of Ecology* **104**(2), pp. 419–429, 2016.
- [131] E. Gilad, M. Shachak, and E. Meron, “Dynamics and spatial organization of plant communities in water-limited systems,” *Theoretical Population Biology* **72**(2), pp. 214 – 230, 2007.
- [132] D. Barthelemy and Y. Caraglio, “Plant architecture: A dynamic, multilevel and comprehensive approach to plant form, structure and ontogeny,” *Annals of Botany* **99**(3), pp. 375–407, 2007.
- [133] I. Bordeu, M. G. Clerc, P. Couteron, R. Lefever, and M. Tlidi, “Self-replication of localized vegetation patches in scarce environments,” *Scientific Reports* **6**, p. 33703, 2016.
- [134] M. E. Cerfonteyn, P. C. Roux Le, B. J. Vuuren Van, and C. Born, “Cryptic spatial aggregation of the cushion plant *azorella selago* (apiaceae) revealed by a multilocus molecular approach suggests frequent intraspecific facilitation under sub-antarctic conditions,” *American Journal of Botany* **98**(5), pp. 909–914, 2011.
- [135] F. Anthelme, A. Abdoukader, and G. Besnard, “Distribution, shape and clonal growth of the rare endemic tree *olea europaea* subsp.

- laperrinei (oleaceae) in the saharan mountains of niger,” *Plant Ecology* **198**(1), pp. 73–87, 2008.
- [136] C. P. Mulder, “Vertebrate herbivores and plants in the arctic and sub-arctic: effects on individuals, populations, communities and ecosystems,” *Perspectives in Plant Ecology, Evolution and Systematics* **2**(1), pp. 29 – 55, 1999.
- [137] O. H. Inga Hedberg, “Tropical-alpine life-forms of vascular plants,” *Oikos* **33**(2), pp. 297–307, 1979.
- [138] C. Leuschner, “Are high elevations in tropical mountains arid environments for plants?,” *Ecology* **81**(5), pp. 1425–1436, 2000.
- [139] C. Körner, *Alpine plant life: functional plant ecology of high mountain ecosystems; with 47 tables*, Springer Science & Business Media, 2003.
- [140] F. Anthelme and O. Dangles, “Plant-plant interactions in tropical alpine environments,” *Perspectives in Plant Ecology, Evolution and Systematics* **14**(5), pp. 363 – 372, 2012.
- [141] J. A. F. Monteiro and C. Körner, “Leaf turnover and herbivory in the tall tussock grass *festuca orthophylla* in the andean altiplano,” *Alpine Botany* **123**(1), pp. 13–20, 2013.
- [142] P. M. Ramsay and E. R. B. Oxley, “The growth form composition of plant communities in the ecuadorian páramos,” *Plant Ecology* **131**(2), pp. 173–192, 1997.
- [143] L. Gomez-Aparicio, “The role of plant interactions in the restoration of degraded ecosystems: a meta-analysis across life-forms and ecosystems,” *Journal of Ecology* **97**(6), pp. 1202–1214, 2009.
- [144] J. A. F. Monteiro, E. Hiltbrunner, and C. Korner, “Functional morphology and microclimate of *festuca orthophylla*, the dominant tall tussock grass in the andean altiplano,” *Flora - Morphology, Distribution, Functional Ecology of Plants* **206**(4), pp. 387 – 396, 2011.

- [145] H. N. Le Houerou and C. H. Hoste, “Rangeland production and annual rainfall relations in the mediterranean basin and in the african sahelosudanian zone,” *Journal of Range Management* **30**(3), pp. 181–189, 1977.
- [146] J. Monteiro, *Functional morphology and productivity of a grassland in the Bolivian Altiplano*. PhD thesis, PhD thesis, Universität Basel, Basel, Switzerland, 2010.
- [147] A. Zhabotinsky and A. Zaikin, “Autowave processes in a distributed chemical system,” *Journal of Theoretical Biology* **40**(1), pp. 45 – 61, 1973.
- [148] A. T. Winfree, “Spiral waves of chemical activity,” *Science* **175**(4022), pp. 634–636, 1972.
- [149] R. J. Field and R. M. Noyes, “Oscillations in chemical systems. v. quantitative explanation of band migration in the belousov-zhabotinskii reaction,” *Journal of the American Chemical Society* **96**(7), pp. 2001–2006, 1974.
- [150] E. Meron, “Pattern formation in excitable media,” *Physics Reports* **218**(1), pp. 1 – 66, 1992.
- [151] M. Bär, S. Nettesheim, H. H. Rotermund, M. Eiswirth, and G. Ertl, “Transition between fronts and spiral waves in a bistable surface reaction,” *Phys. Rev. Lett.* **74**, pp. 1246–1249, Feb 1995.
- [152] F. Haudin, J. H. E. Cartwright, F. Brau, and A. De Wit, “Spiral precipitation patterns in confined chemical gardens,” *Proceedings of the National Academy of Sciences* **111**(49), pp. 17363–17367, 2014.
- [153] S. Nagano, “Modeling the model organism dictyostelium discoideum,” *Development, Growth & Differentiation* **42**(6), pp. 541–550, 2000.
- [154] G. Bub, L. Glass, N. G. Publicover, and A. Shrier, “Bursting calcium rotors in cultured cardiac myocyte monolayers,” *Proceedings of the National Academy of Sciences* **95**(17), pp. 10283–10287, 1998.

- [155] X. Huang, W. Xu, J. Liang, K. Takagaki, X. Gao, and J. young Wu, "Spiral wave dynamics in neocortex," *Neuron* **68**(5), pp. 978 – 990, 2010.
- [156] K. Wada, "Spiral growth of nacre," *Nature* **211**, p. 1427, 1966.
- [157] A. J. Lotka, "Analytical note on certain rhythmic relations in organic systems," *Proceedings of the National Academy of Sciences* **6**(7), pp. 410–415, 1920.
- [158] V. Volterra, "Variations and fluctuations of the number of individuals in animal species living together," *J. Cons. Int. Explor. Mer* **3**(1), pp. 3–51, 1928.
- [159] Z. E. Rugolo de Agrasar, "The species of the genus *deyeuxia* (poaceae, pooideae) from argentina and nomenclatural notes," *Darwiniana* **44**(1), pp. 131–293, 2006.
- [160] M. C. Garcia, R. I. Meneses, K. Naoki, and F. Anthelme, "Methods to evaluate the effects of domestic herbivores on the vegetation communities of bofedales," *Ecologia en Bolivia* **49**, pp. 91 – 103, 12 2014.
- [161] A. T. Winfree, *The geometry of biological time*, Springer-Verlag, New York, 2nd ed., 2001.
- [162] J. van de Koppel, M. Rietkerk, F. van Langevelde, L. Kumar, C. A. Klausmeier, J. M. Fryxell, J. W. Hearne, J. van Andel, N. de Ridder, A. Skidmore, L. Stroosnijder, and H. H. T. Prins, "Spatial heterogeneity and irreversible vegetation change in semiarid grazing systems," *The American Naturalist* **159**(2), pp. 209–218, 2002.
- [163] S. Kéfi, M. Rietkerk, C. L. Alados, Y. Pueyo, V. P. Papanastasis, A. ElAich, and P. C. De Ruiter, "Spatial vegetation patterns and imminent desertification in mediterranean arid ecosystems," *Nature* **449**(7159), pp. 213–217, 2007.

Chapter 7

Appendix

# Appendix A: Localized plateau beam resulting from strong nonlocal coupling in a cavity filled by metamaterials and liquid-crystal cells

In this appendix we present a published article (M. Tlidi, C. Fernandez-Oto, M. G. Clerc, D. Escaff and P. Kockaert, *Phys. Rev. A* **92**, 053838, 2015) which applies the mechanism based on strong nonlocal coupling to generate structures such as fairy circles and flat spots in the context of nonlinear optics. The references are self-contained in this appendix.

## Abstract

We investigate the formation of localized plateau-beam in the transverse section of a nonlinear optical ring cavity filled with a metamaterial and a nonlocal medium such as a nematic liquid crystal. We show that, far

from the modulational instability regime, localized structures with a varying width may be stable in one and two-dimensional settings. The mechanism of stabilization is related with strong nonlocal coupling mediated by a Lorentzian type of kernel. We show that there exists stable bright and dark localized structures. A reduction of Lugiato-Lefever equation in the regime close to the nascent bistability allows us to analytically derive a simple formula for the width of localized structures in one-dimensional systems. Direct numerical simulations of the dynamical model agree with the analytical predictions.

## I. Introduction

The emergence of localized structures in out-of-equilibrium systems has witnessed tremendous progress in the last two decades, allowing for the design of photonic devices for all-optical control of light, optical storage, and information processing (see recent overviews on this issue in [1–5]). Localized structures usually appear as the result of interactions between optical nonlinearity and other phenomena such as dispersion and diffraction. It is generally sufficient to consider that the nonlinear response is local, *i.e.*, that the material response at a certain point depends only on the value of the electromagnetic field at that point. However, many materials exhibit spatial nonlocality, *i.e.*, the refractive index at a certain point depends not only on the value of the field at that point, but also on the field in the region surrounding this point. The material response is therefore calculated by means of a spatial convolution between the excitation beam and a kernel called "influence function", accounting for the nonlocality.

We classify the kernel functions into two types: weak [6–10] and strong [11–14]. If the kernel function decays asymptotically to infinity slower (faster) than an exponential function, the nonlocal coupling is said to be *strong* (*weak*) [14]. However, our definition of strong nonlocality pertains only to

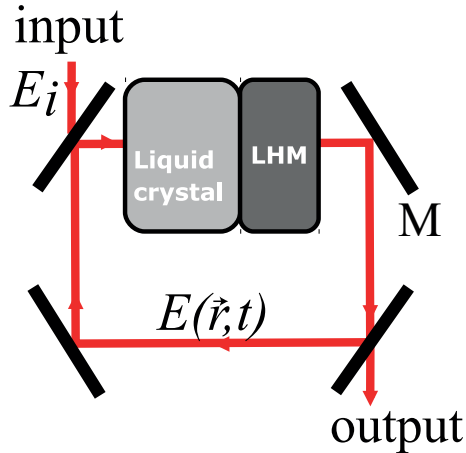


Figure 7.1: Ring resonator filled with a left-handed material (LHM) and a nonlocal medium such a liquid crystal.  $M$  accounts for the mirrors.

the material properties, it differs from the usual one [15] that takes into account both the material response and the beam diameter, stating that the nonlocal coupling is strong if the width of the kernel functions is large in comparison with the beam diameter. Several experimental measurements of a strong nonlocal response of the material with a Lorentzian or a generalized Lorentzian shape have been carried out in nematic liquid crystal (NLC) cells [16, 17]. The NLC response was best fitted with a pseudo-Lorentzian function, which corresponds also to a strong nonlocal coupling. Experimental reconstruction of strong nonlocal coupling has been performed in photorefractive materials [18].

In a different subfield of optics, left-handed materials (LHMs) are metamaterials that present a negative permittivity and permeability [19, 20]. They have been first demonstrated at microwave frequencies [21, 22], and soon after in the optical domain [23, 24]. Metamaterials are shown to exhibit novel electromagnetic phenomena such as imaging [25, 26] or negative diffraction, and can be used in nonlinear optical devices [3, 27–30]. In particular, the

formation of both conservative and dissipative solitons in a Kerr resonator containing a LHM has been studied in [29, 31–37].

In this paper, we consider a ring resonator filled with two materials having indices of refraction of opposite signs (see Fig. 7.1). The first material exhibits a strong nonlocal coupling mediated by a Lorentzian, while the second material consists in a linear material with a negative diffraction coefficient. We focus on the bistable regime far from any modulational or Turing type of instabilities. We analyze the interaction of fronts connecting the two stable homogeneous steady states and we investigate the impact of strong nonlocal coupling on front propagation in the system. A front is an heteroclinic connection between homogeneous steady states [38, 39]. Generally, the fronts are propagating, which means that they are moving and interacting.

When the nonlocal coupling is weak, the interaction of fronts is usually described by the behavior of the tail of one front around the core of the other front [6, 7]. However, for strong nonlocal coupling, the interaction is controlled by the whole influence function and not only by the asymptotic behavior of the front tails. Recently, we have reported that strong nonlocal interaction is responsible for a new mechanism to stabilize a single localized structure [11–13]. We showed that strong nonlocal coupling drastically alters the space-time behavior of spatially extended systems by affecting the asymptotic behavior of a single front and by modifying the law governing front interactions. We also demonstrated the occurrence of stable localized structures with varying plateau size. In the current context, the mechanism of stabilization is attributed to combined influence of the strong nonlocal coupling in the nematic liquid crystal, negative diffraction in the metamaterial and bistability induced by the presence of an optical resonator.

The paper is organized as follows. After introducing the model (Sec. II), we perform numerical simulations of the full model (Sec. III). A reduction of the equation in the nascent bistability regime, which allows us to analytically describe the fronts interaction, is presented in Sec. IV. We conclude in Sec. V.

## II. The Lugiato-Lefever model with nonlocal coupling

The ring resonator filled with a material presenting nonlocal nonlinearity (NLNL) and a negative diffraction (ND) material is described by the well known Lugiato-Lefever model [40], in which we incorporate the strong nonlocal effect. This model equation is valid under the following approximations: (i) at the interface separating the NLNL and the ND materials, the reflection is assumed to be negligible, *i.e.*, they are impedance matched; (ii) the cavity possess a high Fresnel number *i.e.*, large-aspect-ratio system and we assume that the cavity is much shorter than the diffraction and the nonlinearity spatial scales; (iii) for the sake of simplicity, we assume a single longitudinal mode operation. Under these assumptions the space-time evolution of the intracavity field is described by the following partial differential equation

$$\begin{aligned} \partial_t E = E_i & - (1 + i\theta)E + i|E|^2 E + iD\nabla^2 E \\ & - i\gamma \int_{\Omega} E(\mathbf{r} + \mathbf{r}', t) K(\mathbf{r}') d\mathbf{r}', \end{aligned} \quad (7.1)$$

The normalized slowly varying complex envelope of the electric field is  $E$ . The input field amplitude  $E_i$  is real and constant. The detuning parameter is given by  $\theta$ . The diffraction coefficient is  $D$ , and  $\Omega$  is the domain under study. In the absence of nonlocal coupling in the liquid crystal cell, *i.e.*,  $\gamma = 0$ , we recover the well known Lugiato-Lefever model [40]. The inclusion of LHM slice allows to explore the parameter regime where diffraction is negative [31]. From a practical point of view, negative diffraction could be achieved by using a self-imaging configuration [41–43]. In the absence of nonlocal interaction, the stabilization of localized solutions far from any pattern-forming instability has been realized thanks to the combined action of a negative diffraction and an inhomogeneous pumping laser beam [43]. The laser cavity can be also considered as an inhomogeneous cavity in the

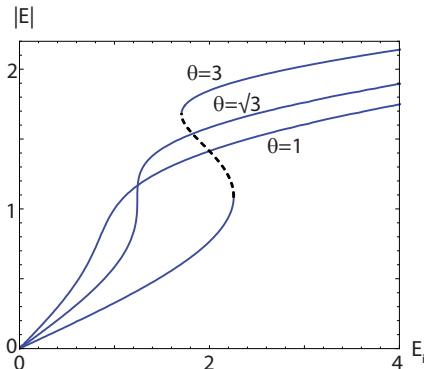


Figure 7.2: Homogeneous steady states solutions of Eq. (7.1) for different values of the detuning parameter  $\theta$ . The continuous and dashed curves indicate stable and unstable states, respectively.

work by Zhang [44, 45]. Finally the nonlocal coupling is modeled by the function  $K(\mathbf{r}')$

$$K(\mathbf{r}') = \delta(\mathbf{r}') - f_\sigma(\mathbf{r}'), \quad (7.2)$$

where  $\delta(\mathbf{r}')$  is the delta distribution and the kernel function  $f_\sigma(\mathbf{r}')$  is defined by

$$f_\sigma(\mathbf{r}) = \frac{N_n}{1 + (|\mathbf{r}|/\sigma)^n}. \quad (7.3)$$

The parameter  $\gamma$  measures the intensity of the nonlocal interaction,  $\sigma$  represent the characteristic length of the nonlocal interaction, and  $N_n$  is a normalization constant. Such a nonlocal response can be realized in a liquid crystal cell. particular, experimental measurements [16] show that the nonlocal variation of the refractive index in cells filled with the commercially available E7 liquid crystal is well fitted with a Lorentzian. In this experiment, the thickness of the cell was varied in the range 18-73  $\mu\text{m}$ . Another group of researchers reported on slightly different results using pulsed beams [17]. The nonlocal response of the material was deduced from the

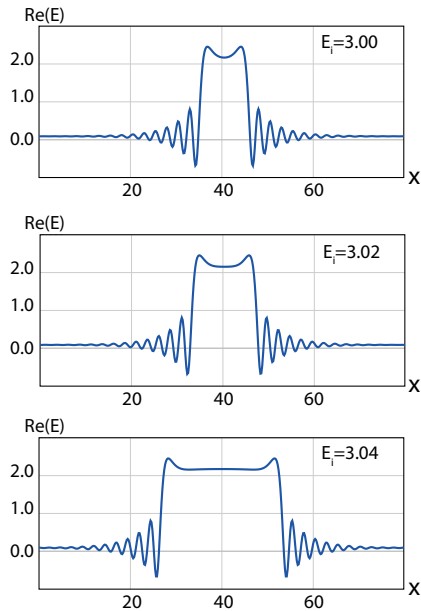


Figure 7.3: Localized plateau-beam in one transverse dimension. Three different structures in one dimension, for three different values of injection  $E_i$ . The parameters are  $\theta = 6.0$ ,  $D = -1.0$ ,  $\gamma = 1.0$ ,  $\sigma = 0.7$  and  $n = 2.0$ .

interaction of soliton beams in a liquid crystal cell. This response was best fitted with a pseudo-Lorentzian function, which corresponds also to a strong nonlocal coupling, as defined here above. Experimental evidence of strong nonlocal coupling has also been performed in photorefractive materials [18], where the strong nonlocal coupling is originating from thermal effects.

The homogeneous steady states of Eq. (7.1) are solutions of  $E_i = [1 + i(\theta - |E_s|^2)]E_s$ . The response curve giving the intracavity intensity  $|E_s|^2$  as a function of the input intensity  $|E_i|^2$  is monostable for  $\theta < \sqrt{3}$  and exhibits a bistable behavior when the detuning  $\theta > \sqrt{3}$  (see Fig. 7.2).

### III. Localized plateau-beam: numerical simulations

Our numerical simulations are focused on the parameter range corresponding to bistability of the homogeneous steady-state solutions, *i.e.*,  $\theta > \sqrt{3}$  and we consider a regime where these states are modulationally stable far from any modulational or Turing instability. The later condition is achieved when the effective diffraction of the cavity is negative ( $D < 0$ ).

Numerical simulations generate stable one-dimensional localized structures, as shown in Fig. 7.3. From these plots, we can see that the width of the obtained localized structures vary strongly with the injected beam intensity. In addition these structures possess a plateau and the background exhibits spatial damped oscillations. The stabilization mechanism is robust in two dimensional setting. An example of 2D localized structures with a varying size plateau is shown in Fig. 7.4. As one-dimensional setting, these structures exhibit damped oscillations in the profile of the intracavity intensity. The circular flat area varies strongly with a small change of the injected beam intensity as shown in Fig. 7.4.

Localized structures have been predicted in one dimensional bistable optical systems with a gaussian beam [46–48]. These solutions were interpreted as switching waves connecting two stable branches of the homogeneous response curve. It has been shown later that LS's do not require a commutation process between distinct uniform stationary states [49, 51]. Two-dimensional LS's can be stable in the monostable regime where a single homogeneous steady state coexists with periodic structures such as hexagons and stripes [49–51]. In bistable regime, the physical systems exhibit the existence of a hysteresis loop. Within it, there generally exists a so-called pinning range of parameter values for which stable localized structures, connecting the uniform and the periodic solutions, can be found. The existence of a pinning range was predicted by Pomeau [52] and observed experimentally in a liquid crystal light valve with optical feedback [53]. The formation of LS's in Turing regime is common in a variety of systems such as reaction-diffusion [54–56], hydrodynamics [57–63] photorefractives [64],

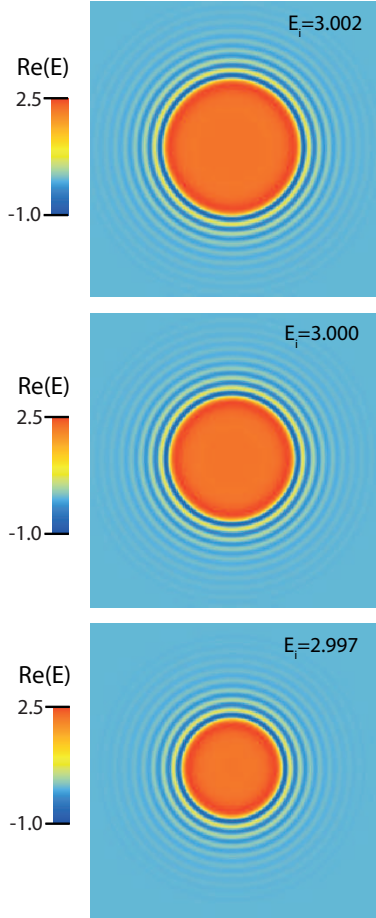


Figure 7.4: Localized plateau-beam in two-dimensions. Three different structures in two dimension, for three different values of injection  $E_i$ . The parameters are  $\theta = 5.93$ ,  $D = -1.0$ ,  $\gamma = 1.0$ ,  $\sigma = 0.4$  and  $n = 2.2$ .

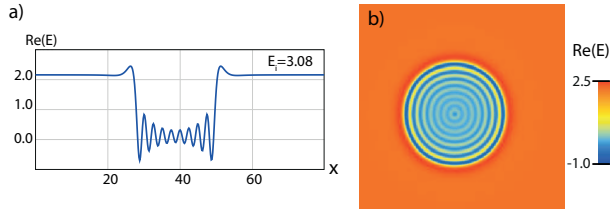


Figure 7.5: Holes FCs in one and two dimensions. In a) the parameters are  $\theta = 6.0$ ,  $D = -1.0$ ,  $\gamma = 1.0$ ,  $\sigma = 0.7$ ,  $n = 2.0$ , and  $E_i = 3.08$ . In b) the parameters are  $\theta = 5.93$ ,  $D = -1.0$ ,  $\gamma = 1.0$ ,  $\sigma = 0.4$ ,  $n = 2.2$  and  $E_i = 3.034$ .

Ginzburg-Landau equation [65,66], liquid crystals [50,71–74], and semiconductors [67,68,70]. The bifurcation that leads to the formation of LS’s is referred to as homoclinic snaking phenomenon [75–81]. The relative stability of 1D and 2D-clusters of closely packed localized peaks of the Swift-Hohenberg equation has been analyzed [82].

Localized plateau-beam reported here are obtained in regime devoid from any pattern forming type of instability. They differs from the above mentioned LS in three ways. First, localized plateau-beam cannot be stable in the monostable regime. Bistability is the prerequisite condition for their stabilization. Second, localized structures found in the subcritical Turing regime have a fixed width. Their width does not significantly change as a function of the injected beam intensity. Their width is determine by the most unstable wavelength. However, in our case the width of LS’s vary strongly with the injected beam intensity. Third, our LS’s connect two homogeneous steady states while the LS’s found in the Turing regime connect one homogeneous steady to a periodic pattern.

In the absence of strong nonlocal coupling ( $\gamma = 0$ ), the model Eq. (7.1) does not admit stable bright localized structures with varying plateau size. The inclusion of strong nonlocal coupling allows for the stabilization of these localized states in one and in two transverse directions as shows in Figs. 7.3

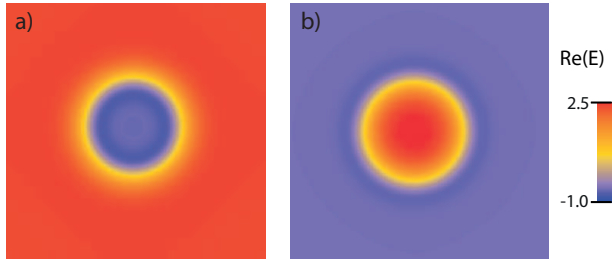


Figure 7.6: (a) dark and (b) bright localized structures in two dimensions obtained by numerical simulations of Eq. (7.1). The parameters are  $\theta = 1.8$ ,  $D = -1.0$ ,  $\gamma = 0.3$ ,  $\sigma = 0.4$ , and  $n = 2.2$ . The injection field amplitude is a)  $E_i = 1.278$  and (b)  $E_i = 1.275$ .

and 7.4. In addition, dark localized structures may be stabilized by the fact that the lower uniform exhibits damped oscillations near to the front core. In Fig. 7.5 we can see the combination of both effects, strong nonlocal coupling and damped oscillations, stabilizing dark localized structures in one and in two-dimensions as shown in Fig.7.5a and in Fig.7.5b. The damped oscillations appear for large detuning parameter. However, close to nascent optical bistability ( $\theta - \sqrt{3} \ll 1$ ), numerical simulations of the model Eq. (7.1) show that both dark and bright localized structures are devoid of damped oscillations (see Fig. 7.6).

In the next section we will perform a perturbative calculation near onset of bistability, which allows us to describe analytically the formation of localized structures with varying plateau size in one-dimension.

## IV. Localized plateau-beams: Analytical analysis

The analytical investigation of fronts dynamics connecting two-homogeneous steady states in the framework of Eq. (7.1) is a complex problem. In this section we perform a reduction of Eq. (7.1) to a simple bistable model with

nonlocal interaction. This reduction is valid close to the onset of optical bistability. At the critical point where the output versus input characteristics have an infinite slope, the critical detuning is  $\theta = \theta_c \equiv \sqrt{3}$ . In order to study the front dynamics, we explore the vicinity of the critical point associated with bistability. At the critical point, the coordinate of the intracavity are  $E_c = u_c + iv_c$  with  $u_c = 3^{1/4}/\sqrt{2}$  and  $v_c = -1/3^{1/4}\sqrt{2}$ , and the injected field amplitude is  $E_{ic} = 2\sqrt{2}/3^{3/4}$ . To derive a simple bistable model with nonlocal interaction, we introduce a small parameter  $\epsilon$  which measures the distance from the critical point as  $\theta = \theta_c + \theta_0\epsilon^2$ . Then we decompose the field into its real and imaginary parts as  $E = u + iv$  and introduce the excess variables  $U$ ; and  $V$  as  $u = u_c + U$  and  $v = v_c + V$ . We next expand the  $U$ ,  $V$ , and  $E_i$  in power series of  $\epsilon$  as

$$\begin{aligned} U &= \epsilon\sqrt{3\theta_0}C/2 - \epsilon^2\theta_0 \left[ 3^{3/4}C^2/\sqrt{2} - \sqrt{3}u_c/2 \right] + \dots, \\ V &= \epsilon\sqrt{\theta_0}C/2 + \dots, \\ E_i &= E_c - \epsilon^2\theta_0v_c + \epsilon^3\eta\theta_0^{3/2}/2 + \dots, \end{aligned}$$

where  $C(x_0, T)$  is an order parameter that describes the optical instability, and  $T \equiv \epsilon^2\theta_0/\sqrt{3}$ , and  $x_0 \equiv \epsilon x\sqrt{-\theta_0/D}$  rescale time and space, respectively. The intensity of the nonlocal coupling scale as  $\gamma \equiv \theta_0\epsilon^2\gamma_0$ . The application of the solvability condition at the third order in  $\epsilon$  leads to a simple bistable model with a nonlocal coupling

$$\begin{aligned} \partial_T C = \eta &+ C - C^3 + \partial_{x_0x_0} C \\ &+ \gamma_0 \int_{-\infty}^{\infty} C(x_0 + x'_0, t) K(x'_0) dx'_0. \end{aligned} \quad (7.4)$$

In the absence of the nonlocal coupling, i.e.,  $\gamma_0 = 0$ , we recover a bistable model [43]. In the expansion of the injected field appears an extra parameter  $\eta$ , which account for the deviation to the Maxwell point. The Maxwell point is obtained when the front velocity vanishes. This point corresponds to  $\eta = 0$ .

In what follows we derive an equation for the time evolution of the width of localized structures. Then we seek for the stationary width as a func-

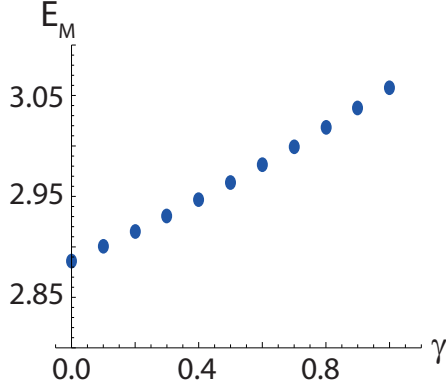


Figure 7.7: Numerical value for the Maxwell point as function of the nonlocal intensity  $\gamma$ . The parameters are  $\theta = 6.0$ ,  $D = -1.0$ ,  $\sigma = 0.7$  and  $n = 2.0$ .

tion of the system parameters. For this purpose we shall restrict our analysis to the case of one transverse dimensional. The two-dimensional case is far from the scope of the present paper. Close to the Maxwell point, one can consider the following ansatz for the localized structure  $C(x_0, T) = \tanh \left[ (x_0 + \Delta_0(T))/\sqrt{2} \right] - \tanh \left[ (x_0 - \Delta_0(T))/\sqrt{2} \right] - 1 + \delta C$ , where  $2\Delta_0$  stands for the width of localized structure and  $\delta C$  accounts for small corrections. To get the front dynamic, we introduce the above ansatz for  $C$  in Eq. (7.4), linearizing in  $\delta C$  and imposing the solvability condition, we obtain for  $n = 2$

$$\partial_T \Delta_0 = \frac{3\eta}{\sqrt{2}} + \frac{3\gamma_0 \sigma \epsilon \sqrt{\theta_0}}{\sqrt{2}\pi \Delta_0}. \quad (7.5)$$

Then, the equilibrium size is give by

$$\Delta_0^{eq} = \frac{-\gamma_0 \sigma \epsilon \sqrt{\theta_0}}{\pi \eta}. \quad (7.6)$$

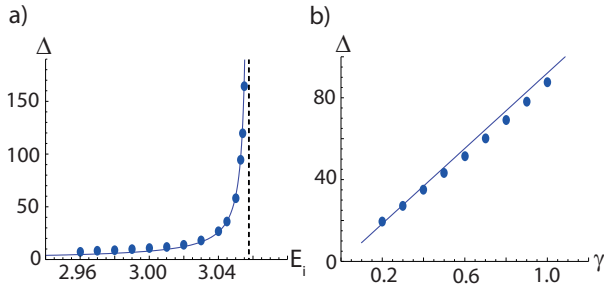


Figure 7.8: Theoretical and numerical size of localized plateau-beam in one-dimension. The solid line is the theoretical prediction from Eq. (7.7), the dots are the numerical results from Eq. (7.1) and the dashed line in a) corresponds to the Maxwell point estimated numerically. In both graphics, the parameters are  $\theta = 6.0$ ,  $D = -1.0$ ,  $\sigma = 0.7$  and  $n = 2.0$ . In a), the nonlocal intensity  $\gamma = 1.0$ . In b), the distance to the maxwell point  $E_M - E_i = 0.005$ .

In terms of the original parameters, the width of the structure is

$$\Delta^{eq} = \frac{-\gamma\sigma\sqrt{\theta - \theta_c}}{\pi(E_i - E_M)}, \quad (7.7)$$

where  $E_M$  is the value of the Maxwell point with the nonlocal coupling intensity  $\gamma$  and the interaction range  $\sigma$ .

The formula Eq. (7.7) is valid close to the nascent optical bistability ( $\theta - \sqrt{3} \ll 1$ ). This prediction is in perfect agreement with numerical simulations. In order to check the robustness of the proposed stabilization mechanism, we perform the analysis far from the onset of bistability by fixing the detuning parameter to  $\theta = 6$ . In this case, the Maxwell point value ( $E_M$ ) depends strongly on the intensity of the nonlocal coupling  $\gamma$  and the interaction range  $\sigma$  as shown in Fig. 7.7. The comparison between the stationary size of localized structure obtained from the formula Eq. (7.7) fits quite well

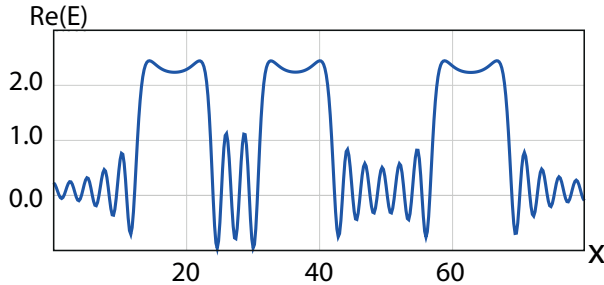


Figure 7.9: Interaction between three localized plateau-beams in one transverse dimension. The parameters are  $\theta = 6.0$ ,  $D = -1.0$ ,  $\gamma = 0.5$ ,  $\sigma = 0.7$ ,  $E_i = 2.94$  and  $n = 2.0$ .

with the results of numerical simulations without any other adjustment parameter. The comparison is shown in Fig. 7.8. These plots show that our analytical investigation is still valid beyond the nascent optical bistability. The width of localized structure increases with the distance to the Maxwell point and with the intensity of the strong nonlocal coupling. At the Maxwell point, the width of localized structure diverges at the Maxwell point as shown in Fig. 7.8a. While the width of localized structure depends linearly on the nonlocal intensity  $\gamma$  as shown in Fig. 7.8b. Numerical results are in good agreement with the theoretical predictions.

The presence of well-pronounced oscillatory tails suggests a possibility to form robust bound complexes of two or several localized plateau-beam. An example of three localized beam bounded together is shown in the Fig. 7.9. When the distance between peaks decreases they start to interact via their oscillating, exponentially decaying tails. This interaction then leads to the formation of clusters [83–88].

To address the problem experimental feasibility of localized plateau-beam, we need to work with a stabilized, and slightly detuned, nonlinear and spatially extended optical cavity, with strong nonlocal coupling and with a layer of left-handed material. The nonlocal nonlinear material that we

target is a liquid crystal cell filled with a standard E7 liquid crystal, and used in a geometry similar to that of Ref. [16]. Such a cell is strongly nonlocal, according to the experimental characterization reported in Ref. [16]. It presents also high nonlinearity that allows to perform the experiment with reasonable optical power. We need a pump beam that allows to reach the input intensity at which the system switches to the higher homogeneous steady state. To keep a sufficient power margin, we will work with a green cw laser delivering up to 15 W at a wavelength of 532 nm. The control of the detuning is a key issue. For this purpose, we will make use of an internally-developed proportional-integral controller based on a microchip device. Once the stabilization setup is working with a beam polarized in one direction, the observation of the plateau solutions will be performed with a beam polarized orthogonally to the control beam as follows. Firstly, for a given detuning, we will record the input-output characteristic of the setup. For a sufficiently large detuning, we should observe bistability. The hysteresis curve will allow to determine the input power corresponding to the Maxwell point. Working at this power, and fixing the detuning, we will induce the spatial structure by means of an additional seed that will be combined with the main beam outside the cavity. The pump beam will be split by a polarizing beam splitter followed on each arm by a different telescope, and by a half-wave plate on the second arm. The two arms will then be recombined on a non polarizing beam splitter in a Mach-Zehnder configuration. The relative width between the main beam and the seed beam will be fixed by the parameters of the two telescopes, while their relative intensity will be determined by the orientation of the wave plates. The output of the cavity will be recorded on a camera. This will allow to study the evolution of the plateau solution when varying the different control parameters (pump power, detuning, nonlinearity by application of a voltage on the liquid crystal cell).

## V. Conclusions

We have considered a ring cavity filled by a combination of a nonlocal medium and a left-handed material. This cavity is driven by a coherent injected signal. We have investigated the formation of localized structures in a bistable regime where both homogeneous steady states are modulationally stable. To avoid modulational or Turing instability, we have used left-handed element that allows the system operating in a negative diffraction regime. The response of left-handed material is considered linear, and the nonlinearity of Kerr type is originated from nonlocal medium such as a nematic liquid crystals cells. We have presented a mechanism of generation of stable localized structures based on strong nonlocal coupling mediated by a Lorentzian-like kernel. This type of nonlocal coupling has been reported experimentally in the case of nematic crystals cells [16, 17]. This nonlocal coupling modifies the nature of front interaction between two homogeneous steady states, and allows for the stabilization of both bright and dark localized structures. These structures have a varying plateau size. Without strong nonlocal coupling localized structures are unstable. They either shrink or expand. An analytical expression of the front interaction law is provided in the regime close to the critical point associated with bistability. Close to this point we have reduced the LL Eq. (7.1) to a simple bistable model equation with nonlocal interaction. The variation of the width of localized structures has been derived in one dimensional system in the framework of the reduced equation. This generic mechanism is robust in one and two spatial dimensions and could be applied to a large class of far from equilibrium systems with strong nonlocal coupling. Finally, we discuss the experimental feasibility of localized plateau-beam.

## Acknowledgments

M.G.C. acknowledges the financial support of FONDECYT project 1150507. D.E. acknowledges the financial support of FONDECYT project N 1140128.

C.F.-O. acknowledges financial support of Becas Chile. M.T. received support from the Fonds National de la Recherche Scientifique (Belgium) and the Interuniversity Attraction Poles program Photonics@be of the Belgian Science Policy Office (BelSPO), under Grant IAP 7-35.

# Bibliography

- [1] H. Leblond and D. Mihalache, *Physics Reports*, **523**, 61 (2013).
- [2] M. Tlidi, K. Staliunas, K. Panajotov, A.G. Vladimirov, and M. Clerc, *Phil. Trans. R. Soc. A*, **372**, 20140101 (2014).
- [3] M. Lapine, I.V. Shadrivov, and Y.S. Kivshar, Colloquium: Nonlinear metamaterials, *Rev. Mod. Phys.* **86**, 1093 (2014).
- [4] L. Lugiato, F. Prati, and M. Brambilla, *Nonlinear Optical Systems*, (Cambridge University Press, 2015).
- [5] O. Descalzi, M. Clerc, S. Residori, and G. Assanto (eds.), *Localized States in Physics: Solitons and Patterns* (Springer, Berlin, 2010).
- [6] M. G. Clerc, D. Escaff, and V. M. Kenkre, *Phys. Rev. E* **72**, 056217 (2005).
- [7] M. G. Clerc, D. Escaff, and V. M. Kenkre, *Phys. Rev. E* **82**, 036210 (2010).
- [8] L. Gelens, D. Gomila, G. Van der Sande, M.A. Matías, and P. Colet, *Phys. Rev. Lett.* **104**, 154101 (2010).
- [9] P. Colet, M.A. Matías, L. Gelens, and D. Gomila, *Phys. Rev. E* **89**, 012914 (2014).

- [10] L. Gelens, M.A. Matias, D. Gomila, T. Dorissen, and P. Colet, *Phys. Rev. E* **89**, 012915 (2014).
- [11] C. Fernandez-Oto, M.G. Clerc, D. Escaff, and M. Tlidi, *Phys. Rev. Lett.* **110**, 174101 (2013).
- [12] C. Fernandez-Oto, M. Tlidi, D. Escaff, and M.G. Clerc, *Phil. Trans. R. Soc. A* **372**, 20140009 (2014).
- [13] D. Escaff, C. Fernandez-Oto, M.G. Clerc, and M. Tlidi, *Phys. Rev. E* **91**, 022924 (2015).
- [14] D. Escaff, *Eur. Phys. J. D* **62**, 33 (2011).
- [15] W. Krolikowski and O. Bang, *Phys. Rev. E* **63**, 016610 (2000).
- [16] X. Hutsebaut, C. Cambournac, M. Haelterman, J. Beeckman, and K. Neyts, *JOSA B* **22**, 1424 (2005)
- [17] J.F. Henninot, J.F. Blach, and M. Warenghem, *J. Opt. A* **9**, 20 (2007).
- [18] A. Minovich, D.N. Neshev, A. Dreischuh, W. Krolikowski, and Y.S. Kivshar, *Opt. Lett.* **32**, 1599 (2007).
- [19] V. G. Veselago, *Sov. Phys. Usp.* **10**, 509 (1968).
- [20] J. B. Pendry, *Phys. Rev. Lett.* **85**, 3966 (2000).
- [21] R. A. Shelby, D.R. Smith, and S. Schultz, *Science* **292**, 77 (2001).
- [22] K. Aydin, K. Guven, M. Kafesaki, L. Zhang, C.M. Soukoulis, and E. Ozbay, *Opt. Lett.* **29**, 2623 (2004).
- [23] C. Enkrich, M. Wegener, S. Linden, S. Burger, L. Zschiedrich, F. Schmidt, J.F. Zhou, T. Koschny, and C.M. Soukoulis, *Phys. Rev. Lett.* **95**, 203901 (2005).
- [24] T.F. Gundogdu, I. Tsiapa, A. Kostopoulos, G. Konstantinidis, N. Katsarakis, R.S. Penciu, M. Kafesaki, E.N. Economou, T. Koschny, and C.M. Soukoulis, *Appl. Phys. Lett.* **89**, 084103 (2006).

- [25] D.R. Smith, J.B. Pendry, and M.C.K. Wiltshire, *Science* **305**, 788 (2004).
- [26] M.W. Feise, I.V. Shadrivov, and Y.S. Kivshar, *Phys. Rev. E* **71**, 037602 (2005).
- [27] A.A. Zharov, N. A. Zharova, I.V. Shadrivov, and Y.S. Kivshar, *Appl. Phys. Lett.* **87**, 091104 (2005).
- [28] N. Lazarides and G. P. Tsironis, *Phys. Rev. E* **71**, 036614 (2005).
- [29] G. D'Aguanno, N. Mattiucci, M. Scalora, and M.J. Bloemer, *Phys. Rev. Lett.* **93**, 213902 (2004).
- [30] M. Scalora, M. S. Syrchin, N. Akozbek, E. Y. Poliakov, G. D'Aguanno, N. Mattiucci, M. J. Bloemer, and A.M. Zheltikov, *Phys. Rev. Lett.* **95**, 013902 (2005).
- [31] P. Kockaert, P. Tassin, G. Van der Sande, I. Veretennicoff, and M. Tlidi, *Phys. Rev. A* **74**, 033822 (2006).
- [32] P. Tassin, G. Van der Sande, N. Veretenov, P. Kockaert, I. Veretennicoff, and M. Tlidi, *Opt. Express*, **14**, 9338 (2006).
- [33] P. Tassin, L. Gelens, J. Danckaert, I. Veretennicoff, G. Van der Sande, P. Kockaert, and M. Tlidi, *Chaos* **17**, 037116 (2007).
- [34] L. Gelens, G. Van der Sande, P. Tassin, M. Tlidi, P. Kockaert, D. Gomila, I. Veretennicoff, and J. Danckaert, *Phys. Rev. A* **75**, 063812 (2007).
- [35] A.D. Boardman, N. King, R.C. Mitchell-Thomas, V.N. Malnev, and Y.G. Rapoport, *Metamaterials* **2**, 145 (2008).
- [36] A.B. Kozyrev, I.V. Shadrivov, and Y.S. Kivshar, *Applied Physics Letters*, **104**, 084105 (2014).

- [37] A.D. Boardman, K.L. Tsakmakidis, R.C. Mitchell-Thomas, N.J. King, Y.G. Rapoport, and O. Hess, Springer Series in Materials Science, **200**, 161 (2015).
- [38] M.C. Cross and P.C. Hohenberg, Rev. Mod. Phys. **65**, 851 (1993).
- [39] W. van Saarloos, Physics reports, **386**, 29 (2003).
- [40] L.A. Lugiato and R. Lefever, Phys. Rev. Lett. **58**, 2209 (1987).
- [41] J. A. Arnaud, Appl. Opt. **8**, 189 (1969).
- [42] P. Kockaert, JOSA B, **26**, 1994 (2009).
- [43] V. Odent, M. Tlidi, M. G. Clerc, P. Glorieux, and E. Louvergneaux, Phys. Rev. A **90**, 011806(R) (2014).
- [44] H. Zhang, D. Y. Tang, L.M. Zhao and X. Wu, Phys. Rev. B **80**, 052302 (2009).
- [45] H. Zhang, D. Y. Tang, L. Zhao, and X. Wu, Opt. Express **19**, 3525 (2011).
- [46] J.V. Moloney and H.M. Gibbs, Phys. Rev. Lett. **48**, 1607 (1982).
- [47] D. W. Mc Laughlin, J.V. Moloney, and A.C. Newell, Phys. Rev. Lett. **51**, 75 (1983).
- [48] N. Rosanov and G. Khodova, Opt. Spektrosk., **65**, 1375 (1988).
- [49] A.J. Scroggie et al., Chaos, Solitons and Fractals **4**, 1323 (1994).
- [50] U. Bortolozzo, M.G. Clerc, and S. Residori, New J. Phys. **11**, 093037 (2009).
- [51] M. Tlidi, P. Mandel, and R. Lefever, Phys. Rev. Lett. **73**, 640 (1994).
- [52] Y. Pomeau, Physica D **23**, 3 (1986).

- [53] F. Haudin, R.G. Elias, R.G. Rojas, U. Bortolozzo, M.G. Clerc, and S. Residori, *Phys. Rev. Lett.* **103**, 128003 (2009).
- [54] S. Koga and Y. Kuramoto, *Prog. Theor. Phys.* **63** , 106 (1980)
- [55] P.B. Umbanhowar, F. Melo, and H.L. Swinney, *Nature* **382**, 793 (1996).
- [56] M.G. Clerc, E. Tirapegui, and M. Trejo, *Phys. Rev. Lett.* **97**, 176102 (2006).
- [57] P. Kolodner, D. Bensimon, and C. M. Surko, *Phys. Rev. Lett.* **60**, 1723 (1988).
- [58] O. Thual, and S. Fauve, *J. Phys. France* **49**, 1829 (1988).
- [59] W. Barten, M. Lücke, and M. Kamps, *Phys. Rev. Lett.* **66**, 2621 (1991).
- [60] M. Dennin, G. Ahlers, and D. S. Cannell, *Science* **272**, 388 (1996).
- [61] H. Riecke, *Phys. Rev. Lett.* **68**, 301 (1992).
- [62] H. Riecke and G. D. Granzow, *Phys. Rev. Lett.* **81**, 333 (1998).
- [63] C. Crawford and H. Riecke, *Physica D: Nonlinear Phenomena*, **129**, 83 (1999).
- [64] A.A. Zozulya, M. Saffman, and D.Z. Anderson, *Phys. Rev. Lett.* **73**, 818 (1994).
- [65] B. A. Malomed and A.A. Nepomnyashchy, *Phys. Rev. A* **42**, 6009 (1990).
- [66] V. Skarka, N.B. Aleksic, M. Lekic, B.N. Aleksic, B.A. Malomed, D. Mihalache, and H. Leblond, *Phys. Rev. A* **90**, 023845 (2014).
- [67] V.B. Taranenko, K. Staliunas, and C.O. Weiss, *Phys. Rev. A* **56**, 1582 (1997).
- [68] V.B. Taranenko, K. Staliunas, and C. O. Weiss, *Phys. Rev. Lett.* **81**, 2236 (1998).

- [69] X. Hachair, F. Pedaci, E. Caboche, S. Barland, M. Giudici, J.R. Tredicce, F. Prati, G. Tissoni, R. Kheradmand, L.A. Lugiato, I. Prot-senko, and M. Brambilla, Selected Topics in Quantum Electronics, IEEE Journal of **12**, 339 (2006).
- [70] E. Averlant, M. Tlidi, H. Thienpont, T. Ackemann, K. Panajotov, Opt. Express **22**, 762 (2014).
- [71] P. L. Ramazza, S. Ducci, S. Boccaletti, and F. T. Arecchi, J. Opt. B, **2**, 399 (2000).
- [72] U. Bortolozzo, L. Pastur, P. L. Ramazza, M. Tlidi, and G. Kozyreff, Phys. Rev. Lett. **93**, 253901 (2004).
- [73] U. Bortolozzo, M. G. Clerc, C. Falcon, S. Residori, and R. Rojas, Phys. Rev. Lett. **96**, 214501 (2006).
- [74] V. Odent, M. Taki, and E. Louvergneaux, New J. Phys. **13**, 113026 (2011).
- [75] A.R. Campneys, Physica D **112**, 158 (1998).
- [76] Y. Nishiura and D. Ueyama, Physica D **130**, 73 (1999).
- [77] P. Couillet, C. Riera, and C. Tresser, Phys. Rev. Lett. **84**, 3069 (2000).
- [78] M.G. Clerc, C. Falcon, and E. Tirapegui, Phys. Rev. Lett. **94**, 148302 (2005).
- [79] M. Tlidi and L. Gelens, Opt. Lett. **35**, 306 (2010).
- [80] M. Tlidi, P. Kockaert, and L. Gelens, Phys. Rev. A **84**, 013807 (2011).
- [81] F. Haudin, R. G. Rojas, U. Bortolozzo, S. Residori, and M.G. Clerc, Phys. Rev. Lett. **107**, 264101 (2011).
- [82] A.G. Vladimirov, R. Lefever, and M. Tlidi, Phys. Rev. A **84**, 043848 (2011).

- [83] K.A. Gorshkov and L.A. Ostrovsky, *Physica D*, **3**, 428 (1981).
- [84] I.S. Aranson, K.A. Gorshkov, A.S. Lomov, and M.I. Rabinovich, *Physica D: Nonlinear Phenomena*, **43**, 435 (1990).
- [85] Boris A. Malomed, *Phys. Rev. A* **44**, 6954 (1991).
- [86] A.G. Vladimirov, J.M. McSloy, D.V. Skryabin, and W.J. Firth *Phys. Rev. E* **65**, 046606 (2002).
- [87] M. Tlidi, A. G. Vladimirov, and P. Mandel, *IEEE Journal of Quantum Electronics* **39**, 216 (2003).
- [88] M. Tlidi, R. Lefever, and A. Vladimirov, *Lect. Notes. Phys.* **751**, 381 (2008).

# Appendix B: List of publications

Publications in international journals

1. M.G. Clerc, C. Falcon, C. Fernandez-Oto and E. Tirapegui, EPL **98**, 30006 (2012). “Effective-parametric resonance in a non-oscillating system”
2. M. G. Clerc, C. Fernandez-Oto, M. A. García-Ñustes, and E. Louvergneaux, Phys. Rev. Lett. **109**, 104101 (2012). “Origin of the Pinning of Drifting Monostable Patterns”
3. M. G. Clerc, C. Fernández-Oto, and S. Coulibaly. Phys. Rev. E **87**, 012901 (2013). ”Pinning-depinning transition of fronts between standing waves”.
4. C. Fernandez-Oto, M.G. Clerc, D. Escaff, and M. Tlidi, Phys. Rev. Lett., **110**, 174101 (2013). “Strong non-local coupling stabilizes localized structures: An analysis based on front dynamics”.
5. C. Fernandez-Oto, G. J. de Valcárcel, M. Tlidi, K. Panajotov, and K. Staliunas. Phys. Rev. A **89**, 055802 (2014). “Phase-bistable patterns and cavity solitons induced by spatially periodic injection into vertical-cavity surface-emitting lasers”.

6. C. Fernandez-Oto, M. Tlidi, D. Escaff, and MG.Clerc, *Phil. Trans. R. Soc. A* **372**, 20140009 (2014). “Strong interaction between plants induces circular barren patches: fairy circles”.
7. P. Couteron , F. Anthelme, MG. Clerc, D. Escaff, C. Fernandez-Oto, and M. Tlidi, *Phil. Trans. R. Soc. A* **372**, 20140102 (2014). “Plant clonal morphologies and spatial patterns as self-organized responses to resource-limited environments”.
8. D. Escaff, C. Fernandez-Oto, M. G. Clerc and M. Tlidi, *Physical Review E* **91**, 022924 (2015). “Localized vegetation patterns, fairy circles, and localized patches in arid landscapes”.
9. A. Reina, G. Valentini, C. Fernández-Oto, M. Dorigo and V. Trianni, *PLoS ONE* **10**(10), e0140950 (2015). “A Design Pattern for Decentralised Decision Making”.
10. M. Tlidi, C. Fernandez-Oto, M. G. Clerc, D. Escaff and P. Kockaert, *Phys. Rev. A* **92**, 053838 (2015). “Localized plateau beam resulting from strong nonlocal coupling in a cavity filled by metamaterials and liquid-crystal cells”.

#### Proceedings Articles

1. G. J. de Valcárcel, C. Fernandez-Oto, M. Tlidi, K. Panajotov, and K. Staliunas. *Proc. SPIE 9134, Semiconductor Lasers and Laser Dynamics VI*, 913416 (May 2, 2014). “Phase bistable patterns in VCSELs due to spatial rocking”.
2. C. Fernandez-Oto, M.Tlidi, D. Escaff, MG. Clerc, and P. Kockaert. *Proc. SPIE 9136, Nonlinear Optics and Its Applications VIII; and Quantum Optics III*, 91360K (May 1, 2014). “Strong nonlocal interaction stabilizes cavity solitons with a varying size plateau”.